

Dipl.-Ing. Wernfried Haas

Morphology control of high-performance polymer solar cells

DOCTORAL THESIS

For obtaining the academic degree of
Doktor der technischen Wissenschaften

Doctoral Programme of Technical Sciences
Technical Physics



Graz University of Technology

Supervisor:

Ao.Univ.-Prof. Dipl. Ing. Dr.techn. Ferdinand Hofer
Institut für Elektronenmikroskopie und Feinstrukturforschung

Graz, April 2013

STATUTORY DECLARATION

I declare that I have authored this thesis independently, that I have not used other than the declared sources / resources, and that I have explicitly marked all material which has been quoted either literally or by content from the used sources.

EIDESSTÄTTLICHE ERKLÄRUNG

Ich erkläre an Eides statt, dass ich die vorliegende Arbeit selbstständig verfasst, andere als die angegebenen Quellen/Hilfsmittel nicht benutzt, und die den benutzten Quellen wörtlich und inhaltlich entnommenen Stellen als solche kenntlich gemacht habe.

Graz, 15. 4. 2013

(signature / Unterschrift)

Danksagung

Die vorliegende Arbeit entstand im Zuge einer Projektzusammenarbeit zwischen zwei Instituten, FELMI/ZFE und ICTM. Zu allererst möchte ich Prof. Ferdinand Hofer vom FELMI/ZFE herzlichst für sehr viele Dinge danken: die Möglichkeit, die Dissertation bei ihm am Institut durchzuführen, ausführliche Gespräche, zu denen er sich regelmäßig trotz eines ständig vollen Terminplans immer Zeit genommen hat und mit seinem umfassenden Wissen wichtigen und wertvollen Input für Untersuchungen, wie auch das Niederschreiben der Ergebnisse in Publikationen und dieser Arbeit, gegeben hat. Die Zusammenarbeit mit dem ICTM war stets eine wahre Kooperation ohne Abgrenzungen in „wir“ und die „anderen“. Prof. Gregor Trimmel und Dr. Thomas Rath vom ICTM möchte ich ebenfalls von ganzem Herzen für ihr Engagement im Projekt und die Unterstützung, die sie mir in vielen Gesprächen sowie der gemeinsamen Arbeit an Untersuchungen und Publikationen geleistet haben herzlichst danken. Meinem Zweitgutachter Prof. Joachim Loos möchte ich ebenfalls für die Zeit, die er sich zum Durchlesen meiner Arbeit genommen hat sowie für sein Feedback während der Verfassung dieser Arbeit meinen Dank aussprechen.

Über die erwähnten Personen hinaus habe ich im Zuge meiner Arbeit mit unzähligen Kolleginnen und Kollegen am FELMI/ZFE und ICTM/CD-Labor für Nanokomposit-Solarzellen zusammengearbeitet. Obwohl ich jeden und jede meiner Kollegen und Kolleginnen gerne namentlich nennen würde, unterlasse ich dies, da dies vermutlich den Umfang der vorliegenden Arbeit sprengen würde. Stattdessen möchte ich gerne einige der Dinge nennen, für die ich ihnen sehr dankbar bin:

Am FELMI/ZFE möchte ich mich bei allen Leuten aus den beiden TEM-Gruppen herzlich für ihre Unterstützung, besonders in der Einlernphase am Mikroskop sowie bei der oft sehr produktiven Diskussion bezüglich Optimierung der Messmethoden und Verwendung der Mikroskope, danken. Auch zu den anderen Arbeitsgruppen hatte ich regelmäßig Kontakt und möchte mich bei diesen Kolleginnen und Kollegen für ihre Unterstützung bei Messungen und Probenvorbereitung ((E)SEM, Raman, FIB, Illion, Präparation von Nanopartikelproben, Mikrotomie, u.v.m) bedanken. Mein Dank gilt aber keinesfalls nur der technischen Unterstützung, vielmehr fand ich bei meinen Kollegen und Kolleginnen am FELMI/ZFE auch immer ein freundliches Klima vor, in dem man gerne seiner Arbeit nachgeht. Dies äußerte sich über die Jahre auch regelmäßig durch über die Arbeit hinausgehende Kontakte und selbstverständlicher Weise auch über den Spaß, den wir in unserem Büro hatten.

Die Kolleginnen und Kollegen am ICTM sah ich zwar nicht ganz so regelmäßig wie jene am FELMI; wenn ich dort war habe ich den Kontakt immer genossen. Die Zusammenarbeit war auf persönlicher Ebene ausgesprochen gut und freundschaftlich, gleichzeitig - und vielleicht gerade deshalb - auch sehr produktiv. Mir wurden stets gut vorbereitete Proben übergeben, die sich gut für Messungen eigneten und deren Ergebnisse dann auch sinnvoll verwendet wurden, wie sich unter anderem auch am Output an Publikationen des CD-Labors erkennen lässt.

Meine Freunde und meine Familie haben an der Arbeit im Gegensatz zu den oben erwähnten zwar nicht direkt mitgewirkt, jedoch möchte ich ihnen besonders danken. Menschen um sich zu haben, die vorbehaltlos hinter einem stehen und ihre Unterstützung geben war für mich ein ausgesprochen wichtiger Faktor, der mir sehr bei der Durchführung meiner Arbeit geholfen hat.

Eine Person, die mich über den Zeitraum meiner Arbeit besonders intensiv begleitet und unterstützt hat, möchte ich noch namentlich erwähnen: Meine – anfangs Freundin – dann Verlobte – und jetzt Ehefrau Claudia.

Abschließend möchte ich meinen Dank an alle involvierten Personen noch einmal wiederholen. Wir hatten einige erfolgreiche und gute Jahre – auf viele weitere ebenso gute!

1 Table of contents

1	Table of contents.....	i
1.1	List of abbreviations	iii
2	Introduction.....	1
3	Materials & Methods	5
3.1	Sample preparation for nanoparticles.....	5
3.1.1	General procedure	5
3.1.2	Choice of sample grid	5
3.1.3	Choice of solvent for nanoparticles and processing parameters	5
3.1.4	Contamination caused by sample and sample grid.....	6
3.1.5	Evaluation of sample grids	6
3.1.6	Measurement of background signal and contamination	7
3.1.7	Presence of holes in films.....	8
3.1.8	Stability assessment and reproducibility.....	8
3.1.9	Summary of results	9
3.2	Synthesis of $\text{Cu}_2\text{ZnSnS}(\text{e})_4$ nanoparticles	9
3.3	Preparation of solar cells / thin film specimens	9
3.3.1	General procedure for nanocomposite solar cells.....	9
3.3.2	Preparation of thin films for TEM.....	11
3.3.3	FIB preparation of cross sections for TEM investigations	11
3.3.4	Ultramicrotomy	12
3.4	Most commonly used microscopy techniques & special aspects for nanocomposite solar cells	12
3.4.1	Electron microscopes	12
3.4.2	Special aspects	13
4	Experimental Part.....	19
4.1	Investigations on $\text{Cu}_2\text{ZnSnS}(\text{e})_4$ nanoparticles	19
4.1.1	Introduction	19
4.1.2	$\text{Cu}_2\text{ZnSnS}(\text{e})_4$ – optimizing the synthesis of stoichiometric nanoparticles	19
4.1.3	Detailed analysis of chemical inhomogeneity in CZTSe nanoparticles.....	25
4.1.4	Analyzing chemical inhomogeneity on the Titan platform	30
4.2	Characterization of nanocomposite materials and devices	35
4.2.1	Introduction	35
4.2.2	Requirements.....	37
4.2.3	State of the art for TEM investigations	37
4.2.4	Methods for specimen preparation	38
4.3	Formation of CuInS_2	42
4.3.1	CuInS_2 from synthesis.....	42
4.3.2	<i>In situ</i> method	43
4.3.3	<i>In situ</i> formation of CuInS_2 inside the ESEM.....	44
4.3.4	<i>In situ</i> transformation in TEM	49
4.4	Comparison of different precursor/polymer systems	51
4.4.1	Metal sulfides in P3EBT	51
4.4.2	CIS from metal salts in polymers.....	54
4.4.3	Xanthate based precursor systems (CIS/F8T2, CIS/PSiF-DBT).....	58
4.5	Process optimization of xanthate based systems.....	60
4.5.1	Variation of temperature profile during CIS formation (F8T2)	61
4.5.2	Comparison of heating conditions (MEH-PPV).....	62

4.5.3	Variation of temperature profile during CIS formation (MDMO-PPV).....	64
4.5.4	Variation of Cu/In-precursor ratio.....	66
4.5.5	Variation of vacuum pressure	68
4.5.6	Conclusion of optimization experiments	69
4.6	Investigations on devices.....	70
4.6.1	CIS/PSiF-DBT.....	70
4.6.2	CIS/MDMO-PPV device – defect analysis.....	75
4.6.3	CIS/PCDTBT device – defect analysis.....	79
4.6.4	Devices using PSiF-DBT and silver/aluminum electrodes.....	82
4.6.5	Conclusion of the device investigations	87
5	Summary and Outlook.....	88

1.1 List of abbreviations

BF	Bright Field
BSE	Back-scattered electron
CIS	CuInS ₂
Copper xanthate	Copper (I) <i>O</i> -2,2-dimethylpentan-3-yl dithiocarbonate
CZTS	Cu ₂ ZnSnS ₄
CZTSe	Cu ₂ ZnSnSe ₄
DF	Dark Field
EDXS	Energy Dispersive X-ray Spectroscopy
EELS	Electron Energy Loss Spectroscopy
EFTEM	Energy Filtered TEM
ESB	Energy Selective Backscattered electron
FEG	Field Emission Gun
FFT	Fast Fourier Transform
FIB	Focused Ion Beam
Formvar	Polyvinyl formal resin
GIF	Gatan Imaging Filter
HAADF	High Angle Annular Dark Field
HRSTEM	High-resolution scanning transmission electron microscopy
HRTEM	High-resolution transmission electron microscopy
HTP	Hole Transport Layer
Indium xanthate	Indium (III) <i>O</i> -2,2-dimethylpentan-3-yl dithiocarbonate
ITO	Indium tin oxide
MDMO-PPV	Poly(2-methoxy-5-(3'-7'-dimethyloctyloxy)-1,4-phenylenevinylene)
MEH-PPV	Poly[2-methoxy-5-(2'-ethylhexyloxy)-p-phenylene vinylene]
P3EBT	Poly-3-(ethylbutanoat)thiophen
P3HT	Poly(3-hexylthiophen-2,5-diyl)
PCBM	[6,6]-phenyl-C61-butyric acid methyl ester
PCTDBT	Poly[[9-(1-octylnonyl)-9H-carbazole-2,7-diyl]-2,5-thiophenediyl-2,1,3-benzothiadiazole-4,7-diyl-2,5-thiophenediyl]
PPV	Poly(p-phenylenvinylen)
PSiF-DBT	Poly[2,1,3-benzothiadiazole-4,7-diyl-2,5-thiophenediyl(9,9-dioctyl-9H-9-silafluorene-2,7-diyl)-2,5-thiophenediyl]
PV	Photovoltaics
SAED	Selected area (electron) diffraction
SDD	Silicon Drift Detector
SE	Secondary Electron
SEM	Scanning Electron Microscopy
SI	Spectrum Imaging
STEM	Scanning Transmission Electron Microscopy
TEM	Transmission Electron Microscopy
XRD	X-Ray Diffraction
Z	Atomic number Z

2 Introduction

The need for reliable, clean energy

It was the dawn of the age of mankind when the flames of a fire would light up a cave and people would gather around it for its warmth. Ever since then technological as well as sociological developments have been influenced by the availability of energy. The First Industrial Revolution, powered by steam engines and coal, and the Second Industrial Revolution, enabled by the use of electricity can be considered to be the basis of today's modern life. In the 20th century Albert Einstein's famous equation gave birth to a new source of energy powerful enough to wipe out all participating parties in the Cold War and most likely the rest of the world as well. Still, today the rising global energy consumption meets the opposition of dwindling resources of fossil fuels as well as environmental problems – CO₂ emissions need to be reduced to avoid global warming. The confidence in clean nuclear energy has been shaken by the accident in Chernobyl, which was considered a once in a lifetime accident until a tsunami, following a major earthquake, hit the Fukushima power plant in 2011. As a consequence of this accident most of Japan's nuclear power plants went offline for approximately a year and plans for increasing the amount of renewable energy were made.¹ Of the currently dominating technologies hydro-electric power plants are considered eco-friendly as they emit no direct pollution, but they have huge impact on the ecosystem of the stream and surrounding areas. Thermoelectric power plants (both fossil fuels and nuclear) are dependent on water cooling and will be affected by the effects of global warming, causing them to yield lower output in the future during dry, hot summer months.² As a consequence of this global energy situation new alternative sources of energy have been developed and installed over the last years.

Solar cell technology

Among the new technologies, photovoltaics (PV) are a clean source of energy with an unlimited supply as the energy from the sun is magnitudes higher than the world-wide power consumption. However, to be successful, the production costs are a dominant factor. Over the last years prices for solar cells have been falling and some pioneer countries (e.g. Germany) have invested a lot of effort and money in integrating the rising capacity of their newly installed PV power plants (see figure 1) and wind parks into their electrical grid.³ However, the weather dependency of solar cells and wind parks requires a more flexible smart grid to balance out the demand and routing of electricity, replacing the concept of central power plants with a more widely spread one.

While photovoltaics have just begun to become a widespread source of electricity, the technology itself is not new. The photovoltaic effect was first observed in 1839 by Becquerel, but it was not until 1954 that the first working solar cells were built. This first cell was based on silicon, which became the dominant material for solar cells over the following decades. The first notable use of solar cells was in space aboard the Vanguard I satellite in 1957. Over the years production techniques for single- and multicrystalline silicon cells were improved and caused a massive decrease in price and an increase of device performance as well. Thin film solar cells were developed as an alternative to classical silicon cells due to the lower amount of material needed for the active layer. The materials used in thin film solar cells are quite widespread: cadmium telluride, copper indium gallium selenide, copper indium sulfide, cadmium sulfide, but also amorphous silicon are used. While the material consumption is lower than in classical silicon based solar cells, their power conversion is also lower and silicon is still dominating in market shares. As a third type of system organic solar cells have been researched in the last years. Compared to the other technologies, organic solar cells promise the use of cheap production techniques (roll to roll processing, printing) as well as unique properties, such as flexible devices (wearable devices, architectural use). However, device performance is still lower than in inorganic systems, as well as the long term stability. The current world record performance is held by Li et. al at 10.6%.⁴ Replacing the fullerene derivatives (e.g. [6,6]-phenyl-C61-butyric acid methyl ester (PCBM)) used in organic solar cell by inorganic nanoparticles results in hybrid, nanocomposite

solar cells. This step allows the optimization of device parameters by changing the chemistry, size or shape of the nanoparticles. At the same time, the advantages in processing and flexibility of the devices gained by the switch to organic electronics still apply. The promising system developed in the Christian Doppler Laboratory for Nanocomposite Solar Cells was investigated in this PhD thesis by the use of advanced electron microscopy techniques.

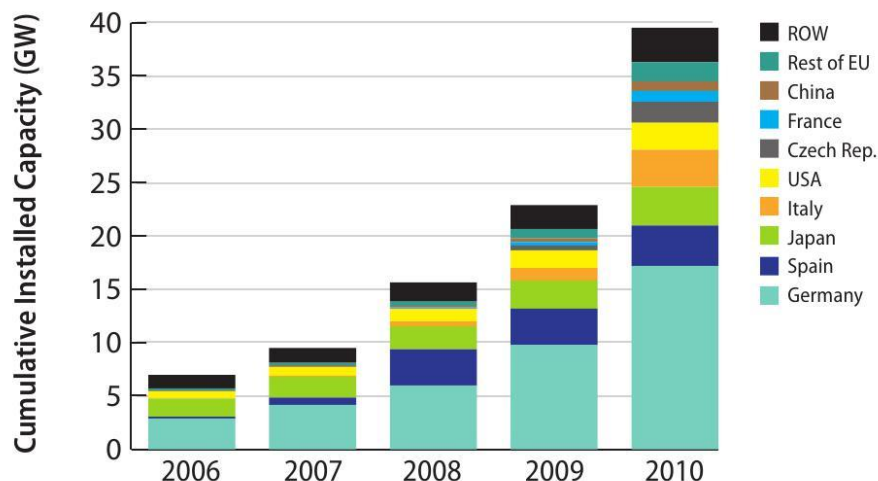


Figure 1: Cumulative installed PV capacity in the top 8 countries 2006-2010 (NREL⁵).

The nanocomposite solar cell

The type of solar cell developed in the Christian Doppler Laboratory for Nanocomposite Solar Cells and its main components are shown in the schematic in figure 2. Differently to silicon solar cells, the conversion of light into electricity is based on the formation of excitons inside the active layer of the solar cell. An exciton is generated when an incoming photon with an energy larger than the band gap of the material excites an electron from the highest occupied molecular orbital (HOMO) to the lowest unoccupied molecular orbital (LUMO). One of the advantages of hybrid solar cells is that both the inorganic as well as the organic material can absorb light and the absorption properties of the solar cell can be tuned via the band gap of both the inorganic and the organic material.

The exciton consists of an electron and a positive charge, which is a hole in case of the conjugated polymer used in these solar cells. For successful generation of electricity, the electron and the hole need to be separated and transported to the respective electrodes. The separation can only occur at the interface between donor (polymer) and acceptor (inorganic) phase. However, the exciton state is only stable for a limited time, allowing the exciton to travel 10-15 nm.^{6,7} Hence devices using a single interface between donor and acceptor yield only poor conversion efficiencies. Bulk-heterojunction devices overcome this limitation by intermixing the donor and acceptor phase since the middle of the 1990s;⁸ the excitons can be successfully separated. For this process the energy levels of HOMO and LUMO of donor and acceptor phase are important. First, an offset of at least 0.3 eV is necessary for the separation of the charges.⁹ Furthermore the effective open circuit voltage is determined by the energy difference between HOMO of the acceptor and the LUMO of the donor phase.

After successful separation at the interface, the charges need to be transported to the electrodes. The electron is transported through the acceptor to the aluminum cathode; the hole is transported through the donor to the Indium Tin Oxide (ITO) anode. Especially in bulk-heterojunction devices the presence of uninterrupted percolation pathways is essential for the transport to the electrodes. The impact of the morphology of the nanocomposite layer on device performance is discussed in chapter 4.2.1.

As shown in Figure 2, a layer of PEDOT:PSS is present below the active layer. It acts as a hole transport layer. Both the ITO anode and the substrate layer are transparent, as the incident light needs to pass through them to the active layer. While efforts are made to replace ITO,¹⁰ it is currently the most used material for transparent electrodes. The substrate for experimental laboratory devices is usually glass; however it can be replaced by polymers (e.g. PET) for building flexible devices. On top of the nanocomposite layer, the aluminum cathode is shown.

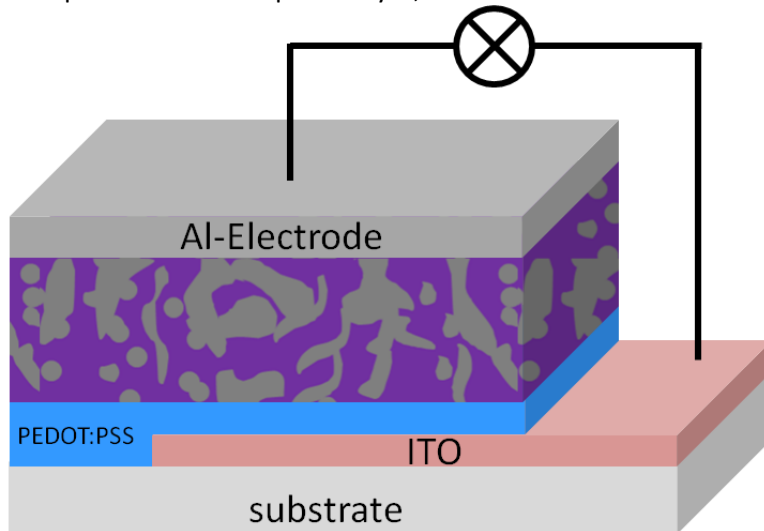


Figure 2: Schematic diagram of a nanocomposite solar cell (Dr. Thomas Rath).

Characterization of solar cells

Transmission Electron Microscopy (TEM) was developed in the 1930s and it soon allowed imaging of smaller structures as well as looking at the crystal structure using diffraction methods. In the 1990s Analytical Electron Microscopy (AEM) was developed. Two complementary methods, Energy Dispersive X-Ray Spectroscopy (EDXS) and Electron Energy Loss Spectroscopy / Energy Filtered TEM (EELS/EFTEM), allow investigating the chemical composition of a specimen. In EFTEM a series of images is recorded at certain energy windows allowing the calculation of elemental maps or jump ratio images.¹¹ On the other hand in EELS a spectrum featuring the low loss features or ionization edges for one or more elements can be recorded. The spectra can be used for quantification¹² and the fine structure also holds information on the type of chemical bond.¹³ EDXS has a much worse energy resolution than EELS, but unlike EELS/EFTEM it allows the overview measurement of all elements at the same time. When both EELS and EDXS is combined with Scanning Transmission Electron Microscopy (STEM) in Spectrum Imaging (SI), a three dimensional data cube containing an EELS and/or EDX spectrum for each pixel in the two dimensional image is recorded.¹⁴ The same can also be done in EFTEM by variation of the energy window.¹⁵ SI methods allow the extraction of data from the three-dimensional data cube such as elemental maps for all elements in a STEM-EDX SI.

Resolution in TEM and STEM is coupled to the wave length of the electron beam. Increasing resolution by increasing the acceleration voltage seems like an obvious idea, but turned out to be a dead end. While resolution was increased this way,¹⁶ even the most robust specimens hit by an electron beam at 1-2 MeV are usually damaged almost instantly.¹⁷ On the other hand more and more electron beam sensitive materials (e.g. polymers) were investigated by TEM, demanding lower beam currents and acceleration voltages. Based on the works of Rose¹⁸ a new approach for increasing resolution was developed: Lens correction. Correctors for spherical and chromatic aberration have been implemented in TEMs from all major manufacturers around the world in the last 5 years. The limits of resolution have improved significantly for both TEM and STEM.

At the same time, the analytical methods were improved. Silicon Drift Detectors (SDD) with larger areas can be mounted directly inside the microscope and have improved the efficiency of EDXS

analysis.¹⁹ The Gatan Imaging Filter (GIF) Quantum allows recording of Dual EELS spectra (one for the zero/low loss and one for the core loss at the same time) and offers improved performance in EFTEM and EELS.²⁰

Finally, the development and wide availability of Focused Ion Beam (FIB) systems allows the preparation of cross-sections for almost any type of material and device.²¹ Contrary to ultramicrotomy, where hard materials were impossible to cut, FIB can cut out specimens from almost everything – enabling the investigation of devices instead of preparing a specialized TEM specimen.

All of these recent developments are crucial for this work. A nanocomposite solar cell has a thickness in the range of around 200 nm and the nanoparticles embedded in the matrix are even smaller, most of them below 10 nm. Optical methods clearly cannot resolve these fine structures any more, the solar cell becomes a black box converting light to electricity - sometimes. Using TEM (in combination with FIB and Scanning Electron Microscopy (SEM)) enables us to see all that is happening in the range of nanometers. Devices can be investigated and explained by morphological and analytical studies, their result can explain system- and device-performance and used to build better solar cells. This work will contribute to the ongoing development of a new, clean energy source.

3 Materials & Methods

3.1 Sample preparation for nanoparticles

3.1.1 General procedure

One of the most important requirements in TEM is having a thin, electron transparent specimen. While most samples need to be cut, polished, thinned or ion-milled to achieve an adequately thin specimen, nanoparticles are already in the range of a few tenths of nanometers. However, to analyze them in a TEM, they need to be mounted on a TEM specimen grid. These grids consist of a mechanically stable metal grid on which a thin film – usually polymers or carbon – is mounted. With thinner specimens and higher magnifications the background signal added by this carbon film becomes more dominant in the measurements. Hence the properties of this film are of high importance for successful High-Resolution TEM (HRTEM) and High-Resolution STEM (HRSTEM) investigations, especially on the FEI Titan.

Usually sample preparation is simply done by solving or dispersing the nanoparticles in a volatile solvent and dripping a drop of the solution onto the sample grid. Once the solvent evaporates the nanoparticles remain on the thin film and can be investigated in the TEM. While the method itself is very straightforward, during this work some key factors for ideal sample preparation were identified.

3.1.2 Choice of sample grid

TEM sample grids are available with different films on different metal grids such as nickel or copper. Materials can be chosen to avoid interference in EDXS from stray radiation of the grid, which makes more sense than assuming the signal to be homogeneous and subtracting as shown here.²² As the samples contain copper, nickel grids were chosen in this work.

3.1.3 Choice of solvent for nanoparticles and processing parameters

Ideally the solvent is volatile, able to solve the nanoparticles and does not dissolve the carbon based film of the sample grid. As the nanoparticles could only be solved in very few solvents, the solvent had to be chosen accordingly. CHCl_3 or CH_2Cl_2 have shown to be good solvents for this purpose. However, they also dissolve the films when exposure is longer than a few seconds, which happens when specimens are prepared at room temperature. To minimize processing times samples are best prepared at 80°C inside a drying oven. This leads to evaporation of the solvent within seconds, leaving the support film mostly unharmed. Additionally, putting the specimen grid on a piece of filter paper helps minimize contact times, as the solvent is sucked from the specimen grid. As a consequence of the quick evaporation and removal of the solvent, nanoparticles are usually spread quite randomly across the film (see figure 3a).

Toluene is also an excellent solvent for nanoparticles and has a significantly higher boiling point. While its evaporation takes longer, it has a much lower tendency to dissolve the carbon based films, especially Quantifoil. This allows evaporating the toluene from specimens even at room temperature in a few minutes instead of seconds without severe damage to the carbon film. Due to the lower evaporation rate the nanoparticles are distributed more evenly on the film (see figure 3b).

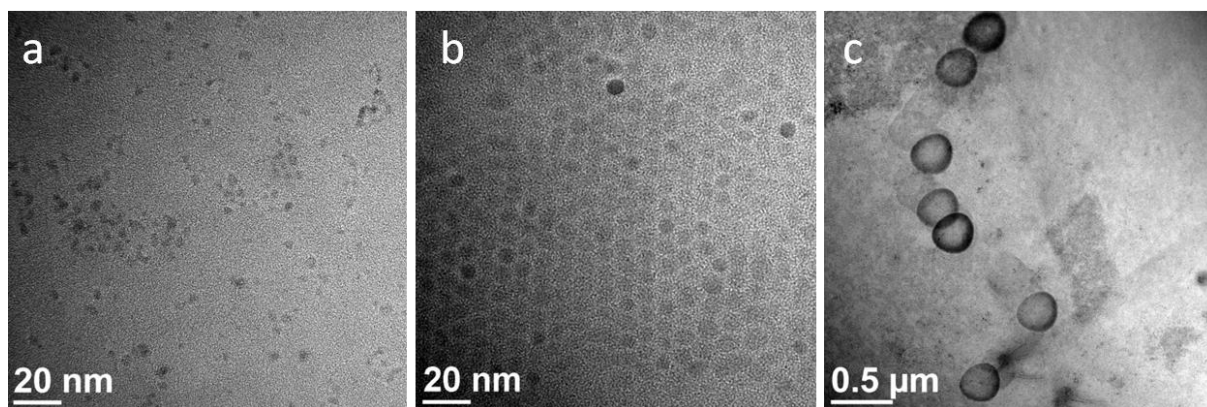


Figure 3: TEM-BF images of CZTSe nanoparticles processed from CHCl_3 at 80°C (a) and toluene at room temperature (b). While the nanoparticles in (a) are distributed randomly, they are arranged in a regular pattern in (b). The low-magnification image (c) shows contamination caused by organic material present in the specimen.

3.1.4 Contamination caused by sample and sample grid

Specimen contamination, mostly by carbon, is most crucial in TEM. Image resolution can be significantly reduced and the effect on EEL spectroscopy is even worse.

There are multiple possible sources of contamination in TEM, such as contamination of the microscope by previously measured specimens, contamination caused by the sample itself, and dirt on the sample holder. Cracking of organic molecules into volatile components and following redeposition caused by the electron beam is considered one of the main processes in this case of nanoparticle specimens.

Carbon based specimen grids can contribute significantly to the contamination of the specimen as well – this has been investigated and is presented in the contamination tests of pristine grids below.

Additionally carbon from the sample contributes to the contamination. Inorganic nanoparticles such as CuInS_2 (CIS) or $\text{Cu}_2\text{ZnSnS}_4$ (CZTS) / $\text{Cu}_2\text{ZnSnSe}_4$ (CZTSe) usually contain an organic capping agent (copper). The copper cannot be removed, as it is necessary to prevent agglomeration of the nanoparticles. However, usually a lot of excess copper and other organic material from synthesis are present in the solution. These organic materials can easily be removed by placing the specimen grid on filter paper during specimen preparation as described above. While most of the nanoparticles attach themselves to the support film, the organic material stays in solution and is removed from the specimen grid into the filter paper. Specimens prepared this way showed a significantly lower tendency to contaminate than samples prepared without filter paper, in which case the organic material stays on the specimen after evaporation of the solvent. As a downside for the reasons mentioned above, this has a negative impact on the arrangement of the nanoparticles.

Figure 3c shows a low-magnification image of the specimen prepared from toluene at room temperature without filter paper as presented in figure 3b. While the nanoparticles are arranged in a regular pattern, the contamination from placing the electron beam in TEM Bright Field (BF) mode on the sample for a few minutes can clearly be seen.

As a consequence the slow evaporation process was used when regularly arranged nanoparticles were desired for BF imaging. The rapid evaporation process was chosen for most specimens to keep contamination effects as low as possible for analytical investigations.

3.1.5 Evaluation of sample grids

Homemade Formvar (Polyvinyl formal resin) support film as well as commercially available sample support films on nickel grids (Quantifoil, Luxfilm, carbon films type S147N2 and S166N2; all bought from Gröpl Elektronenmikroskopie) were evaluated for their use in sample preparation.

Procedure for homemade Formvar films:

0.25 g Formvar (bought from Merck, used without further purification) was stirred in 100 g CHCl_3 for 2 hours. 2 ml glycerine were added to 32 ml of previously prepared solution and stirred for 12 hours. The emulsion was shaken before application to gain a well dispersed emulsion. Microscope slides were dipped into the emulsion and dried for 10 minutes. Both sides of the microscope slides were exposed to H_2O vapor for one minute and dried for another 10 minutes. The film was cut on the sides of the microscope slides and floated off in deionized water. Subsequently the film was transferred onto 200 mesh nickel TEM grids and dried over night. The TEM grids were exposed to saturated acetone atmosphere for 30-60 seconds and the size of the resulting holes in the film was controlled in a TEM. Afterwards they were coated with 5 nm carbon for increased stability.

S147N2 and S166N2 are commercially available carbon films with a thickness of 15-25 nm. The main difference is the ratio between film and holes; S166N2 is a lacey carbon film whereas S147N2 is a film with significantly smaller holes.

Luxfilm is a 30 nm thick Nylon film with high mechanical stability, but lacks holes. Since early 2012 it is no longer commercially available.

Quantifoil 3.5/1 is a combination of carbon and Formvar with a thickness of 20 nm. Quantifoil features a highly regular structure of holes and is available featuring different hole patterns. Type 3.5/1 was chosen because of its high amount of film with relatively small holes.

TEM grids with home-made carbon nanosheets were kindly provided by Nottbohm et al.²³ Initial tests showed a very thin film, which is perfect for high resolution work. However, high beam currents, especially in STEM, caused the immediate destruction of the film. As high beam currents are often required for analytical work, especially in EDXS, these films were not included in further investigations.

For the evaluation of different specimen grids various parameters – some of them “soft” parameters mostly connected to handling issues, some of the “hard” and quantifiable – were established and measured.

- Background signal: The amount of background signal added by interaction of the support film with the electron beam correlates to the thickness of the film and can be measured (see table 1 and figure 4).
- Contamination: Different types of support films show a varying tendency to contaminate even in pristine state (see table 1 and figure 4).
- Holes: The presence of holes in the film allows observation of free standing nanoparticles located at the border of holes without background from the support film.
- Mechanical & chemical stability: Rating of the stability against mechanical damage and solving the film during sample preparation.
- Reproducibility: Rating on how reproducible different batches of support films are with respect to the other key parameters in the evaluation.

3.1.6 Measurement of background signal and contamination

Background signal and contamination were both measured in STEM-HAADF (STEM with High Angle Annular Dark Field) mode under identical conditions (FEI Tecnai 20, C2 70 μm , emission 3, spot size 5, camera length 100 mm) by scanning a defined area (indicated magnification 450 kx, scanned area 130 x 130 nm^2) for 2.5 and 5.0 minutes. The relative signal increase of the film and the two contaminated areas with respect to the signal in vacuum are shown in table 1 and figure 4. Quantifoil clearly shows to add the least amount of background signal and also gains the smallest signal increase due to contamination. The background signal and contamination behavior of S147N2 and

S166N2 is significantly higher than Quantifoil, but they are still acceptable alternatives to Quantifoil. Luxfilm and the homemade films add a large quantity of signal already in uncontaminated state and contaminate strongly.

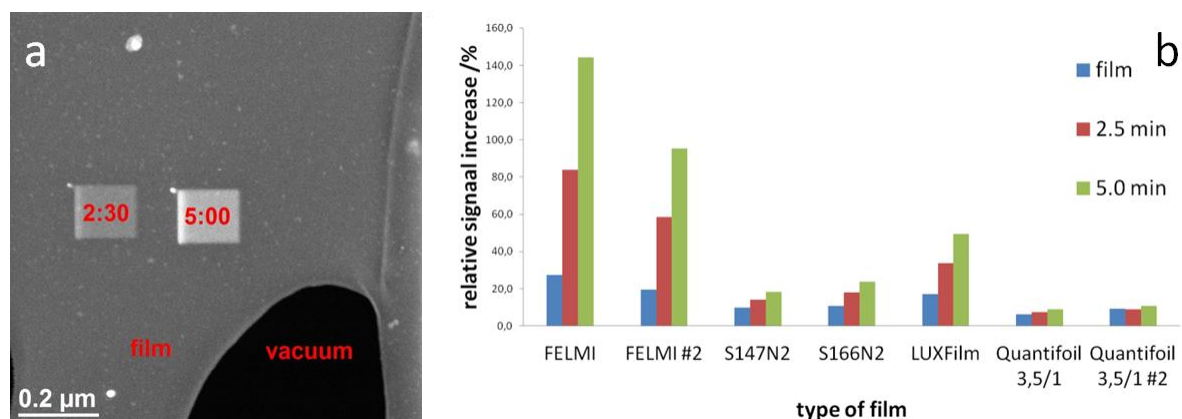


Figure 4: (a): STEM-HAADF image showing a type S147N2 TEM-grid; contaminated regions (2:30, 5:00), uncontaminated film (film) and empty regions (vacuum); (b) Graphical representation of the data shown in table 1.

Table 1: Relative signal increase (%) of investigated carbon films compared to vacuum. The signal increase for the plain film, areas exposed to the beam for 2.5 min and 5.0 min is shown.

Support film type	film	2.5 min	5.0 min
FELMI	27.3	83.8	144.4
FELMI test #2	19.7	58.4	95.4
S147N2	10.0	14.1	18.3
S166N2	10.8	18.1	23.8
Luxfilm (Nylon), 30 nm	17.1	33.7	49.6
Quantifoil 3,5/1, 20 nm	6.4	7.4	8.9
Quantifoil test #2, 20 nm	9.3	8.8	10.9

3.1.7 Presence of holes in films

Luxfilm is the only film without holes. Quantifoil has a very regular, repeating structure with holes at defined positions. All other films show a more irregular structure, but holes are present.

3.1.8 Stability assessment and reproducibility

Mechanical stability: The absence of holes in Luxfilm gains high mechanical stability, which is significantly better than all other films – which is however not really that necessary for the preparation of nanoparticles.

Chemical stability: None of the films is able to withstand CHCl_3 for longer than a few seconds. When the conditions described above (evaporation at 80°C and presence of filter paper) were used the solvent was evaporated quickly and drawn into the filter paper. In this case the contact time and hence the damage to the films due to the solvent could be minimized and no significant differences could be observed between the films.

The chemical stability against solvents is generally not perfect in all of the films, but following the technique described above (80°C and filter paper) specimens can be prepared with only little to no damage to the film.

Reproducibility: Luxfilm and Quantifoil are highly reproducible due to their defined structure; the homemade films are rather irreproducible, especially with respect to their background signal and contamination behavior.

3.1.9 Summary of results

Table 2 shows a summary of the different parameters for each of the investigated films. Considering background signal and contamination behavior the primary key issues for the support film and a rather equal rating of all films in the “soft” parameters, Quantifoil was chosen as support film and was used preferably throughout this work. Processing solutions in CHCl_3 or toluene at 80°C inside an oven by putting the sample grid on filter paper was identified as the method of choice for minimizing contamination from the nanoparticle solution.

Table 2: Evaluation of key parameters for various support films

	background signal	contamination	holes	mechanical stability	chemical stability	reproducibility
Homemade	-	--	+	o	o	-
S147N2	+	+	+	o	o	o
S166N2	+	+	+	o	o	o
Luxfilm	o	o	-	++	o	+
Quantifoil	++	++	++	o	o	+

3.2 Synthesis of $\text{Cu}_2\text{ZnSnS(e)}_4$ nanoparticles

$\text{Cu}_2\text{ZnSnS(e)}_4$ nanoparticles were synthesized by a modified version of the synthesis route described by Hyeon et al.^{24,25} In a typical synthesis, metal salts (copper-I-acetate, zinc-II-iodide, and tin-IV-acetate) are dissolved in oleylamine and heated 30 minutes at 170°C until the solution is clear. The solution is cooled down and S or Se in oleylamine is added. The solution is heated to $210\text{-}230^\circ\text{C}$ for approximately 90 minutes. Further experimental details are described elsewhere.²⁶ Nanoparticle synthesis was carried out at the ICTM (TU Graz) by Dr. Thomas Rath and DI Angelika Pateter.

3.3 Preparation of solar cells / thin film specimens

3.3.1 General procedure for nanocomposite solar cells

Solar cells using a variety of polymers and CuInS_2 nanoparticles formed from different precursor materials were investigated throughout this work. They were built following a generic procedure: Glass/ITO slides were cleaned in deionized water and isopropanol in an ultrasonic bath. Optionally a layer of PEDOT:PSS was coated as hole transport layer. The nanocomposite layer was coated from a solution of polymer and precursor material using spin coating or doctor blading. During a heating step the nanoparticles were formed from the precursor material inside the polymer layer. The metal cathode was deposited using a shadow mask and thermal evaporation of the metal.

HTP	polymer	precursor	coating	processing	cathode
none	P3EBT	Cu(Ac), InCl ₃ , Zn(Ac) ₂ , TU	spin coating	tube furnace (~200°C, ~20mins, vacuum)	Al
	MEH-PPV	Cd(Ac) ₂ ·nH ₂ O, TU			
	F8T2	Zn(Ac) ₂ , TU			
PEDOT: PSS	PSiF-DBT	Pb(SCN) ₂ , TU	doctor blading	heating plate (N ₂ atmosphere)	Al/Ag
	PCDTBT	CuI, InCl ₃ , TAA			
	MDMO-PPV	Cu/In xanthate			

Figure 5: Process flow for the production of nanocomposite solar cells. For each key element all possibilities used in this work are listed. The most commonly used options throughout this work are highlighted.

An overview of the key elements in the process flow is shown in figure 5; the most commonly used options are highlighted. While it seems obvious that the combinations of inorganic materials (mostly CIS, but also CdS/ZnS/PbS) and polymers were chosen because of matching band gaps that promise high performance solar cells, the choice of materials was also influenced by external factors. Over the time of the project development of the solar cells was conducted in two geographic locations at the TU Graz and NTC Weiz. At the beginning of the project one of the objectives was the development an efficient hybrid solar cell based on CIS. Soon the choice was made to use an in situ route to avoid copper based synthesis of the nanoparticles. During development challenges were solved step by step, and thus having influence on the choice of polymers.

The initial concept for the in situ route used metal salts and thiourea. A solvent for the precursor materials as well as a soluble polymer had to be found. The combination of P3ETB and pyridine as solvent were found to be processible and were applied to CdS/ZnS/PbS-P3EBT and metal salts/thiourea-P3EBT. Additionally a mixture of water/ethanol was used to solve precursor metal salts, thioacetamide and a precursor for the polymer PPV.

The introduction of the xanthate precursor system improved the solubility of the precursors, especially since changing the chemistry of the side chain of the xanthate can be used to tune its solubility. Solvents that could not be used before in combination with metal salts, such as chlorobenzene, could now be used. This development opened the window for so far insoluble polymers. A number of polymers was investigated experimentally in the CD Laboratory and hence also investigated in the TEM. P3HT is one of the best researched polymers for organic solar cells using P3HT and PCBM. Even though the energy levels of its HOMO and LUMO should match very well with CIS, all initial experiments failed. As a consequence other polymers were tested; among the successful polymers were MDMO-/MEH-PPV and F8T2. All of these polymers are readily available and their HOMO/LUMO levels are also a good match for CIS. The low band gap polymers PSiF-DBT and PCDTBT are an ideal choice with respect to their band gap, but also with respect to other processing parameters, such as the solubility in chlorobenzene and their film forming properties. However, both of them were not available in the earlier half of the project. As soon they became commercially available they were bought and characterized in solar cells.

Detailed information about the production of individual systems can be found in literature for CdS/ZnS/PbS-P3EBT,²⁷ Metal salts/thiourea-P3EBT,²⁸ Metal salts/thioacetamide,²⁹ xanthate/PsiF-DBT.³⁰ Experimental details about xanthate based solar cells using F8T2, MEH-PPV, PSiF-DBT, PCDTBT and MDMO-PPV are described elsewhere.³¹ The structures of polymers used in this work are shown in figure 6.

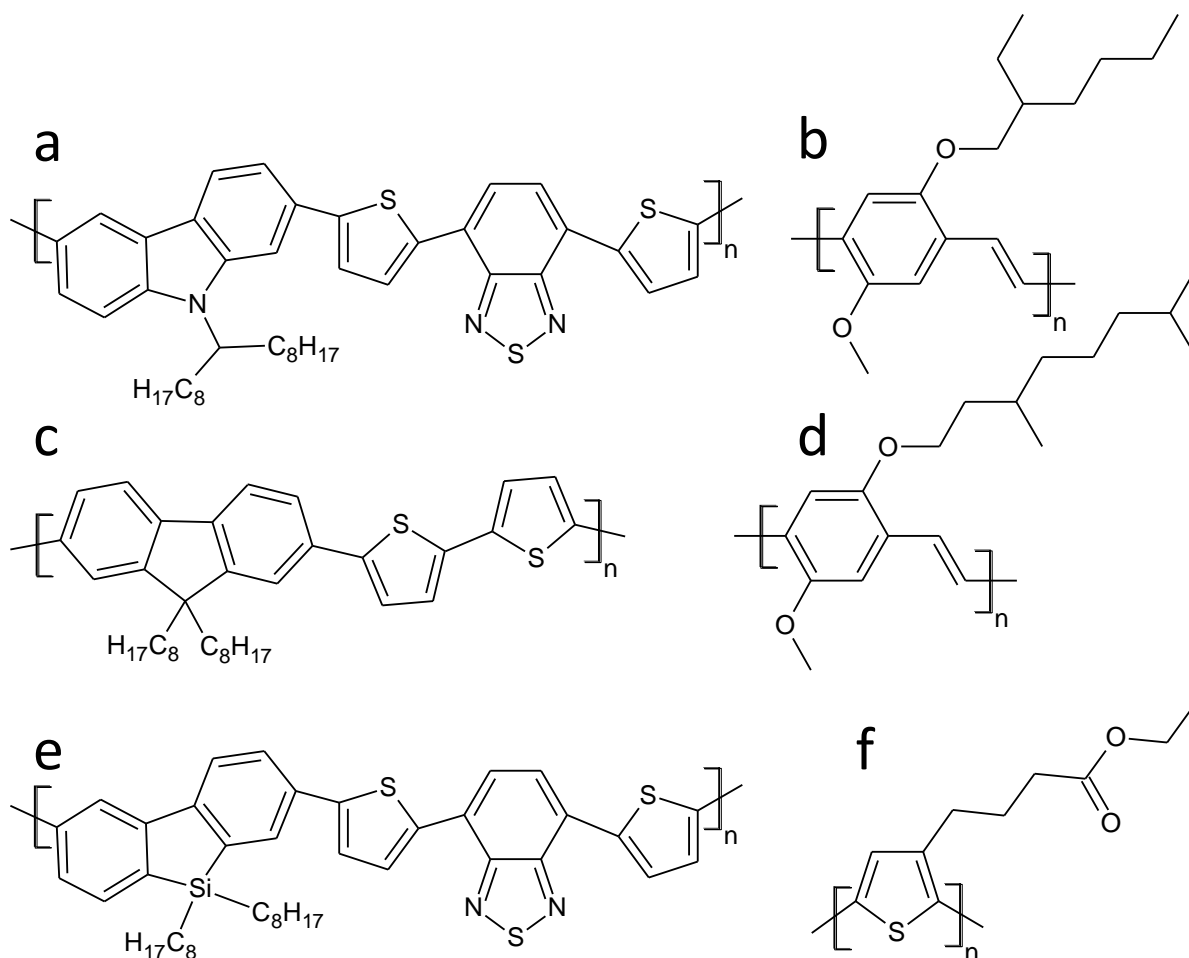


Figure 6: Polymers used for the preparation of nanocomposite solar cells: PCDTBT (a), MEH-PPV (b), F8T2 (c), MDMO-PPV (d), PSiF-DBT (e), P3EBT (f)

3.3.2 Preparation of thin films for TEM

TEM specimens were prepared by spin coating a solution of polymer and precursor on NaCl single crystals (acquired from Korth Kristalle GmbH, Item #1040001, 13 mm \varnothing x 2 mm) at 800 to 2000 rpm. All other parameters of the process (polymer/precursor concentration, oven temperature, etc) were unchanged with respect to the corresponding solar cells to gain a specimen with the same properties as the solar cells.³²

3.3.3 FIB preparation of cross sections for TEM investigations

FIB lamellae were prepared on a FEI Nova 200 Dual Beam FIB using the in situ lift out procedure.²¹ Electron beam induced platinum deposition was done at 5 kV and 1.6 nA; Ion beam induced platinum deposition was done at 30 kV and 100 pA. Ion milling was performed at 30 kV acceleration voltage with decreasing beam currents from 1 nA down to 500 pA. The lamellae were transferred to Mo TEM grids using the in situ Omniprobe™ system. Thinning to electron transparency was done at 100 to 50 pA. A final cleaning step to reduce preparation induced amorphous surface layers was done at 5 kV and 70 pA with a milling angle of 5 degrees. FIB lamellae were prepared by Dr. Meltem Sezen, Dr. Thomas Haber and Martina Dienstleder.

3.3.4 Ultramicrotomy

Solar cells coated on PET-ITO instead of glass-ITO were embedded in Spezifix 40 and sectioned using an ultramicrotome (Leica UCT) at room temperature with a thickness of 100-120 nm per cut. The cuts were transferred to 200 mesh TEM grids.

3.4 Most commonly used microscopy techniques & special aspects for nanocomposite solar cells

A wide range of electron microscopy related techniques was used throughout the work presented here. While the techniques are very well known and documented in literature and textbooks, special aspects for the investigation of nanocomposite solar cells and nanoparticles have to be considered.

3.4.1 Electron microscopes

3.4.1.1 Transmission Electron Microscopy (TEM)

The Philips CM20 is operated at 200 kV with a LaB₆ cathode and equipped with a Noran HPGe detector, a DigiScan II STEM controller and a Gatan 678 Imaging Filter. This microscope was primarily used for STEM/EDXS work.

The FEI Tecnai 20 (T 20) is operated at 200 kV with a LaB₆ cathode and equipped with a Fischione HAADF detector, a DigiScan II STEM controller and an EDAX Sapphire Si(Li) detector.

The FEI Tecnai F 20 (TF 20) microscope is operated at 200 kV with a Schottky emitter type Field Emission Gun (FEG) and equipped with a Gatan GIF Tridiem energy filter, an UltraScanCCD camera, a Fischione HAADF detector, an EDAX Sapphire Si(Li) detector and a DigiScan II STEM controller. This microscope was used for HRTEM, EFTEM, SI, STEM, EELS and EDXS work. Point resolution in TEM mode is 0.24 nm, HR-STEM resolution is 0.2 nm.

The FEI Titan³ is operated at 300 kV with a X-FEG and equipped with a Gatan GIF Quantum energy filter system, a DigiScan II STEM controller and a FEI ChemiSTEM system for EDXS. Point resolution in TEM mode is 0.24 nm, HR-STEM resolution is 0.08 nm. A schematic diagram and the illumination modes are shown in figure 7.

3.4.1.2 Scanning Electron Microscopy (SEM)

The Zeiss Ultra 55 is operated at 0.1-30 kV with a FEG, InLens and Energy Selective Backscattered electron (ESB) detector. It was mainly used for SEM imaging work.

The FEI Quanta 600 is operated at 2-30 kV with a FEG, Back-Scattered Electron (BSE) and Secondary Electron (SE) detector. The low vacuum mode allows investigating specimens without additional conductive coating. A homemade heating stage was used for heating experiments.³³

A FEI Nova 200 Dual Beam FIB equipped with SE/BSE detector, a Ga ion source, Pt gas injection system and Omniprobe was used for preparation of the FIB lamellae. The experimental details for the preparation of FIB lamellae are described in chapter 3.3.3.

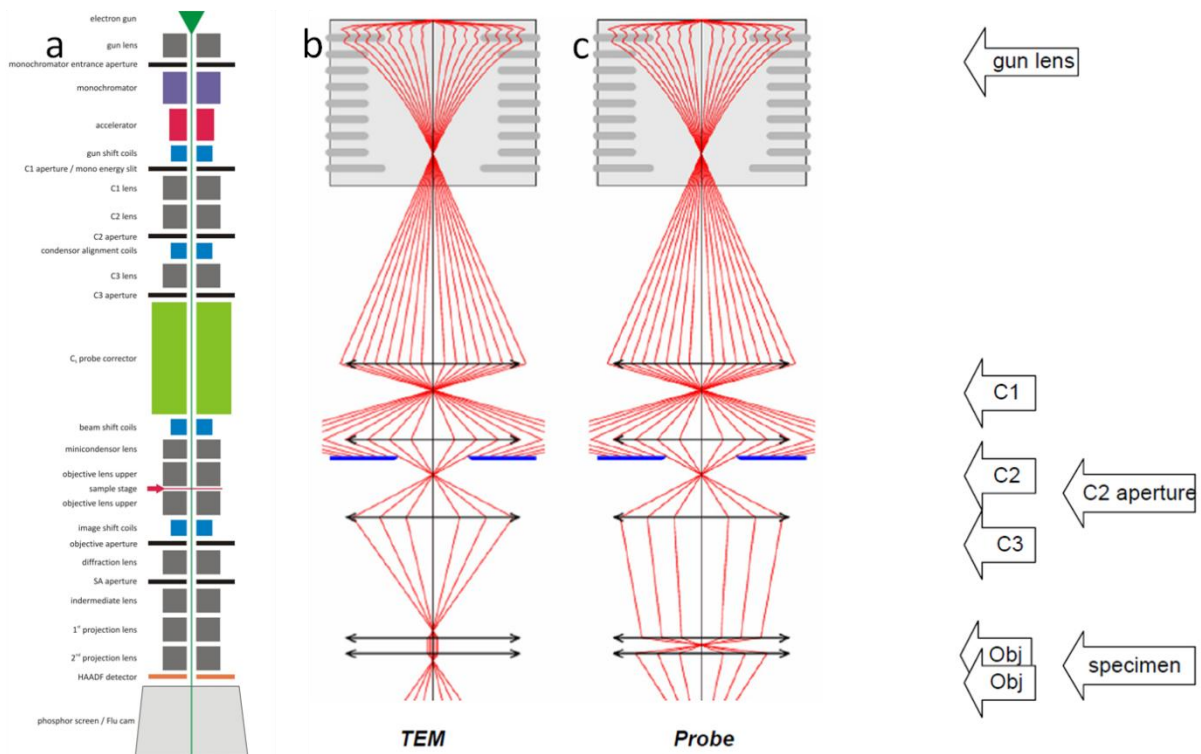


Figure 7: Schematic diagram of the FEI Titan (a, Dr. Evelin Fisslthaler), Illumination in nanoprobe mode for TEM (b) and STEM (c, FEI Titan condenser manual).

3.4.2 Special aspects

3.4.2.1 Imaging techniques:

Being the standard mode of operation conventional bright field TEM plays an important role in the presented work. Under parallel illumination conditions the objective aperture is placed in the back focal plane of the objective lens, blocking electrons that are scattered off the optical axis. The interaction of the electron beam leads to a decrease of intensity in areas that are thick or contain heavy atoms. This mechanism is known as mass-thickness contrast. In an evenly thick specimen, areas containing heavy atoms appear darker than areas containing light atoms. In practice this causes areas containing CIS nanoparticles to appear dark, while areas containing the polymer appear brighter. However, areas containing the same material also appear darker if they are thicker. Even though both thin films and FIB lamellae usually do not show large variations in thickness, this effect can be noticed in the specimens shown in chapter 4.4.3, where the formation of string like structures (which also include a high amount of CIS nanoparticles) were formed. In addition to mass-thickness contrast crystalline areas that fulfill Bragg scattering conditions due to their orientation also appear dark. To avoid misinterpretation of these dark areas the specimen can be tilted. As soon as the angle is changed the Bragg contrast disappears and only mass-thickness contrast remains. An example is shown in chapter 4.4.2. Dark field TEM makes use of Bragg scattering by placing the objective aperture off-axis on a diffraction spot allowing only crystals that reflect into this spot to be visualized in the image. As shown in chapter 4.4.2 this method can be used to determine the size of nanocrystals inside of large agglomerates. Both TEM-BF and TEM-DF offer a quick way to investigate the size and shape of nanoparticles prepared on support films as well as investigations on the morphology of nanocomposite solar cells and the nanoparticles within.

Using sufficiently thin, crystalline specimens at higher magnifications phase contrast becomes the dominant mechanism for contrast generation. When passing through the specimen the beam can be

considered as a wave interacting with the atomic columns of the specimen, causing a phase shift in the exiting beam. The exit wave can be described using the Contrast Transfer Function (CTF). In a phase contrast image areas containing atomic columns appear at different brightness than the space between them. However, phase shift and intensities are a function of the sample thickness; hence HRTEM is usually coupled to simulations. They allow a deeper understanding of the actual location of the atomic columns in the image. These simulations require knowledge of the sample thickness. As this is usually not known for the non-spherical nanoparticles and varies for each individual nanoparticle, this part of the analysis was not performed. Even without knowledge about the exact location of the atomic columns information about the crystal structure can be gained. The lattice distance can be measured and defects in the crystal are visible. Normally high resolution TEM usually requires careful orientation along the zone axis of a crystal. The specimens investigated in this work are nanoparticles in random orientation (though there are some preferred ones for nanoparticles immobilized on the surface of a TEM grid); the orientation process can usually be skipped by simply searching for already oriented nanoparticles.

3.4.2.2 Scanning Transmission Electron Microscopy (STEM):

While the whole specimen area is illuminated in conventional TEM using a parallel beam, a convergent beam (probe) is used to illuminate a small area of the specimen in STEM mode. While scanning over the specimen a signal is recorded for each spot (corresponding to a pixel in the image) using one or multiple detectors (DF, HAADF, but also spectroscopy with EDXS or EELS). Due to the imperfection of electron lenses inside the microscope resolution in STEM is limited by the size of the probe. The probe size is affected by the imperfections of the condenser system, mainly spherical aberration, but also coma, astigmatism and higher order aberrations. Correction of these lens aberrations using a Cs corrector allows significant improvements, enabling atomic resolution STEM. Differently to HRTEM, images are easy to interpret and actually show the location of the atoms without the need for simulations.

The microscope is operated in diffraction mode in STEM, due to the convergent beam a CBED pattern is formed when interacting with crystalline materials. Additionally electrons are scattered by elastic and inelastic scattering. A bright field detector can be used to pick up the signal in the middle. Its signal intensity is weakened by the specimen similar to conventional TEM-BF imaging. The ring shaped dark field (DF) and high angle annular dark field (HAADF) detectors are placed concentrically around the BF detector and have a hole in the middle. They allow picking up signals between certain angles. These angles can be adjusted by changing the camera length.

In STEM-HAADF contrast is primarily based on elastic interaction between the positively charged nucleus and electrons from the electron beam (Rutherford scattering). Heavy atoms cause scattering to high angles. These electrons are picked up by the HAADF detector. A higher brightness in these images corresponds to a higher atomic number Z .³⁴ As the active layer of nanocomposite solar cells consist of a carbon based matrix (low Z) and inorganic nanoparticles (CuInS_2 , higher Z), this method allows investigating the inorganic phase with only little contrast from the polymer. This also applies for $\text{Cu}_2\text{ZnSnS}(e)_4$ nanoparticles on carbon support films.

$\text{Cu}_2\text{ZnSnS}(e)_4$ nanoparticles often show defects in their crystal structure (mostly twinning), which can be seen by tilting the sample in conventional BF or DF mode. STEM-DF however offers a much more efficient way to image these defects without the need to tilt the sample. A comparison between DF and HAADF images is shown in “ $\text{Cu}_2\text{ZnSnS}(e)_4$ – optimizing the synthesis of stoichiometric nanoparticles”, figure 15.

3.4.2.3 Selected Area Electron Diffraction (SAED)

As mentioned before, the electron beam can be scattered by crystalline specimens if Bragg conditions are fulfilled. This often adds unwanted contrast in BF mode, but these diffraction patterns can be recorded in diffraction mode. Investigation of diffraction patterns can be used to gain information about the crystal structure of single- or polycrystalline materials. Using selected area

apertures of different size a region of the specimen can be selected for investigation, so that only its diffraction pattern is shown in the diffraction image. However, in a nanocomposite even the smallest selected area apertures do not allow selecting individual nanoparticles for diffraction analysis, but rather a few tens or hundreds. As a consequence SAED measurements usually show typical ring patterns, which yield similar information as powder X-ray diffraction. The most prominent peaks can be extracted and compared with reference data from the Joint Committee on Powder Diffraction Standards (JCPDS) database.

Data evaluation was done by using David Mitchell's CHT³⁵ plugin³⁶ for Digital Micrograph. It can be used for the automatic analysis of circular diffraction patterns in a reproducible way and produces a radial intensity profile including d-values for the main peaks as output. The procedure described in literature³⁷ was followed, only the threshold value was changed to 75.

3.4.2.4 Energy-Dispersive X-ray Spectroscopy (EDXS)

During inelastic scattering an electron from the incident beam interacts with an electron from an atom in the specimen. Energy is transferred from the incident electron (this energy loss can be measured in EELS), and the electron from the atom is ejected from its shell. The hole in the shell is filled with an electron from a higher energy level, and a characteristic amount of energy is released as an X-ray photon. However, instead of emission of a photon also the emission of an Auger electron can occur, especially in light elements. These elements are usually better detected in EEL spectroscopy. The X-rays emitted from the specimen can be recorded in an EDX detector, usually in the range from 0 to 40 keV. EDXS allows easy access to overview measurements as the whole spectrum of elements can be recorded simultaneously. Considering the multiple elements inside a typical sample (e.g. C, O, In, Sn, Si, Al, Ag, Cu, In, S in a typical FIB-cross section of a solar cell device) this allows quick identification of the elements and layers. On the other hand energy resolution in EDXS is limited and overlapping peaks can hide traces of other elements. The low thickness of thin films (50-100 nm), FIB cross sections (50-100 nm) and especially nanoparticles (often <20 nm) result in limited generation of characteristic X-rays. In combination with rather low detection efficiencies in EDXS and limited measurement time due to beam damage, recording spectra can be quite challenging.

In case of the FEI Titan these problems are severely decreased by the ChemiSTEM system. First of all, the powerful X-FEG can deliver beam currents up to the nA range, which means a significantly higher X-ray generation. Of course, the high beam current usually leads to immediate destruction of the sample. Using the new scan engine, it is possible to continuously scan a sample area with dwell times in the range of 100 μ s. Measurements over 600-1000 seconds were conducted at 1 nA without significant damage on Cu₂ZnSnSe₄ nanoparticles using this engine. Additionally the new SDD detector has a four times larger detection area than conventional Si(Li) detectors (120 instead 30 mm²) and efficiency (4-9 fold depending on the energy observed) which allows more counts to be registered.^{38,19} Using this combination EDXS can be pushed to a significantly improved level. Experimental details can be found in chapter 4.1.4.

Quantification of EDX spectra is possible using the thin film technique established by Cliff and Lorimer.³⁹

$$\frac{I_1}{I_2} = k \frac{C_1}{C_2}$$

As shown in the equation, the ratio of peak intensities (I_1 , I_2) within an EDX spectrum is correlated to the elemental composition (weight fractions C_1 and C_2) via a sensitivity factor (k-factor), which can be determined theoretically and experimentally.⁴⁰ No correction is applied for absorption or fluorescence; hence the specimen needs to fulfill the thin film criterion. Quantification was performed with Noran System Six using experimentally determined k-factors (PhD thesis Werner Grogger, 1994⁴¹). The Cu K and Zn K lines were used for quantification due to the overlap of Cu L and Zn L (and additionally Ni L from stray radiation of the specimen grid). The k factor for Cu K was interpolated from the experimental data, Zn K was determined experimentally. For Ag, Sn and In

usually the L lines were used, unless specimens contained more than one of these elements, as they overlap. In this case the corresponding K lines were used despite their lower intensities. Ag, Sn and In L were determined by interpolation as well as Ag, Sn and In K. Furthermore S K (experimentally determined) and Se L (interpolated) were used. “Filter without Standards” was chosen as quantification method in Noran System Six, “Cliff-Lorimer (MBTS) without absorption” was selected as the correction method.

In a new approach to overcome limitations of the thin film method – mainly the need for standards in multicomponent systems and the need to correct for absorption in thicker specimens – the ζ -factor method was introduced recently.⁴²

3.4.2.5 Electron Energy Loss Spectroscopy (EELS) / Energy Filtered TEM (EFTEM)

The inelastic scattering process mentioned before causes electrons to lose energy when interacting with matter. The energy released by transferring one electron from a higher energy level to a lower one is highly specific and can be seen in the peaks in an EDX spectrum. This is different when looking at the energy required for ejecting an electron from the shell of an atom. A minimum energy is required for this process, which is called the critical ionization energy, but it may be higher. As a consequence ionization edges are observed in EELS^{43,44} instead of peaks. The chemical environment of the atom is reflected in the fine structure of these edges. The ionization edges (also called high-loss) are not the only information that can be gathered with EEL spectroscopy. The so-called low-loss region (<100 eV) features plasmon peaks and at 0 eV the zero loss peak can be observed. While the zero loss (ZL) peak is not an interesting target for EELS, zero loss filtering can enhance BF-TEM images by excluding electrons that have been inelastically scattered, leaving only electrons that have not interacted with the beam at all, or that have been elastically scattered. This can help improving the image quality, especially in cases where the specimen is slightly too thick and multiple scattering starts to occur. ZL Filtering removes all multiple scattered electrons that had at least one inelastic interaction. An example is shown in Figure 8 for BF TEM and HRTEM images of a FIB lamella of a CIS/MDMO-PPV device taken with and without zero loss filtering. In both cases more details can be seen in the ZL filtered images, which look less blurry.

Zero loss filtering is a special case of Energy Filtered TEM (EFTEM).^{45,46} Recording images before and after the EELS edge allows the calculation of elemental maps or jump ratio images. Compared to elemental maps spectrum images EFTEM images allow higher spatial resolution. Both EELS and EFTEM require thin samples, a criterion matched very well by the thin films prepared on NaCl single crystals as well as the nanoparticles immobilized on carbon films. It is also possible to prepare adequately thin cross sections from FIB for EELS and EFTEM investigation.²¹

Beam broadening can in some cases, especially in thicker specimens, decrease the spatial resolution in EDXS compared to EELS,⁴⁷ making it easier to prove the presence or absence of chemical elements at a specific location within the sample in EELS. However, considering the multi-element composition of the specimens, EELS edges are very likely to overlap. As an example, the extraction of the Zn-L edge in $\text{Cu}_2\text{ZnSnS(e)}_4$ can be problematic because of the overlap with the Cu-L edge. Carbon from the sample (plus additional carbon from contamination) can have severe impact on the measurements as well. Some elements (e.g. S) also have no edges, that can be recorded in a useful way (L_{23} @165 eV cannot be extracted properly; K @ 2472 eV has too little intensity). On the other hand, elements that can effectively be recorded with EELS require lower dwell times than in EDXS, which leads to better results with respect to resolution and beam damage. Chapter 4.6.1 shows details for STEM-EELS (using only the Cu and In edges) and STEM-EDXS.

The challenges described for EELS also apply for EFTEM. In practice STEM-EELS was preferred most of the time, as the extraction of background and signal can be adjusted with respect to overlapping edges and other effects after recording of the image. Additionally specimen drift is often an issue – especially at high magnifications – which is another downside for EFTEM, as the images recorded start to smear, whereas the drift can be corrected in STEM-EELS.

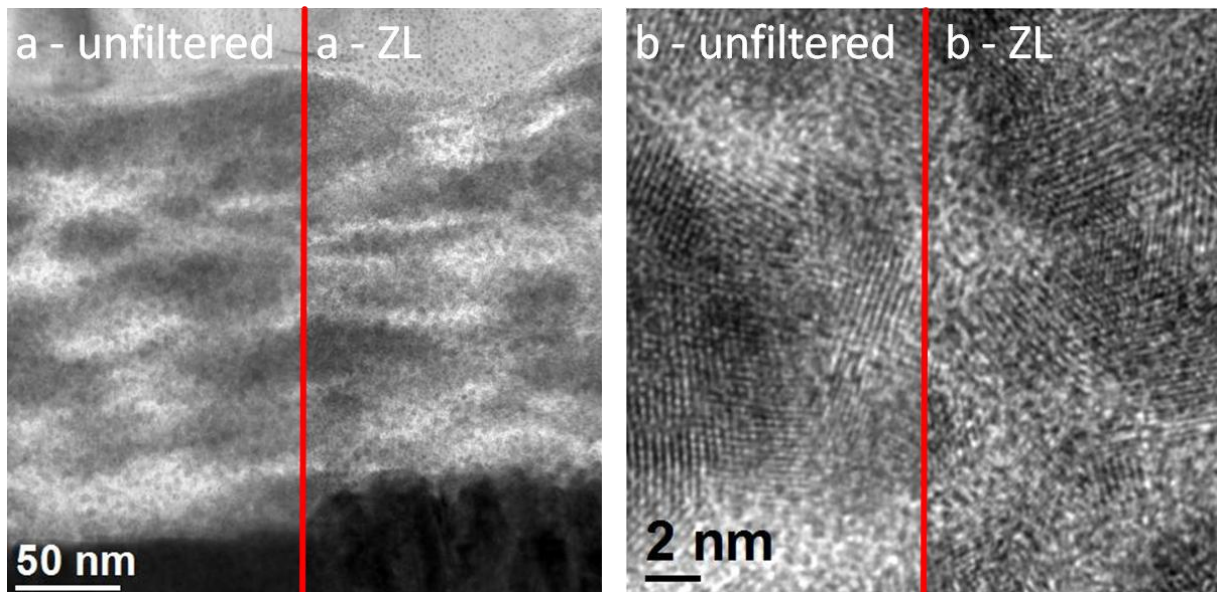


Figure 8: Comparison between unfiltered TEM images of a CIS/MDMO-PPV device: TEM image showing the cross section of the nanocomposite layer (a), HRTEM image of CIS crystals in the nanocomposite layer (b).

Due to these circumstances EFTEM was mostly used for FIB cross-sections with known elements at lower magnifications with good results.

3.4.2.6 Beam damage

Exposure to the electron beam leads to beam damage.⁴⁸ There are multiple mechanisms involved, such as heating, knock-on damage, ionization damage, sputtering and contamination with hydrocarbons. In case of nanocomposites consisting of inorganic nanoparticles and organic polymers, the polymers were affected at a much earlier stage than the inorganic phase.

Figure 9a shows the damaged area after illumination of the central area. While the polymer is melting, the inorganic agglomerations are still present and seem to be mostly unchanged. The polymer (P3EBT) in figure 9b is already melting; the lattice fringes of several CdS nanoparticles can still be seen. At least in TEM mode, the polymer is a good indicator for beam damage, while the inorganic phase is still intact. As a consequence of these observations beam damage could be avoided in TEM mode by carefully observing the polymer for first signs of beam damage. In these cases measurements were continued on a different, undamaged area of the polymer.

In STEM mode, especially on the FEI Titan, damage to the inorganic phase due to the much more concentrated beam was noticed and steps were taken to reduce it (see chapter 4.1.4). In general, attention was paid to avoid beam damage by comparing the area of interest before and after investigation. Contamination with hydrocarbons was discussed previously in chapter 3.1.4.

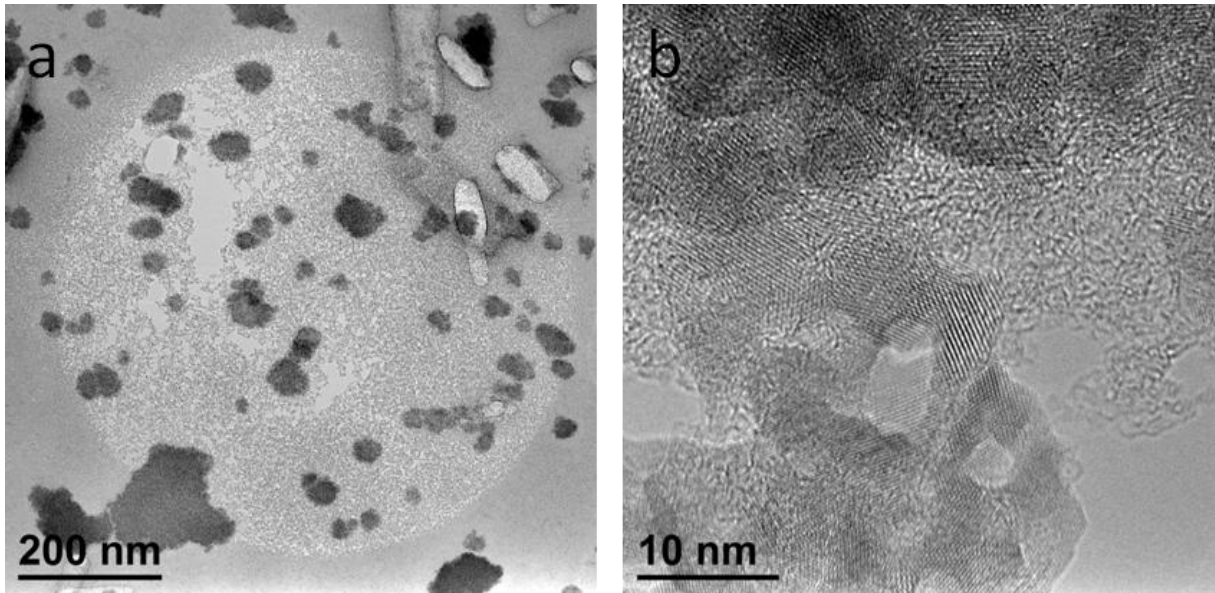


Figure 9: Beam damage after illumination in TEM mode of a CIS/PPV specimen (see chapter 4.4.2) (a); nanoparticles in HRTEM remain crystalline even though polymer is melting in CdS/P3EBT (see chapter 4.4.1) (b).

3.4.2.7 Conclusions

A wide range of methods for investigation in the TEM is available. At the same time the questions raised within the project require more than a single approach and method. TEM-BF is a versatile method for the quick investigation of specimens in comparative studies such as the layer structure of nanocomposite cells (e.g. layer thickness) or the size and shape of CZTS(e) nanoparticles. HRTEM is a useful method for the investigation of crystalline nanoparticles and can reveal d-spacings and defects. Similar to XRD SAED is a useful standard tool for determining the crystal structure.

For advanced investigations of CZTS(e) STEM-DF enables the identification of defects. STEM-HAADF and its Z-contrast mechanism is an ideal method for specimens with variations in the average Z – ideal for FIB cross sections with varying Z, like it can be found in a nanocomposite solar cell.

For analytical investigations EDXS and EDXS SI are often the preferable method due to their ability to identify all present elements at once. However, in spectrum imaging EDXS usually requires a significant amount of measurement time. In situations where the desired analytes are already known and have edges below 1 keV EELS SI can be considered a great alternative allowing faster measurements at higher resolution than in EDXS SI due to higher signal intensities. Under these conditions EFTEM can also yield results that show better spatial resolution than EELS SI.

At the end of the day – or often in the beginning of it - one of the most important questions is which method is going to deliver the most useful information about the specimen. The results of this work show, a variation of methods was used depending on the scientific question raised within the project.

4 Experimental Part

4.1 Investigations on $\text{Cu}_2\text{ZnSnS}(\text{e})_4$ nanoparticles

4.1.1 Introduction

Two nanoparticle systems were investigated in this work: CuInS_2 , which is also used as the inorganic phase in the solar cells and $\text{Cu}_2\text{ZnSnS}(\text{e})_4$, which has recently gained focus as an alternative to the indium based materials.

Using advanced electron microscopy it is possible to gain knowledge about a variety of properties needed to characterize nanoparticles – size and shape (TEM-BF), crystal structure and defects (SAED, HRTEM) and chemical composition (EDXS/EELS/EFTEM).

4.1.2 $\text{Cu}_2\text{ZnSnS}(\text{e})_4$ – optimizing the synthesis of stoichiometric nanoparticlesⁱ

$\text{Cu}_2\text{ZnSnSe}_4$ nanoparticles have high potential to be used as nanocrystal ink for printable solar cells. Using transmission electron microscopy we show that these nanoparticles exhibit a broad range of chemical heterogeneity. These results are contrary to the interpretation of previous experimental work in literature and will have considerable impact on the development of these nanoparticles.

Copper zinc tin chalcogenides have attracted significant attention over the last years owing to their interesting photoelectric properties.⁴⁹ As they consist of low-cost and readily available elements, they have high potential for mass production as solar absorber material.⁵⁰ Consequently, much work has been devoted to the preparation of these materials in the form of thin films. Various methods have been suggested such as co-evaporation,⁵¹ sulfurization/selenization of metal precursor films⁵² and thermal annealing of solution based precursors.⁵³

However, copper zinc tin chalcogenide nanoparticles have been recognized only recently as a promising alternative to thin films. During the last two years, $\text{Cu}_2\text{ZnSnS}_4$ and $\text{Cu}_2\text{ZnSnSe}_4$ nanoparticles have been successfully prepared using colloidal synthesis routes.^{54,55,56,57,58} A key issue often unaddressed in these studies and to our opinion still unanswered is the chemical homogeneity of these nanoparticles. Although authors of previous studies state that their nanoparticles have a homogeneous chemical composition, there is some evidence in the experimental results of previous work that the copper zinc tin chalcogenide nanoparticles show a certain range of chemical heterogeneity.

However, the chemical composition strongly influences the absorber properties of copper zinc tin chalcogenide nanoparticles,⁵⁹ and therefore a detailed quantitative study of the chemical composition of individual nanoparticles is called for. Previous investigations in literature by means of X-ray and electron diffraction are difficult to interpret when considering the structural similarity of these quaternary compounds to the binary and ternary chalcogenides of the same elements. Therefore, X-ray and electron diffraction cannot easily distinguish between these phases and generally only yield information about a large number of particles.

The composition of individual $\text{Cu}_2\text{ZnSnS}(\text{e})_4$ nanoparticles is investigated using TEM in combination with EDXS and EELS.⁶⁰ Due to its excellent spatial resolution which is in the nanometer range, this method allows the detailed chemical analysis of nanostructured materials and even individual nanoparticles.⁶¹

ⁱ Parts of this chapter are already published in: Haas, W.; Rath, T.; Pein, A.; Rattenberger, J.; Trimmel, G.; Hofer, F. *Chemical communications* **2011**, 47, 2050 and Rath, T.; Haas, W.; Pein, A.; Saf, R.; Maier, E.; Kunert, B.; Hofer, F.; Resel, R.; Trimmel, G. *Solar Energy Materials and Solar Cells* **2012**, 101, 87.

Table 3 gives an overview of the samples investigated in this work and the reactants used for synthesis. Different combinations of metal salts were used in an attempt to synthesize nanoparticles with stoichiometric composition. Furthermore, in A-Se-TOPO trioctylphosphineoxide (TOPO) was added to the reaction.

Table 3: Reactants used for synthesis of samples A-S, A-Se, A-Se-TOPO, B-Se and C-Se

Sample	reactants
A-S	CuI, ZnCl ₂ , SnI ₄ , S
A-Se	CuI, ZnCl ₂ , SnI ₄ , Se
A-Se-TOPO	CuI, ZnCl ₂ , SnI ₄ , Se, TOPO
B-Se	CuI, ZnI ₂ , SnI ₄ , Se
C-Se	CuOAc, ZnI ₂ , SnOAc ₄ , Se

Samples A-S and A-Se were synthesized using the same reactants (CuI, ZnCl₂, SnI₄ and S/Se). Figure 10 shows TEM-BF, SAED and HRTEM images for A-S and A-Se. The nanoparticles in A-S are between 7-10 nm in size, while the nanoparticles in A-Se are larger (14-18 nm). This data is consistent with primary crystallite sizes estimated from X-Ray Diffraction (XRD) line width using the Scherrer formula (see table 4). Crystallographic investigations were done with both XRD and SAED (see figure 11a). Results of both methods match very well with the reference data. Deviations for d-values gained from SAED using a radial intensity profile were around 1% which is in accordance for the method used and described before.³⁷ There is a good match between the XRD and SAED data and the reference files (JCPDS 26-0575 for CZTS, JCPDS 52-868 for CZTSe). However, the quality of measurements cannot overcome the fact that the binary and ternary selenides have similar structure and diffraction peaks, e.g. Cu₂SnSe₃ (JCPDS 89-2879), Cu₂Se (JCPDS 88-2043), ZnSe (JCPDS 37-1463). The XRD reference for Cu₂SnSe₃ is also shown in figure 11. Binary and ternary selenides have similar structure and diffraction peaks, e.g. Cu₂SnSe₃ (JCPDS 89-2879), Cu₂Se (JCPDS 88-2043), ZnSe (JCPDS 37-1463). Due to these similar patterns distinction cannot easily be made based on XRD and SAED, but only by chemical analysis.

Table 4: Primary crystallize sizes (XRD-Scherrer) and particle sizes (TEM) of the prepared nanoparticle samples.

Sample	prim. cryst. size (nm)	particle size (nm)
	XRD - Scherrer	TEM
A-S	7	7-10
A-Se	18	14-18
A-Se-TOPO	23	25-35
B-Se	13	15-25
C-Se	18	15-25

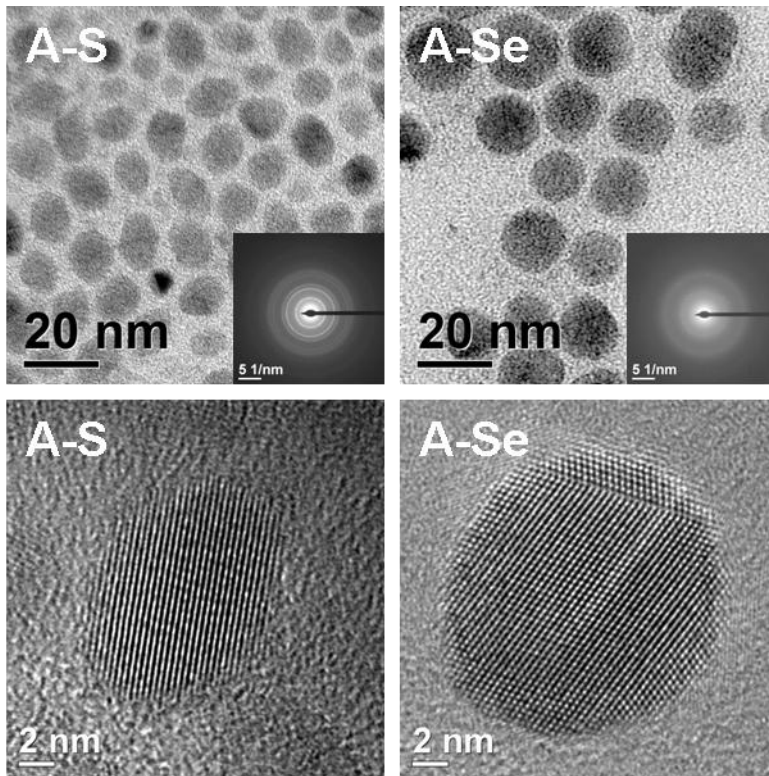


Figure 10: TEM-BF, SAED and HRTEM images for nanoparticles A-S and A-Se.

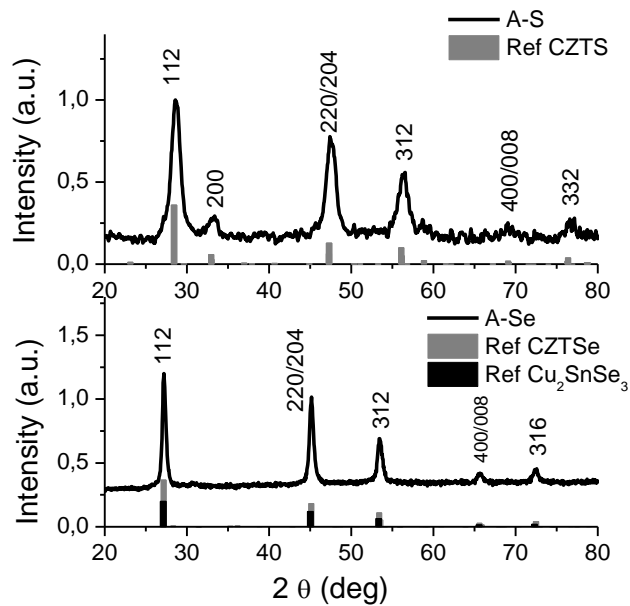


Figure 11: X-ray diffraction patterns of A-S and A-Se. The peaks are in good agreement with the reference patterns of CZTS (PDF 26-0575) and CZTSe (PDF 52-868 – grey lines) or Cu_2SnSe_3 (PDF 89-2879 – black lines). The corresponding indexation is given; measured by T. Rath.

In figure 12 the EDX spectra for A-S and A-Se are shown. The almost complete absence of Zn can be seen. Subsequent quantification shows that the composition is far off the stoichiometric $\text{Cu}_2\text{ZnSnSe}_4$ and closer to Cu_2SnSe_3 – which has already been identified as one of the possible matches in XRD.

While the composition of the nanoparticles was found to be almost stoichiometric for $\text{Cu}_2\text{ZnSnSe}_4$, the synthesis had to be optimized for $\text{Cu}_2\text{ZnSnSe}_4$ before a sample with nearly stoichiometric composition was synthesized (C-Se).

Table 3 shows the reactants used in the synthesis of the $\text{Cu}_2\text{ZnSnSe}_4$ (A-S) and $\text{Cu}_2\text{ZnSnSe}_4$ (A-Se – C-Se) nanoparticles and their chemical composition according to overview measurements using TEM-EDXS (A-S, A-Se, A-Se-TOPO, B-Se) or SEM-EDXS (C-Se) respectively.

Data was acquired on a Philips CM20 (200 kV, LaB_6 cathode, Noran HPGc detector) by collecting EDX spectra for multiple (100-150) nanoparticles and quantification of the Cu K, Zn K, Sn L, S K/Se K peaks using the thin-film technique.³⁹

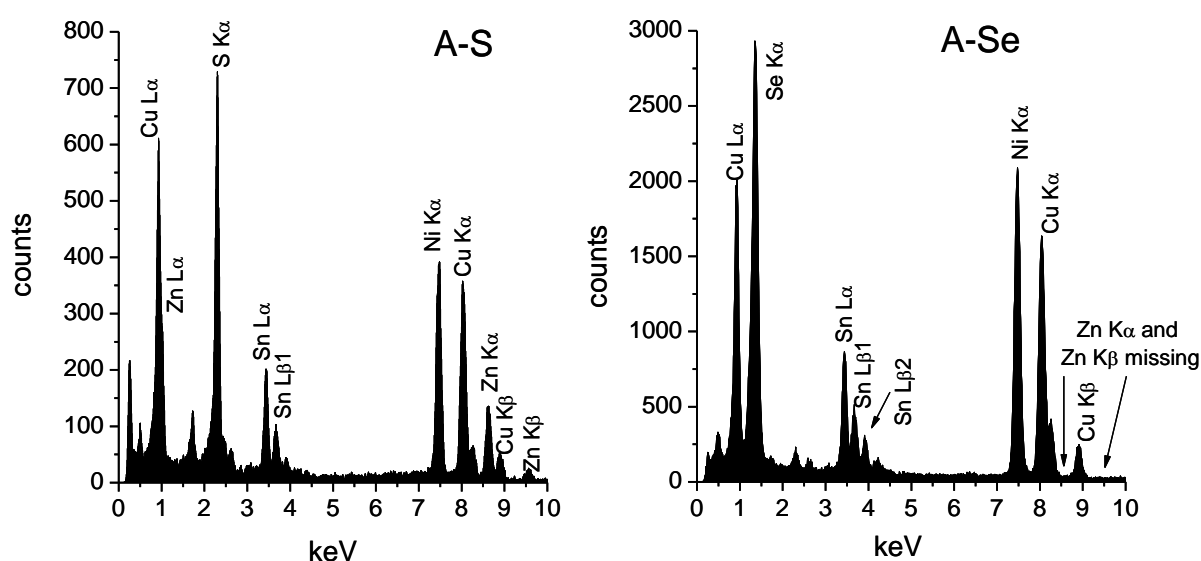


Figure 12: TEM-EDXS overview spectra for A-S and A-Se. The Zn K-line is absent in A-Se.

Table 5: Chemical composition found in TEM-EDXS for $\text{Cu}_2\text{ZnSnSe}_4$ (A-S) and $\text{Cu}_2\text{ZnSnSe}_4$ (A-Se – C-Se)

sample	Cu (at%)	Zn (at%)	Sn (at%)	S or Se (at%)
stoichiometric	25.0	12.5	12.5	50.0
A-S	23.8±0.8	12.7±0.4	12.2±0.3	51.3±1.2
A-Se	31.0±9.8	1.1±0.5	20.2±3.7	47.7±5.6
A-Se-TOPO	37.6±2.9	0.7±0.3	18.0±0.9	43.7±1.3
B-Se	26.1±2.0	4.6±0.4	24.0±2.7	45.3±4.6
C-Se	26.3±0.3	10.6±0.0	14.2±0.8	48.9 ±0.4

As the TEM-EDXS analysis (see table 5) revealed a lack of Zn in A-Se, the synthesis was altered. Addition of TOPO, while yielding larger nanoparticles, had no significant impact on the chemical composition. Introducing Zn as iodide increased the Zn content from 1.1 to 4.6 at% instead of 12.5. Suppressing the activity of Cu and Sn by using the corresponding acetate ions finally yielded an almost stoichiometric Zn content of 10.6 at%.

Figure 13 shows TEM-BF, SAED and HRTEM for A-Se-TOPO, B-Se and C-Se. Particle size from TEM and XRD using the Scherrer formula is shown in table 4. In general, the Se-samples show a higher particle size than A-S, however, there is a discrepancy between the primary crystallite size and the size of the particles in TEM measurements. This can be explained by the presence of defects within the nanoparticles. As the images in figure 10 and figure 13 show, twinning appears in almost all Se samples. While the smaller nanoparticles in A-Se have only one twin interface, larger ones such as A-Se-TOPO exhibit multiple twin interfaces. Especially A-Se-TOPO and B-Se show high concentrations of twin defects, which may stem from stacking faults.⁶² This lamellar twinning, visible as a kind of zigzag surface structure,⁶³ can be seen very clearly in the HR-TEM image of sample A-Se. XRD data (not shown) for A-Se-TOPO, B-Se and C-Se SAED match very well to the reference data for CZTSe (JCPDS 52-868) and Cu_2SnSe_3 (JCPDS 89-2879). The Raman spectrum of sample C-Se is depicted in figure 14. All main peaks ($173/191/232\text{ cm}^{-1}$) can be attributed to $\text{Cu}_2\text{ZnSnSe}_4$. Using peak fitting two small peaks from other phases could be identified using reference data from literature:⁶⁴ Cu_2SnSe_3 at 184 cm^{-1} and Cu_xSe_y at 262 cm^{-1} . This measurement confirms the presence of $\text{Cu}_2\text{ZnSnSe}_4$ in the sample. However, just like SEM-EDXS or XRD, Raman measurements can only be used as an integral method over a large area.

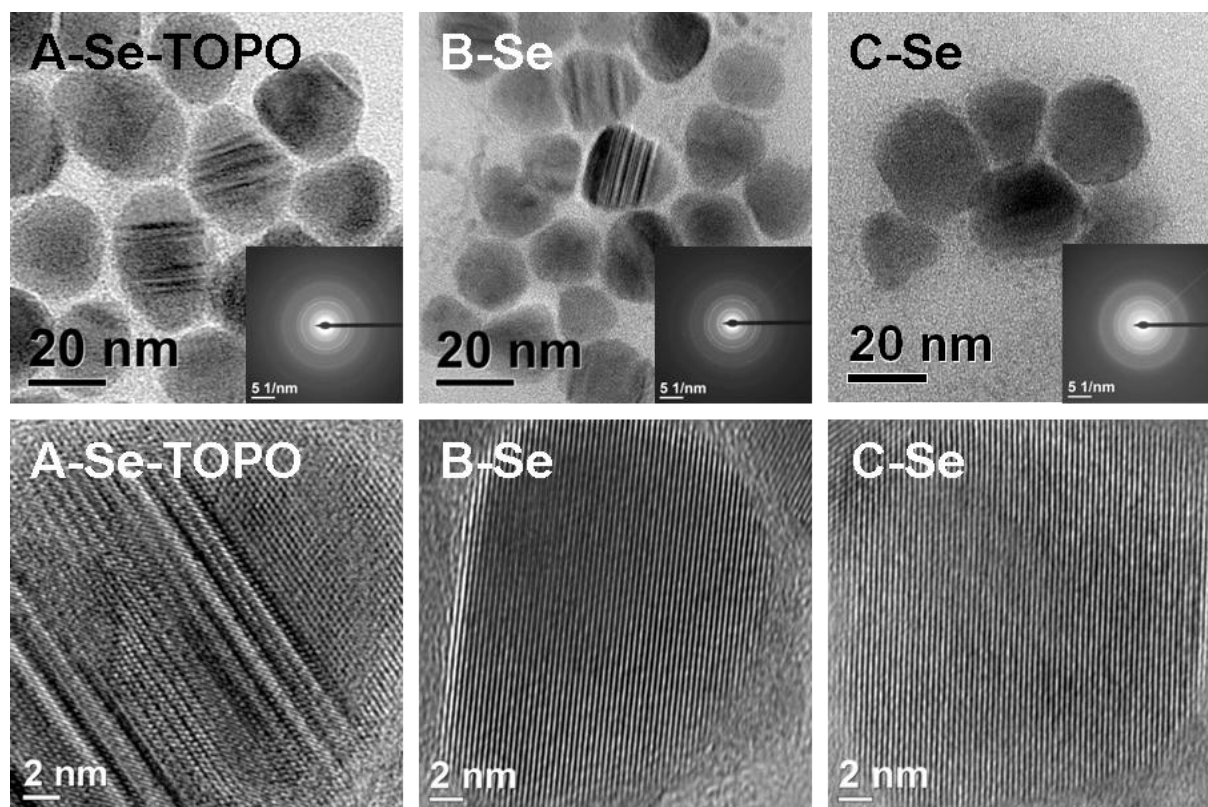


Figure 13: TEM-BF, SAED and HRTEM images for nanoparticles A-Se-TOPO, B-Se and C-Se.

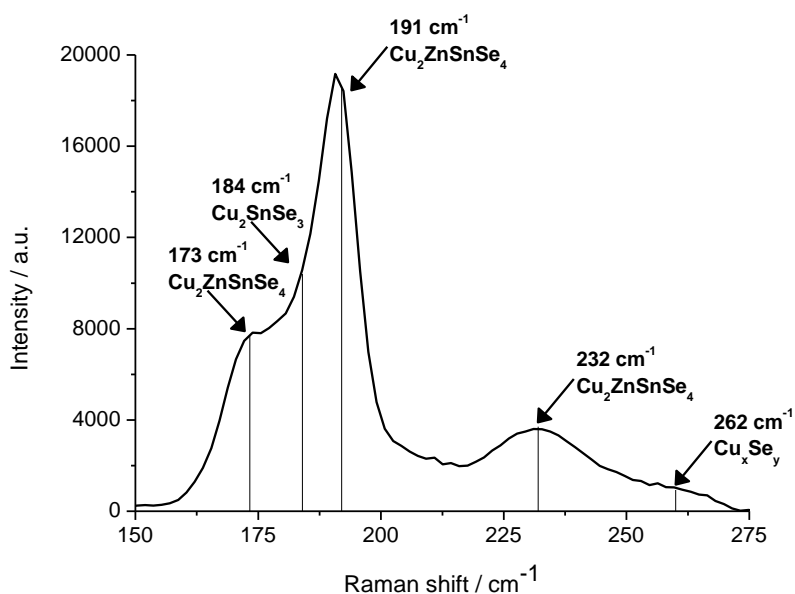


Figure 14: Raman spectrum for sample C-Se; measured by B. Chernev.

Figure 15 shows STEM-DF and STEM-HAADF images for Se-A-TOPO recorded at a camera length of 100 mm. In the STEM-DF image defects in many of the nanoparticles are visible. The defects can also be observed in TEM-BF, however it is often necessary to tilt the sample as only a small amount of defects is visible at each tilting angle. STEM-DF allows the quick identification of defects even without tilting. When using the HAADF detector at this camera length only small variations are visible in the HAADF image due to chemical inhomogeneity. Defects inside the nanoparticles are almost invisible except for the nanoparticle in the lower left corner.

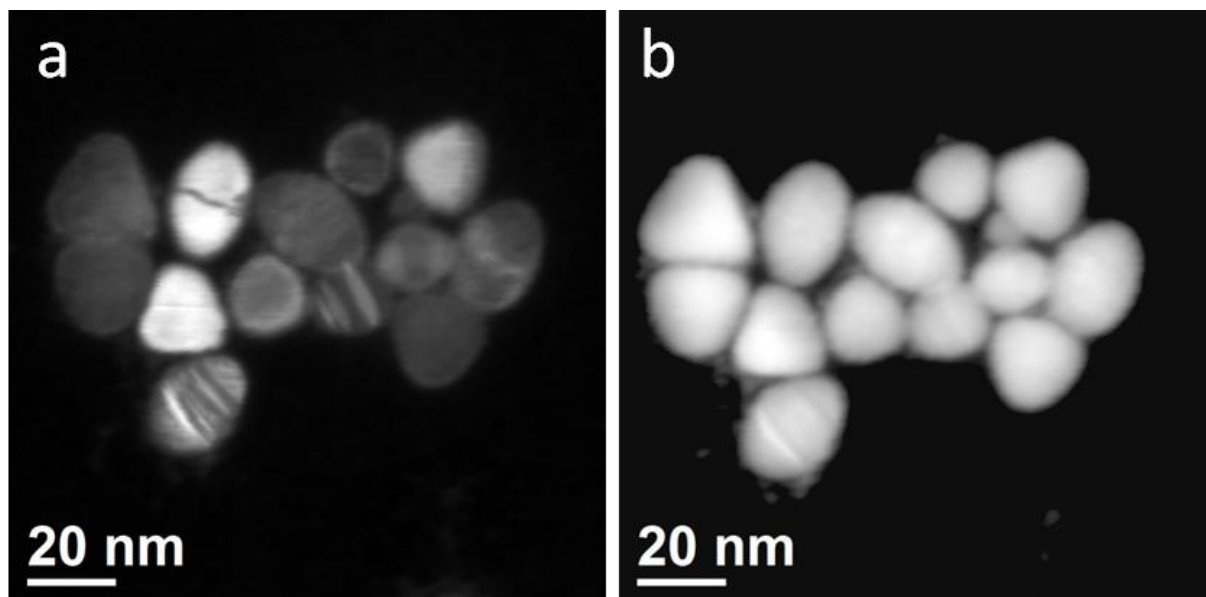


Figure 15: STEM-DF (a) and STEM-HAADF (b) images for A-Se-TOPO recorded at a camera length of 100 mm.

4.1.3 Detailed analysis of chemical inhomogeneity in CZTSe nanoparticles

A detailed analysis was carried out on the almost stoichiometric sample C-Se to gain deeper understanding of the chemistry and methodology to study it.

The chemical composition of the nanoparticles was investigated by SEM-EDXS over an area of 300 x 225 μm^2 . For measurements on three different spots the average composition was Cu 26.3, Zn 10.6, Sn 14.2 Se 48.9 at% with only little variation between the measurements (see table 6 for details). The composition of the bulk phase is almost stoichiometric and matches very well with the SEM-EDXS results reported on a similar synthesis by Wei et al.⁵⁵ In agreement with these results a decrease for Zn and an increase of Sn levels also appears in the nanoparticles prepared by our synthesis. This may be explained by differences in the reactivity of the precursor materials. Additionally, images of the regions scanned for SEM-EDXS were also recorded using a secondary electron and backscatter electron detector (see figure 16). The backscatter images show only very little variation in brightness, which implies a homogeneous composition in the micrometer range.

Table 6: Overview elemental analysis in at% for nanoparticles obtained by SEM-EDXS (SEM1-SEM3) including average and standard deviation (std).

#	Cu / at%	Zn / at%	Sn / at%	Se / at%
SEM 1	25.9	10.6	15.1	48.4
SEM 2	26.4	10.6	13.8	49.1
SEM 3	26.5	10.6	13.8	49.1
average	26.3	10.6	14.2	48.9
std	0.31	0.02	0.76	0.43

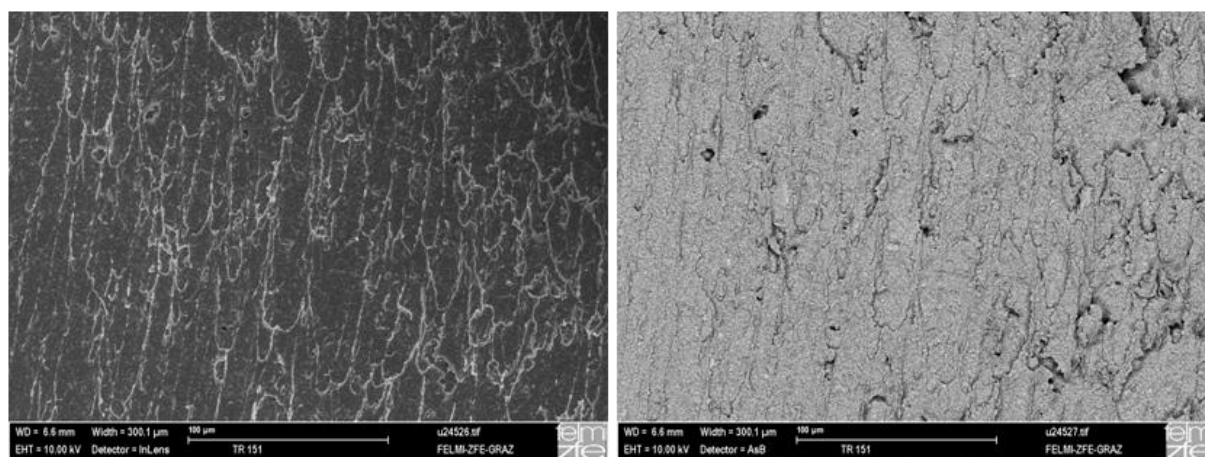


Figure 16: Secondary electron and Backscatter electron images for SEM-EDXS measurement of C-Se (SEM 1, table 6).

Contrary to SEM-EDXS measurements STEM using a HAADF detector combined with EDXS and EELS allows the investigation of single nanoparticles even with high spatial resolution. For our study we decided to record EDX and EEL spectra of individual nanoparticles. Three particles and the corresponding EDX and EEL spectra are shown in the STEM-HAADF image in figure 18.

All in all for 20 nanoparticles (shown in figure 17) an EDX and EEL spectrum was recorded by placing the probe on the particle. EDX spectra were used for quantification (see table 7). EEL spectra were recorded with a dispersion of 0.2 eV in the region from 810 to 1220 eV, which features the Cu-L edge (930 eV) and the Zn-L edge (1020 eV). Background subtraction using power law was used to extract the signal for both edges. However the edges overlap, which complicates the extraction of the Zn edge; therefore the edges can only be used for qualitative confirmation of the results from TEM-EDXS.

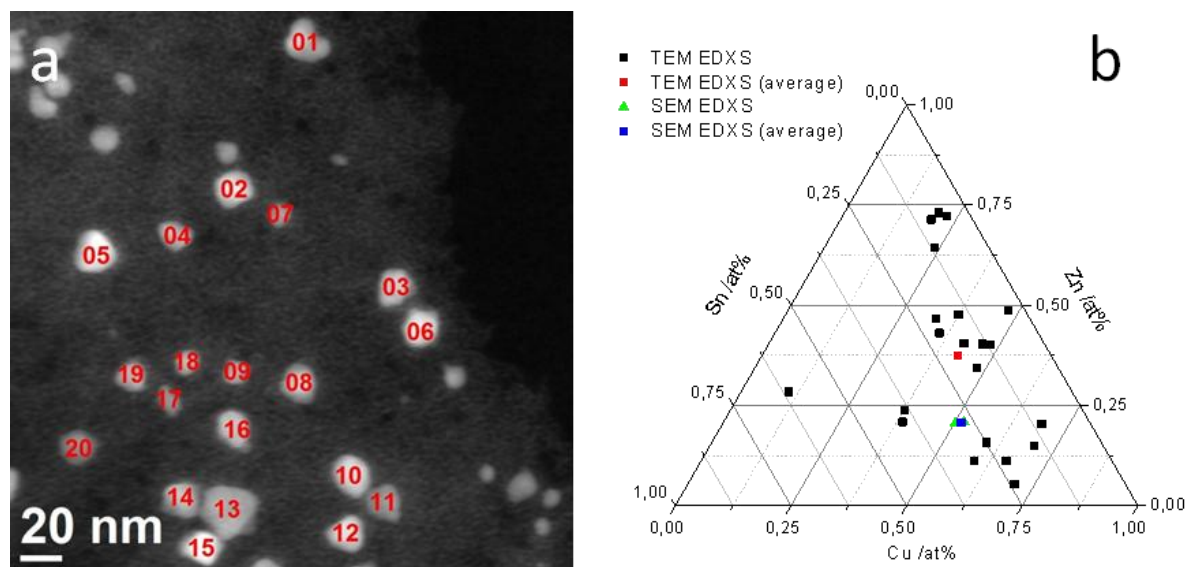


Figure 17: STEM-HAADF of sample C-Se; image of used area for measurement of 20 individual nanoparticles (a). Ternary diagram featuring individual composition for the 20 nanoparticles (TEM-EDXS) and average as well as the results from SEM-EDXS (b).

Table 7: Elemental analysis in at% of individual nanoparticles (see figure 17) obtained by TEM-EDXS including average (aver) and standard deviation (std) for all 20 nanoparticles.

#	Cu	Zn	Sn	Se	#	Cu	Zn	Sn	Se
1	35	10	5	49	11	15	21	9	56
2	25	25	2	49	12	27	5	14	54
3	16	20	10	54	13	18	23	7	51
4	24	21	7	49	14	12	42	4	43
5	12	33	6	48	15	12	40	3	45
6	26	7	11	56	16	23	16	8	53
7	17	11	18	54	17	9	34	4	52
8	33	2	11	53	18	20	20	8	51
9	18	10	19	53	19	25	21	6	48
10	33	7	7	53	20	33	6	11	50
aver	21.7	18.7	8.5	51.0	std	7.9	11.7	4.5	3.5

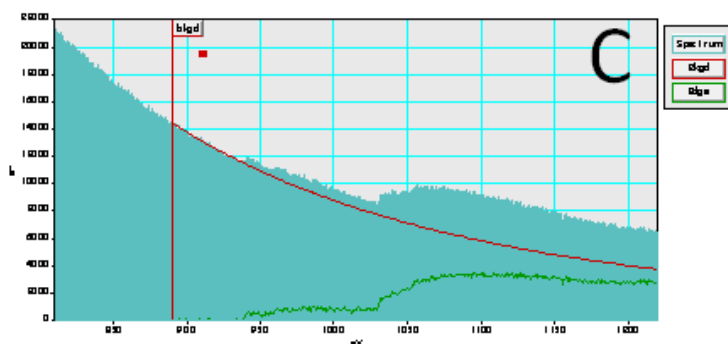
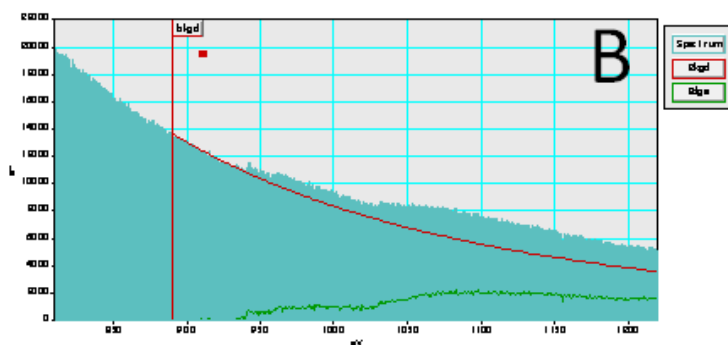
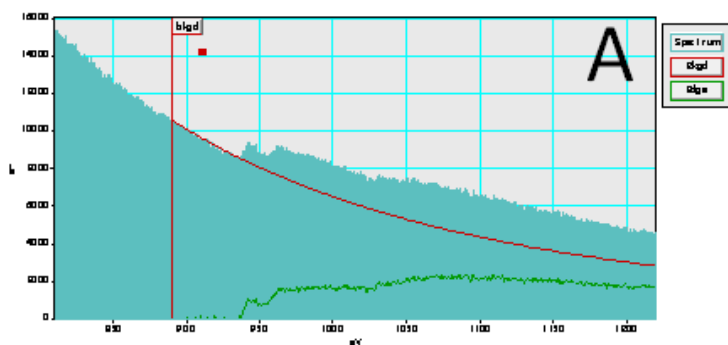
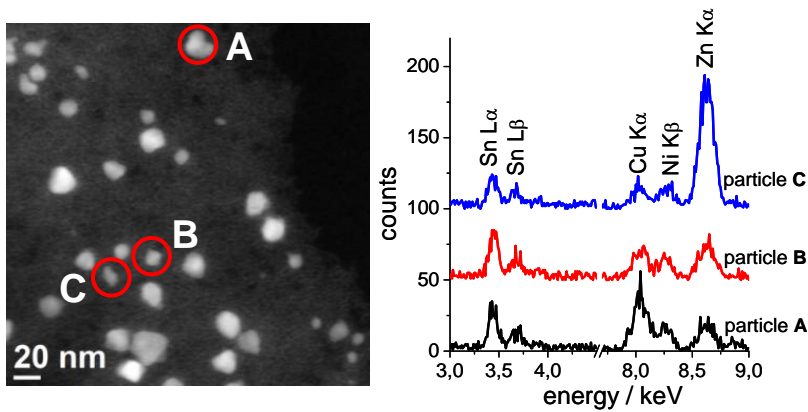


Figure 18: STEM-HAADF image of $\text{Cu}_2\text{ZnSnSe}_4$ nanoparticles C-Se and EDX and EEL spectra for a selected copper- (A), tin- (B) and zinc-rich (C) nanoparticle. The differences in EDXS peak height are caused by the variations in chemical composition. The Ni-peak is caused by stray radiation from the sample grid. The EEL spectra show the Cu L edge at 931 eV overlapped by the Zn L edge at 1020 eV.

The data in table 7 clearly show, that the Cu:Zn:Sn:Se ratio varies over a broad range. Exemplarily, the EDX spectra for each of one Cu-, Zn- and Sn-rich nanoparticle are shown in figure 18. In each of the three spectra the characteristic peak for one of the elements is increased. The elemental compositions in table 7 show a strong exchange of Cu, Zn and Sn with each other. Zn and Sn can be found in a range from almost complete absence (approx. 2 at%) up to more than 40 at%. Cu also covers a range from 9 to 35 at%. Our data show no trends with respect to preferred compositions, i.e. it seems that every nanoparticle has its own stoichiometry. This is also visualized in the ternary diagram in figure 17. The ratio between (Cu+Zn+Sn) and Se remains in the range of stoichiometric composition with Se values between 43 and 56 at%. When comparing the SEM-EDXS results to the average values for the 20 measurements differences especially for the Zn and Sn content of the nanoparticles can be found. Considering the large standard deviation of the values and the fact that due to the inhomogeneity the sample size of 20 is not representative of the whole sample the average value is still in good accordance. In addition to EDXS measurements EEL spectra of the Cu-L and Zn-L edge were recorded simultaneously. Due to overlaps in these two edges, data was only analyzed on a qualitative basis, but the spectra confirm the variations in the Cu/Zn ratio measured in EDXS.

At first glance these results are contrary to the results on $\text{Cu}_2\text{ZnSnSe}_4$ nanoparticles reported by other groups. To our best knowledge there is only one existing publication featuring stoichiometric $\text{Cu}_2\text{ZnSnSe}_4$ nanoparticles so far, but no investigations on lateral elemental distribution have been reported there.⁵⁵ However, a closer look on EEL spectrum imaging data of non-stoichiometric $\text{Cu}_2\text{ZnSnSe}_4$ nanocrystals presented by Shavel et al.⁵⁴ reveals that the Sn/Se ratio has some variations. Similar conclusions can also be drawn from the corresponding quaternary sulfide nanoparticles, $\text{Cu}_2\text{ZnSnS}_4$, as a careful review of the EDX spectrum images of $\text{Cu}_2\text{ZnSnS}_4$ reported by Steinhagen et al.⁵⁶ uncovers a slight but clearly visible spatial separation which can be seen best in the distribution of Zn and Sn, but affects all elements. Judging from our own results and from reevaluation of the existing literature we assume that the variation in content of elements to be a characteristic feature of these types of synthesis for the quaternary chalcogenide systems $\text{Cu}_2\text{ZnSnS}_4$ and $\text{Cu}_2\text{ZnSnSe}_4$.

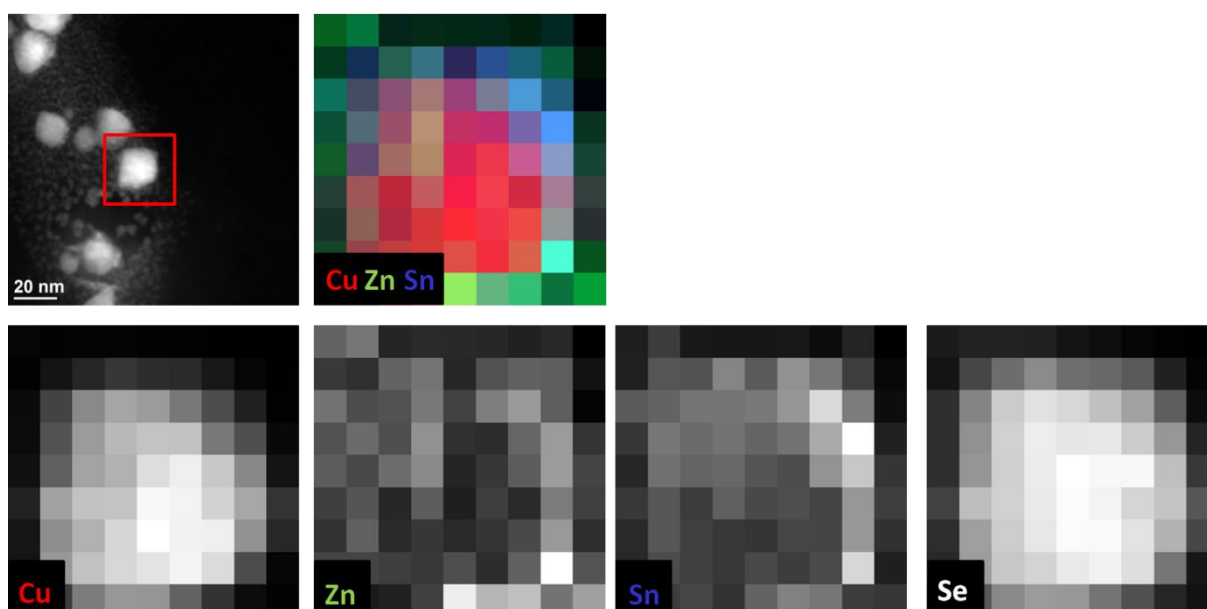


Figure 19: Spectrum image for C-Se on the Tecnai F20. STEM-HAADF image (top left), composite image for Cu/Zn/Sn and individual chemical maps (lower panel) extracted from EDXS mapping.

In addition to the EDX and EEL spectra of individual nanoparticles an EDX spectrum image was recorded for specimen C-Se on the Tecnai F20. A live time of 40s per pixel was chosen (overall recording time including dead time and drift correction 75 minutes). At 9 x 9 pixels with a pixel size of 2.5 nm a field of view of 22.5 x 22.5 nm was covered, the probe current was 85 pA. Figure 19 shows the resulting chemical maps extracted from the EDXS data. Resolution is however limited, hence this result has to be interpreted with care. There is a good overlap between the Cu- and Se- maps. On the other hand Zn and Sn are localized rather outside the core of the particle than inside. While this coincides nicely with the previous findings about the chemical inhomogeneity of the nanoparticles, investigating just a single nanoparticle takes over an hour – more detailed studies would require a significant amount of measurement time. Additionally, with a relatively long live time of 40s, it is possible that the nanoparticle has been changed by the long term exposure to the electron beam. Therefore it was important to check for eventual changes by recording STEM-HAADF images before and after the investigation, as shown in figure 20. The nanoparticle looks similar in size and shape, some change are visible as well as a halo of contamination around the nanoparticle.

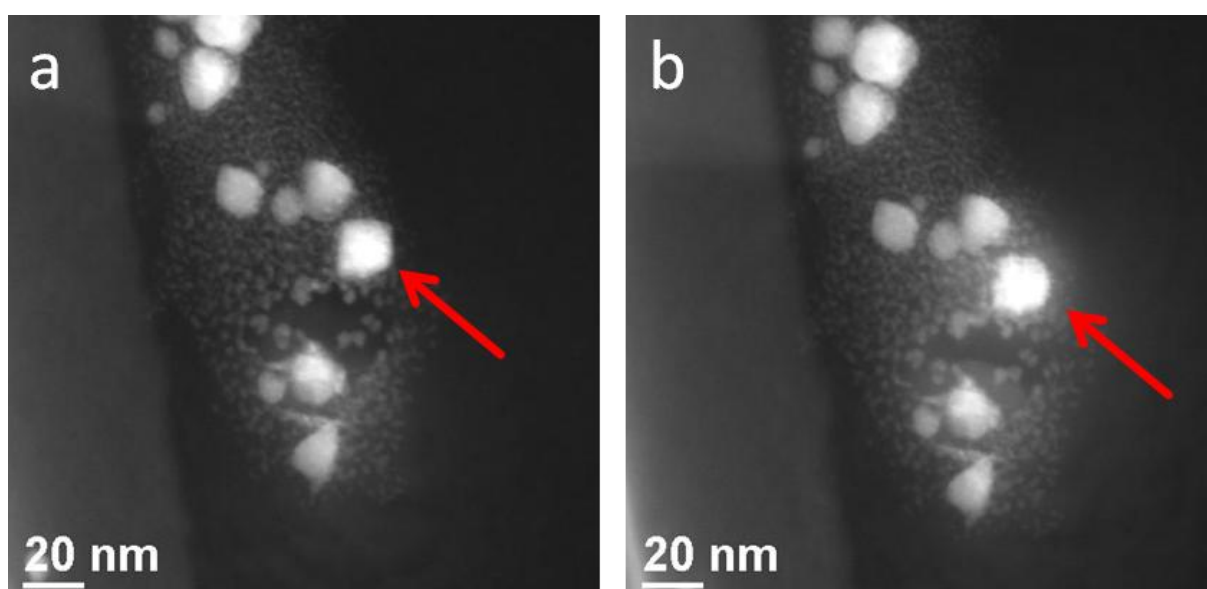


Figure 20: STEM-HAADF image before (a) and after (b) spectrum imaging for specimen C-Se. The indicated nanoparticle was investigated.

In conclusion, $\text{Cu}_2\text{ZnSnSe}_4$ nanoparticles produced via a modified version of the recently popular wet chemical oleylamine synthesis routes were analyzed with respect to their composition. Overview measurements show a good stoichiometric composition, but measurements of individual nanoparticles show a large variation in the content of Cu, Zn and Sn. This was confirmed using two independent techniques, EDXS and EELS. A critical review of existing literature indicates that this effect applies in general to current syntheses of both $\text{Cu}_2\text{ZnSnS}_4$ and $\text{Cu}_2\text{ZnSnSe}_4$ nanoparticles. The results gained from EDX spectrum imaging of a single nanoparticle strongly suggest inhomogeneity inside the nanoparticles, however due to limited resolution, slow measurement times and issues with potentially changing the chemistry of the nanoparticles during the measurement, further measurements were necessary on the FEI Titan.

4.1.4 Analyzing chemical inhomogeneity on the Titan platform

A new batch of nanoparticles (A-Se-TOPO 2) was synthesized using the same procedure as for A-Se-TOPO. Even though the same protocol was used, smaller nanoparticles than in the initial sample were isolated during work-up.

First experiments were performed on a FEI Titan³ with ChemiSTEM technology and probe Cs corrector at 300 kV using the Bruker Esprit software package. The main features of the new EDXS system are listed in table 8. The beam current of the Titan can easily be adjusted by simply changing the focus of the monochromator lens. Depending on the focus fewer or more electrons enter the condenser system. The big advantage of this method is that, unlike other methods of changing the beam current, such as changing the spot size, the monochromator focus has no significant impact on the course of the electron beam. Hence all alignments including those of the Cs-corrector stay intact and the beam current can be changed on the fly without the need to realign the microscope.

Table 8: Main features of the new EDXS detector used in the FEI Titan.³⁸

Type	SDD
# of detectors	4
Window	Windowless
Detector area	120 mm ²
Count rate	200 kcps
Collection angle	0.7 sr
Energy resolution	≤ 136 eV (Mn-K α and 10 kcps)

In case of EDXS spectrum images this allows the preparation steps such as STEM-HAADF imaging to be done at low beam currents (50-200 pA) until the actual EDXS mapping is started. This helps limiting beam damage and contamination until the beam current is increased for a higher count rate in EDXS. The presented measurements were acquired at a beam current of 1.0 nA (figure 22, figure 23) and 0.8 nA (figure 24) respectively using times between 250 and 1000s.

Dwell time is another critical component in the acquisition of EDXS mappings. In the measurements acquired on the Tecnai F20 each pixel was scanned once for 15-60 seconds. As the beam of the Titan has higher beam current and is also more focused because of the Cs corrector, the Cu₂ZnSnS(e)₄ nanoparticles (and most other specimens) can be severely damaged by the beam. To avoid this, the scanning strategy was changed to quick scanning and accumulating data by scanning the same frame multiple times. A dwell time of 100 μ s was used for a total acquisition time of 250-1000 seconds. STEM-HAADF images for a 250 second measurement at 1.0 nA and a dwell time of 100 μ s are shown in figure 21. There is almost no visible change in the appearance of the nanoparticles after the measurement.

With large acquisition times specimen drift can be problematic. Drift is generally caused by thermal and electrical instabilities of the microscope. In general, the observed drift of the microscope was very low and practically unnoticeable. However, scanning a specimen mounted on a carbon film with a high intensity beam over several hundred seconds leads to sample drift due to heating of the specimen. As consequence images start to blur into the direction of the drift over time. The images in figure 21 show that the sample moved to the left and upwards during acquisition.

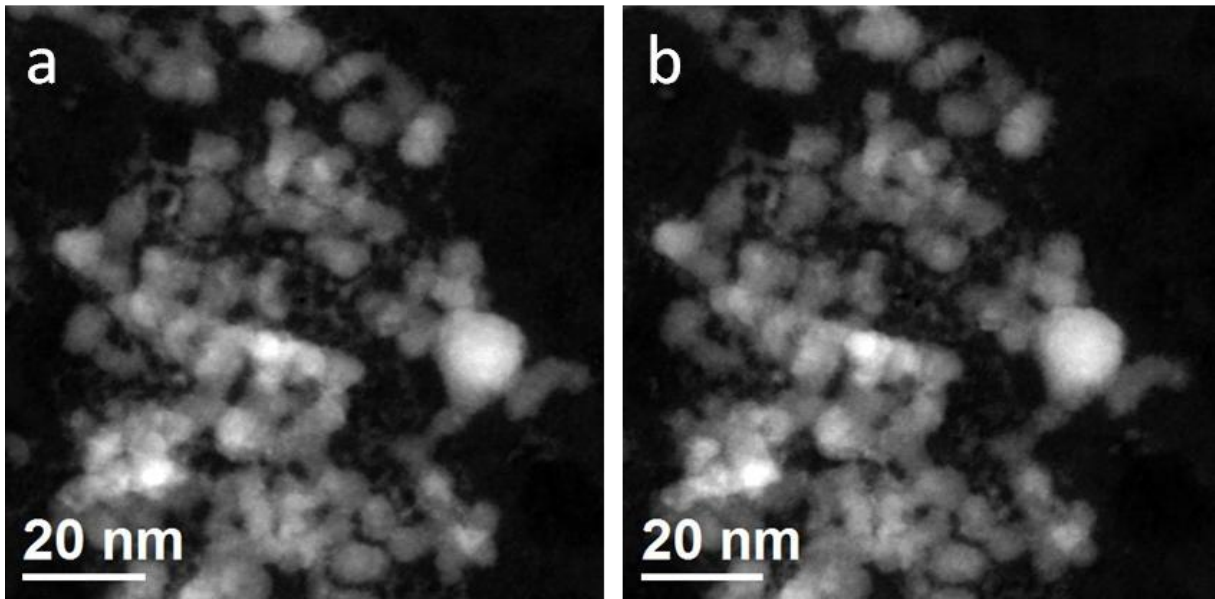


Figure 21: STEM-HAADF image of specimen A-Se-TOPO 2 before (a) and after (b) cumulative scanning for 250 seconds using a beam current of 1.0 nA with a dwell time of 100 μ s.

To compensate drift the drift correction module was activated in Bruker Esprit. It works by cross-correlating specific patterns within the scanned area for each frame and readjusting the scanning region in case drift is detected. Unluckily the drift compensation is not perfect and while it can prolong the acquisition time, blurring still occurs. During acquisition a live image of the total measurement is shown in Esprit. This allows monitoring the progress of the data acquisition. Once the blurring effect of the specimen drift becomes visible the measurement can be stopped.

Elemental maps were extracted from the EDX spectrum images by selecting an energy window for each element in the EDX spectra. For each pixel of the elemental maps the sum of counts within this energy range is represented as intensity. While this method is simple, it has some drawbacks that need to be considered when interpreting these images.

Background correction is missing in this method. Even if an element is absent in an area of the image, some counts will be collected by the EDXS detector. Setting the lower contrast limits of the image to the lowest values measured will usually result in a correct image, but in case the matrix contains a constant, low amount of the element in question this could lead to false interpretations. As the matrix is a carbon film, it can safely be assumed that it consists only of carbon and the lower contrast limit is correct.

Summing up intensities is not a sufficient tool for quantitative analysis. The elemental maps show the distribution of the elements from low to high content in certain areas. However, it is not possible to get quantitative information about the chemical composition using these maps. For this purpose a quantitative analysis (e.g. using the thin film method) could be done. Considering the low count rate of the spectra in the individual pixels, the error margin of the quantification would be too high for reliable results, and was hence not executed.

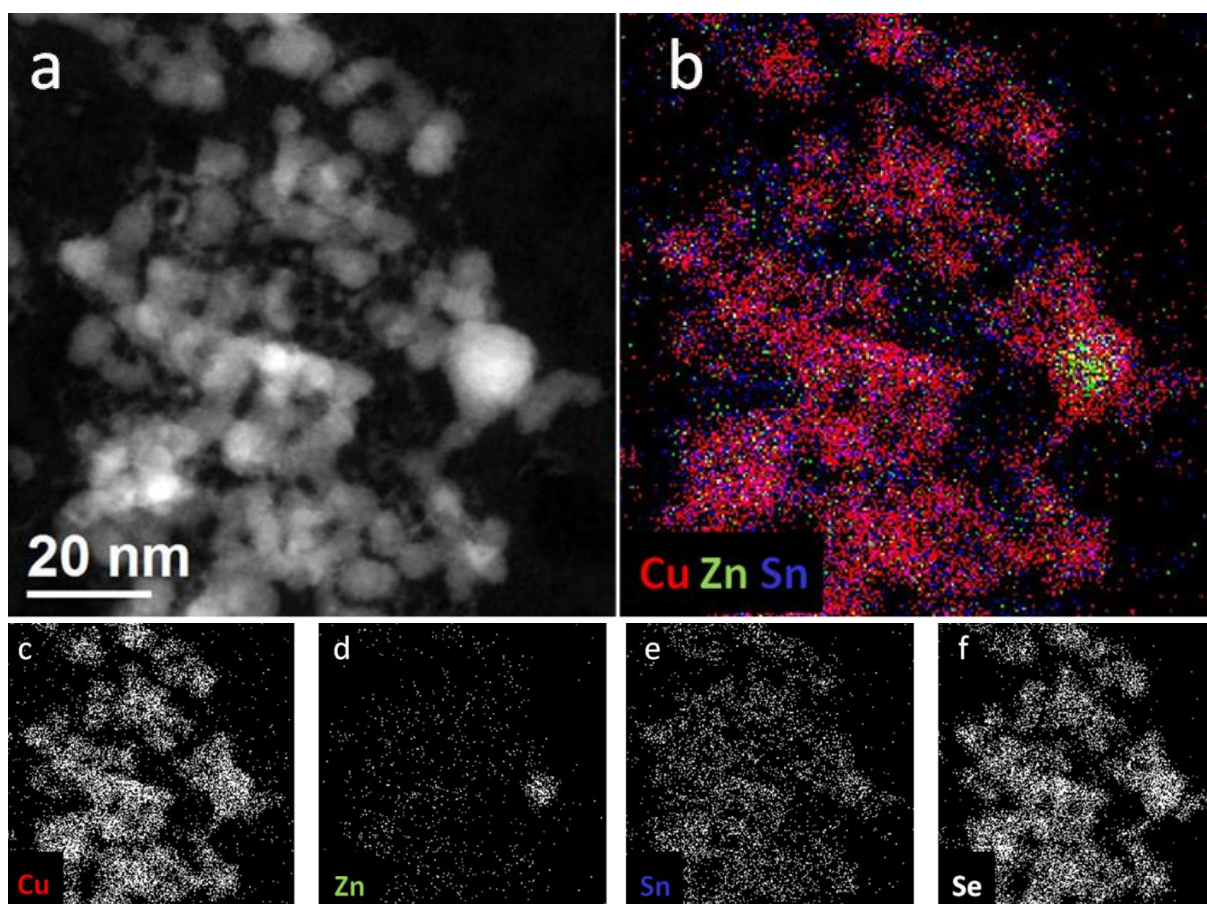


Figure 22: STEM-HAADF image (a), composite image (b) for Cu/Zn/Sn and individual chemical maps (c-f) extracted from EDXS mapping for specimen A-Se-TOPO 2.

Figure 22a shows results including STEM-HAADF (a) and a composite image (b). Maps extracted from the EDXS mapping for individual elements are shown in c-f. Beam current was 1.0 nA with 250 s total acquisition time at 300 kV. The pixel size was 0.38 nm with a field of view of 97 nm (256^2 pixels). The maps for Cu and Se show a good overlap, Sn on the other hand seems to be mostly localized in the areas containing Cu and Se, but the intensity does not increase significantly inside the particles. This may indicate a preferred reaction with Cu, as it was noticed during optimization of the synthesis before. Zn is hardly present at all and seems to be localized in only one nanoparticle, which is larger than all other nanoparticles. The Zn seems to be inside the core of this nanoparticle.

The elemental maps presented in figure 23 show the Zn-rich nanoparticle at higher magnification. Beam current was 1.0 nA with 600 s total acquisition time at 300 kV. The pixel size was 0.19 nm with a field of view of 49 nm (256^2 pixels). The horizontal line in the maps is an artifact caused by a software glitch. Zn is restricted to the inside of the nanoparticle while the outside is made up of Cu and Zn. Again, Cu seems to be more localized and has sharper borders than Sn.

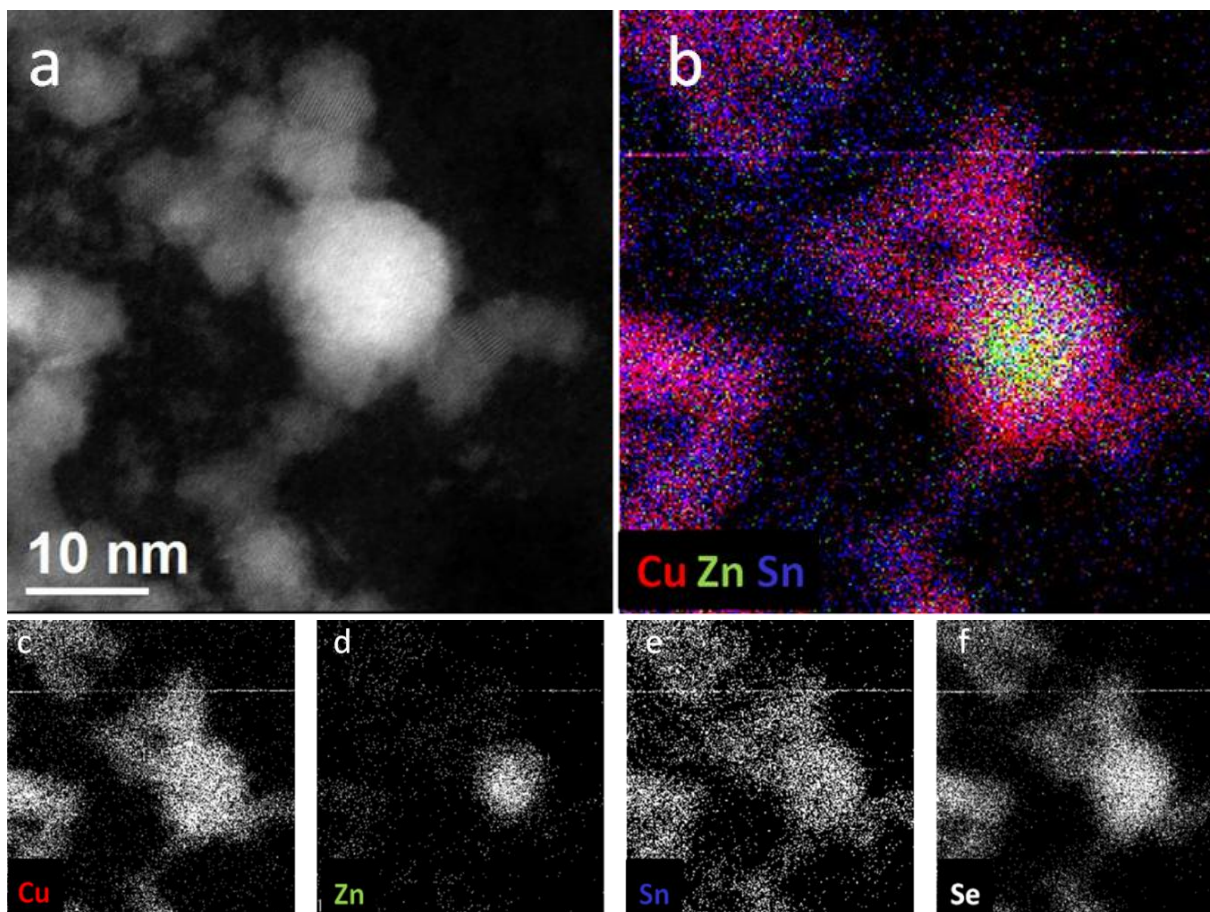


Figure 23: STEM-HAADF image (a), composite image (b) for Cu/Zn/Sn and individual chemical maps (c-f) extracted from EDXS mapping for specimen A-Se-TOPO 2.

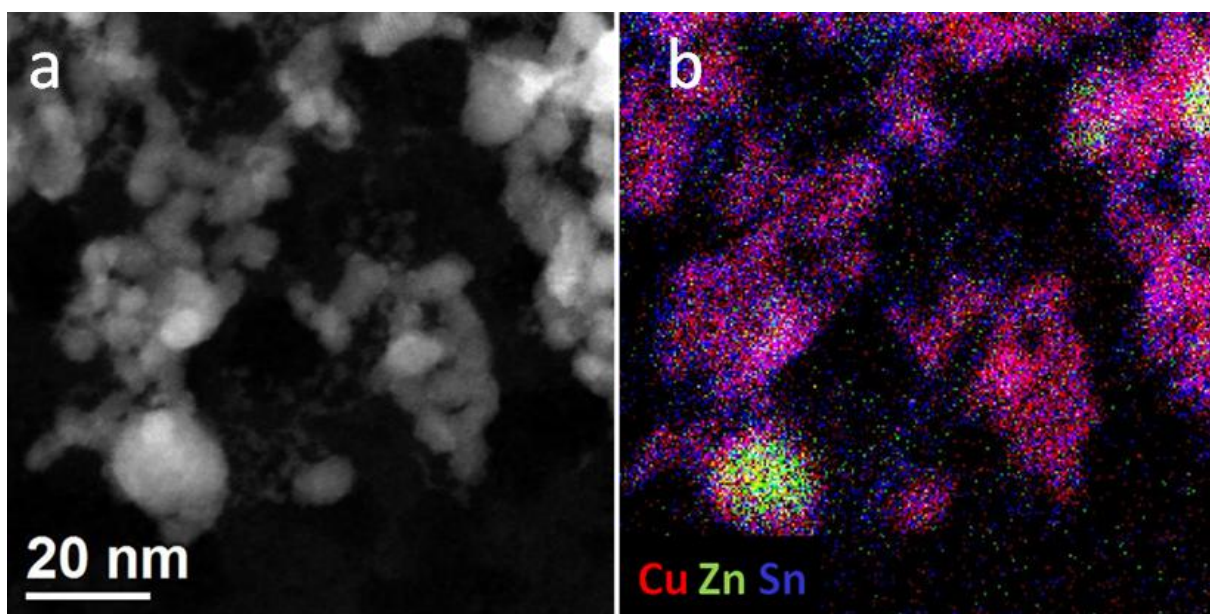


Figure 24: STEM-HAADF image (a), composite image (b) for Cu/Zn/Sn for specimen A-Se-TOPO 2.

Figure 24 shows an additional overview image (taken at 0.8 nA beam current, 1000 s total acquisition time, pixel size was 0.38 nm with a field of view of 97 nm (256² pixels)). Specimen drift is visible in direction from lower left to upper right corner. The large particles contain a Zn core whereas the small ones are made up by Cu and Sn.

This is a highly interesting result and further measurements will be executed to gain a deeper understanding of this issue. The resolution of the images shown with a pixel size of 0.19/0.38 nm is much higher than images acquired previously on the Tecnai F20 and allows a more detailed view of the nanoparticles. Due to the increased resolution, the presence of Zn-rich areas can be attributed to an actual presence of Zn and not local artifacts in a single pixel. However some of the pixels are still black because statistically even during repetitive scanning little or no signals were acquired in them, while surrounding pixels clearly show signals. This issue could be resolved by recording spectrum images with higher acquisition times (currently limited by drift effects) and higher count rates. Recording EDX spectrum images with a higher total count rate would also allow quantification of the spectrum images. To achieve this goal the beam current and the measurement time could be increased. As the beam current of the measurements shown here is already around 1 nA and the acquisition parameters have been optimized to not damage the specimen, further increase should be avoided. Increasing the measurement time could be done by decreasing the specimen drift or using a different drift correction module (e.g. Gatan's Digital Micrograph instead of Bruker Esprit). Electron tomography would allow getting three dimensional data about the nanoparticles. In combination with analytical techniques it would help understanding if the Zn-rich areas are actually embedded inside shell of Cu/Sn-selenide, as some indications in the images suggest.

4.2 Characterization of nanocomposite materials and devices

4.2.1 Introduction

Electron microscopy images give a deeper insight into the nanocomposite layer of a solar cell. However, by simply taking an image it is not possible to understand why one system works and another does not. Morphology has been identified as a crucial factor influencing device performance in the organic PCBM/P3HT system. Over the years many factors have been found to influence the morphology via phase separation and the size of agglomerates. Consequently these factors have high impact on the device performance of organic solar cells, such as solvents used for processing,⁶⁵ compound concentration and ratio⁶⁶ and thermal treatment after formation of the active layer.⁶⁷ When connecting the morphology and device performance, one of the key aspects is the exciton diffusion length. With typical values of 10-15 nm⁶⁷ both phases need to be in contact within this range for efficient charge generation/separation process. Additionally a gradient of donor/acceptor material can help ensuring the percolation pathways are not interrupted as the amount of material needed for transport increases towards the respective electrodes. While certain aspects, such as the need for uninterrupted and short percolation pathways can be applied to hybrid solar cells as well, aspects dealing with the solubility and phase separation of two organic components cannot be applied directly to hybrid solar cells. Most importantly, the inorganic phase is either formed ex or in situ, but in both cases additionally to phase separation between organic and inorganic phase the size and shape of the nanoparticles has to be addressed. Yang et. al found for their CdSe/P3HT system that increasing the size of the nanoparticles had a positive impact on device performance, mostly caused by an increased short circuit current. The largest nanoparticle size investigated was 7 nm, attempts to produce larger nanoparticles were not successful due to agglomeration of the nanoparticles.⁶⁸ Zhou et. al investigated the effect of mixing nanorods and quantum dots in the CdS/PCPDTBT system. A 2:1 ratio of quantum dots:nanorods yielded the highest power conversion efficiency, which was also the maximum of the short circuit current.⁶⁹ In both cases the positive effect on short circuit current and device performance can be attributed to the formation of a higher number of percolation pathways. Due to the presence of a copper in ex situ prepared nanoparticles/nanorods a system using in situ generated nanorods would be ideal for extensive percolation pathways.⁷⁰

Figure 25 shows the I-V curves of an organic solar cell. The black line is measured under dark conditions, the red line under illumination. The following key parameters for describing a solar cell can be extracted:

- The open circuit voltage (V_{OC} , b) is measured when no current is flowing through the device. V_{OC} primarily depends on the energy difference between HOMO of the donor and LUMO of the acceptor and is not influenced by the morphology.
- The short cut current density (J_{SC} , a) includes many factors, such as the efficiency of the current generation process and its transport towards the electrodes. Morphology related effects strongly affect J_{SC} .
- The maximum power point (P_{max}) is defined by the maximum of the product of voltage and current. The shape of the curve can be described by the fill factor (FF), which is defined by

$$FF = \frac{I_{MPP} \cdot V_{MPP}}{J_{SC} \cdot V_{OC}}$$

In practice, a high FF corresponds to a rectangular shape of the I-V curve. The efficiency η of a solar cell is defined by

$$\eta = \frac{V_{OC} \cdot J_{SC} \cdot FF}{P_{IN}} * 100$$

Apart from P_{IN} , the power of the incident light, the three previously discussed factors, V_{OC} , J_{SC} and FF define the performance of the solar cell. An ideal solar cell has high V_{OC} (depends on the materials used) and high J_{SC} and FF (both defined by the morphology).

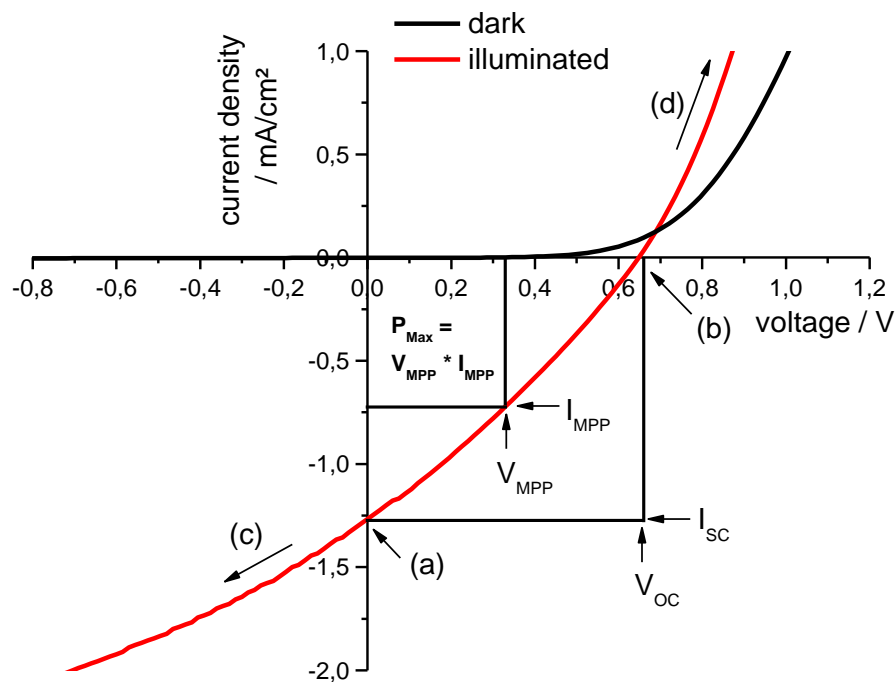


Figure 25: I-V curves of an organic solar cell under illumination (red line) and in dark conditions (black line); PhD thesis Thomas Rath.⁷¹

One of the goals of the CD Laboratory for nanocomposite solar cells was gaining a better understanding of the connection between morphology and device performance. For the PCBM/P3HT system a lot of simulation work exist describing many parameters including variation of the energy levels, domain size, interface to volume ratio, percolation pathways and weight ratio between donor and acceptor.^{72,73} Simulations on the topic of hybrid nanocomposite cells were conducted at the Institute of Theoretical and Computational Physics, TU Graz (Dr. Karin Zojer, DI Benjamin Stickler, Dr. Manfred Gruber). Gruber et al.⁷⁴ defined two scenarios for their simulations: Isolated particles and comb-like structures. The comb-like structure (figure 26a), providing percolation pathways to the electrode, corresponds to an ideal case, in which the distance between the digits would be limiting to the short cut current if the distance between the digits rises above the exciton diffusion length. Additionally the effect of isolated islands (figure 26b) was investigated in simulations. Their presence decreases the overall efficiency. Pathways to the electrode on the other hand increase the short cut current. A large contact area between the phases is advantageous for the form of the I-V-curve, a small contact area results in s-shaped I-V-curves. In practice, systems are usually a superposition of comb like structures and isolated islands (figure 26c). These results are in good agreement with both theoretical and practical observations that have been reported previously.

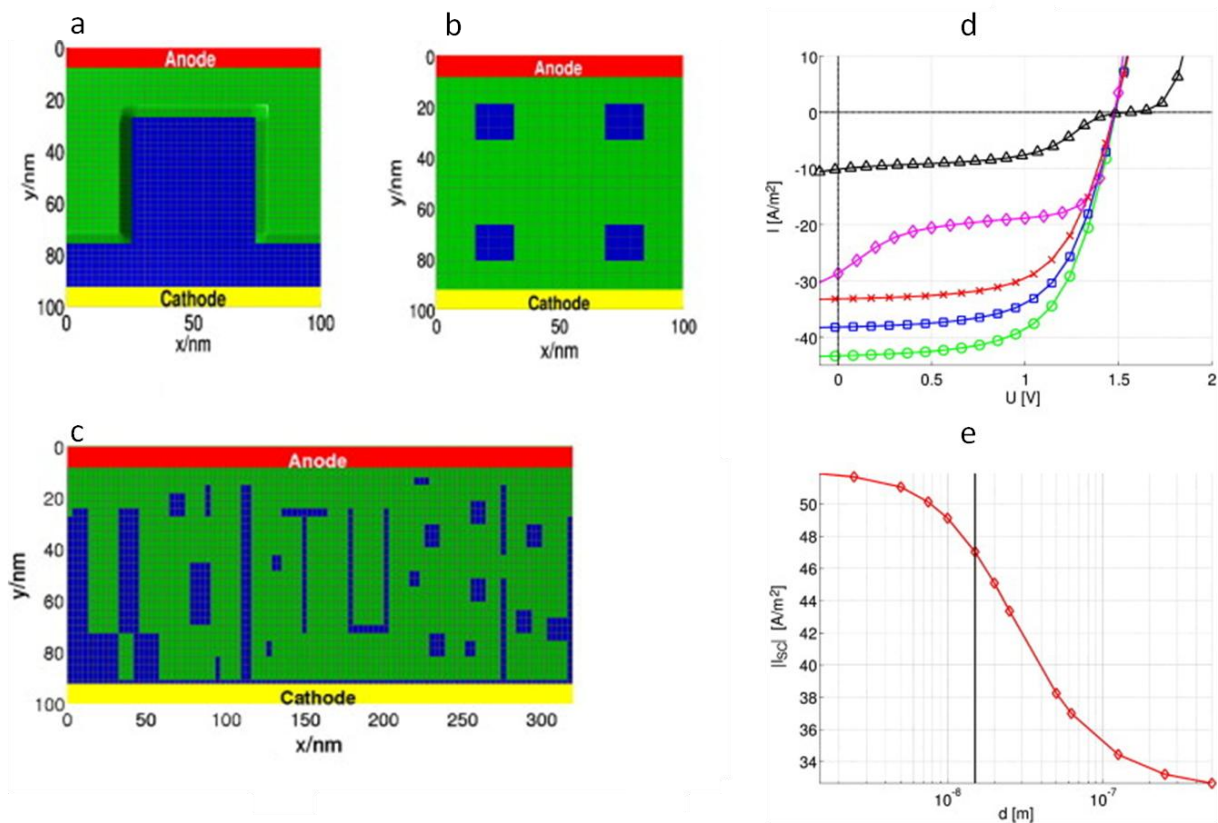


Figure 26: Morphologies for interface: comb-like structure (a), isolated nanoparticles (b), superposition of both structures (c); I-V curves for the P3EBT/CuInS₂ interdigitated interface with finger width $d=250$ nm (crosses, \times), 50 nm (squares, \square), and 25 nm (circles, \circ), nanoparticles (triangles, \triangle), and real structure (diamonds, \diamond) in a device with ohmic contacts. (d); Dependence of the short circuit current density J_{sc} on finger width d for the interdigitated device with ohmic contacts. The exciton mean free path length of 15 nm is indicated by a vertical line. (Results from master's thesis M. Gruber⁷⁵ and Gruber, M.; Stickler, B.a.; Trimmel, G.; Schürer, F.; Zojer, K.; Impact of energy alignment and morphology on the efficiency in inorganic–organic hybrid solar cells; *Organic Electronics* **2010**, *11*, 1999–2011.⁷⁴)

4.2.2 Requirements

In general, TEM samples need to be thin (<100-200 nm) and transparent for electrons. As a TEM specimen is limited in size to 3 mm and FIB lamellae are usually only a few micrometer in size it is vital to have both a representative specimen, but sometimes also one that shows a specific defect of a device. Additionally the specimen should be able to withstand the preparation both mechanically and chemically without being altered. It is essential to keep all these points in mind when preparing TEM specimens.

4.2.3 State of the art for TEM investigations

A lot of effort was put into the study of organic/organic solar cell systems, most of all the very popular PCBM/Poly(3-hexylthiophen-2,5-diyl) (P3HT) system or variations using different polymers or fullerene derivatives. Xiaoniu Yang and Joachim Loos gave a good overview over literature in their review in 2009.⁷⁶ The morphology of the active layer is identified as crucial part in the investigations and imaged in both 2D and 3D.⁷⁷ While nanoparticles had been studied for years as well as inorganic solar cell materials at the beginning of this work, no literature could be found about the study of

organic/inorganic nanocomposite solar cells. Over the years other groups released details about their TEM investigations of organic/inorganic nanocomposites, such as ZnO/P3HT⁷⁸ or CdS/P3HT.⁷⁹ Hence, the methods described for specimen preparation and investigation of the PCBM/P3HT system were used as a starting point and adapted for nanocomposite solar cells in this work.

4.2.4 Methods for specimen preparation

In principle, two methods are available to analyze a nanocomposite solar cell: Top-down and cross-sections. The unique advantages and disadvantages will be discussed below.

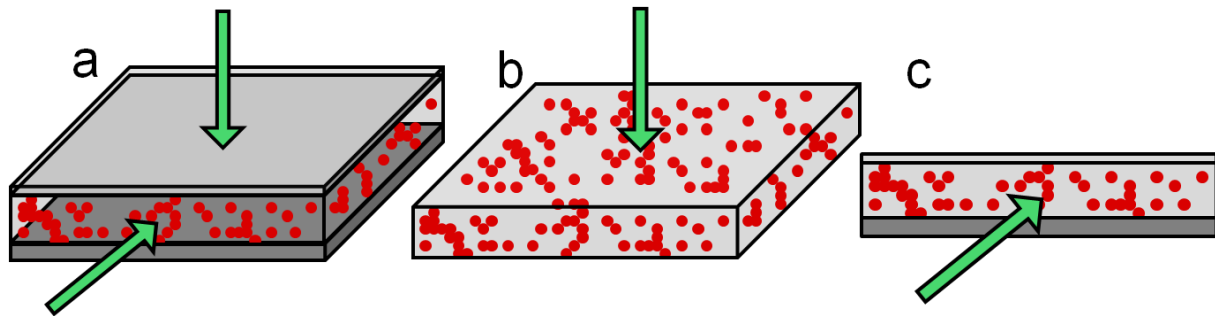


Figure 27: a) Methods for investigation of nanocomposite solar cells: top-down and cross-section approach; b) top-down of thin film; c) cross-section.

4.2.4.1 Top-down preparation

Figure 27a shows a schematic of a solar cell consisting of multiple layers (electrodes below and above the active nanocomposite layer). Using a top-down approach as shown in figure 27a is only of limited use, as the electron beam has to pass through all layers. Even if the sample would still be electron transparent, the information from all layers would overlay and no useful image information would be generated. Hence the approach shown in figure 27b was used by creating a specimen consisting only of the active layer. In literature, one of the popular approaches for PCBM/P3HT is by floating off the active layer. Usually, a layer of PEDOT:PSS is coated as a first step. The active layer is added on top of it, dried and the specimen placed in deionized water. PEDOT:PSS dissolves and the active layer floats off to the water surface and is collected using a TEM grid.⁸⁰ Due to the thermal treatment of the nanocomposite solar cells with temperatures up to 180-200°C PEDOT:PSS was not useable in this case, as its solubility was strongly decreased during the process. As a consequence PEDOT:PSS was substituted by single NaCl crystals. Due to high concentration of NaCl in the water after floating off, films had to be washed thoroughly (transfer to a vessel with fresh deionized water for 5 times) and were subsequently transferred to TEM grids. Figure 28 shows nanocomposite films mounted on TEM grids.

As the process does not involve any cutting or milling steps, no artifacts are introduced hereby. Specimens are stable over months and no special, expensive equipment is needed. The active layer of the solar cell can be studied in detail as no other layers are present.

It is however important to keep in mind that water soluble components inside the film can be removed. Additionally coating on top of the surface of NaCl can lead to different wetting behavior than on ITO or PEDOT:PSS. Since it is a top-down view, no interfaces or other layers can be observed.

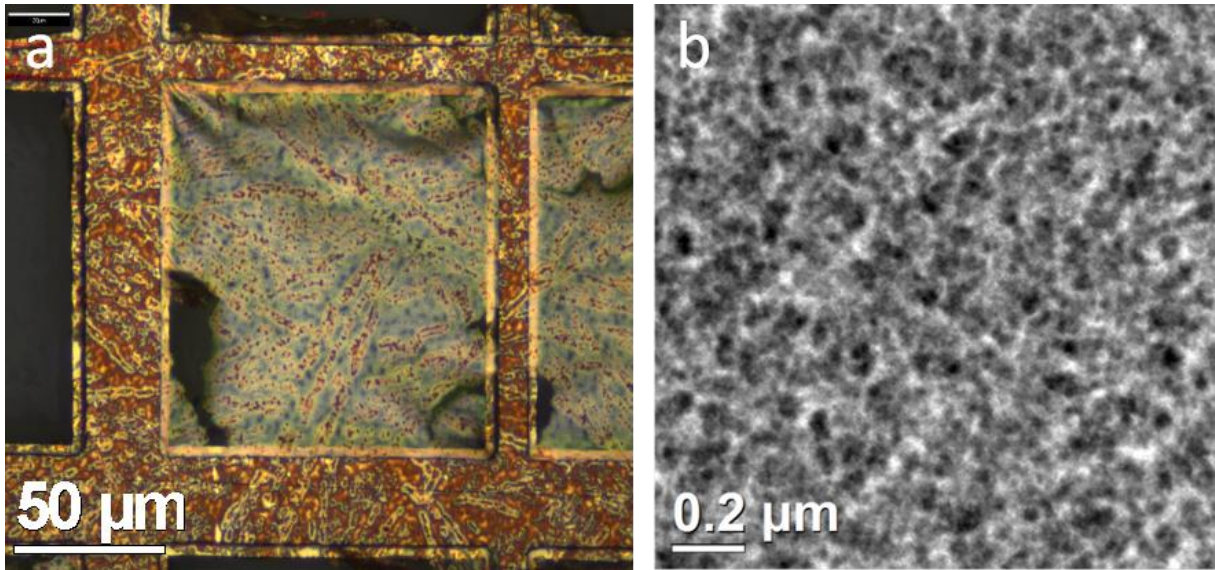


Figure 28: Optical microscope image of nanocomposite film mounted on TEM grids (a); TEM-BF of nanocomposite solar cell (top-view, b).

4.2.4.2 Cross sections using ultramicrotomy

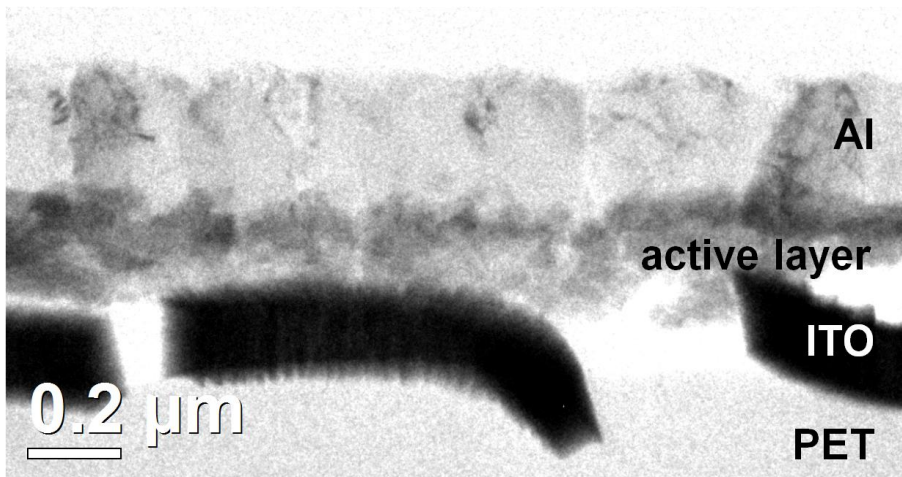


Figure 29: TEM-BF of ultramicrotomy cut of a device on PET-ITO.

Ultramicrotomy allows the preparation of cross sections from soft materials. Several attempts were made to cut nanocomposite solar cells on PET-ITO (as glass-ITO is too rigid and would damage the knife). However, due to the different hardness of the individual layers breaking of the ITO layer and delamination occur. Figure 29 shows the best of all results, in which no complete delamination occurs. The ITO layer is broken and the nanocomposite layer is falling apart. As this method did not prove to produce reliable results, it was abandoned.

4.2.4.3 Cross sections using FIB

Differently to top-down preparation cross-sections can be made from an actual solar cell device instead of preparing a film solely for TEM investigations. This allows connecting the properties from electrical characterization with the results from TEM. Furthermore all layers of the device can be investigated. Of course, these advantages come literally at a price – specimen preparation of cross sections is more complicated and requires more sophisticated equipment such as the Focus Ion

Beam Microscope (FIB). Additionally the area of investigation is limited to a few micrometers by the size of the cross section. It is important to cut out the right part of the device, either a representative region, a defect, or both.

The FIB itself is a unique tool beyond a method for simply creating TEM specimens. Functioning as a SEM it allows the characterization of samples, which enables to find exactly the spot from which a lamella should be taken. However, exposure to the electron and ion beam of the FIB can cause severe damage to specimen,⁴⁸ especially degradation of polymers.⁸¹ Amorphization of crystalline materials is also a well known issue and can be minimized by using the right milling conditions.⁸² Previous experiments on organic materials (OLED, OFET) using the institute's FIB were positive,^{21,83} there have also been successful FIB cuts of organic/organic (PCBM/MDMO-PPV)⁸⁴ and inorganic/organic (ZnO/P3HT)⁷⁸ solar cells in literature.

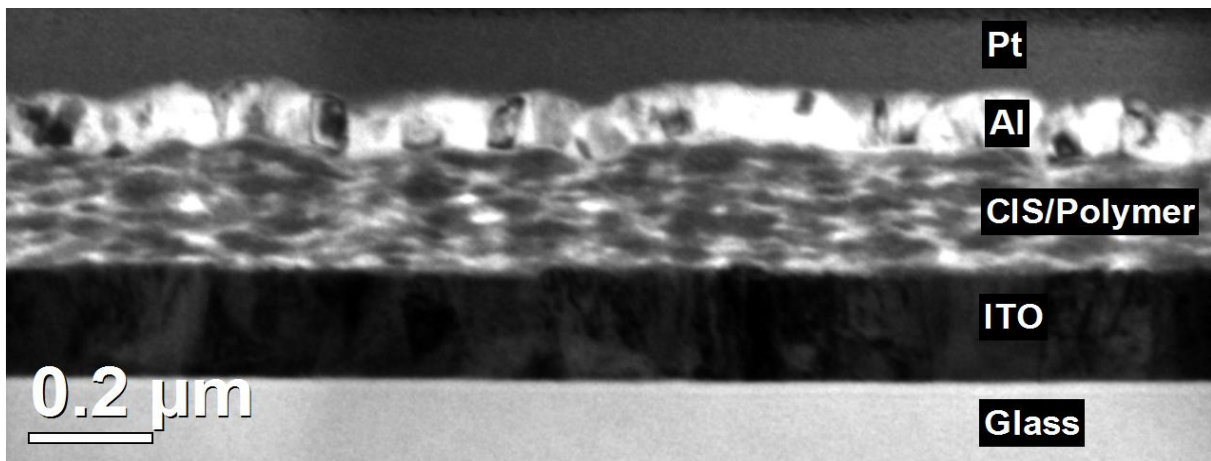


Figure 30: TEM-BF of layer structure in FIB cut of a device based on CIS/MDMO-PPV.

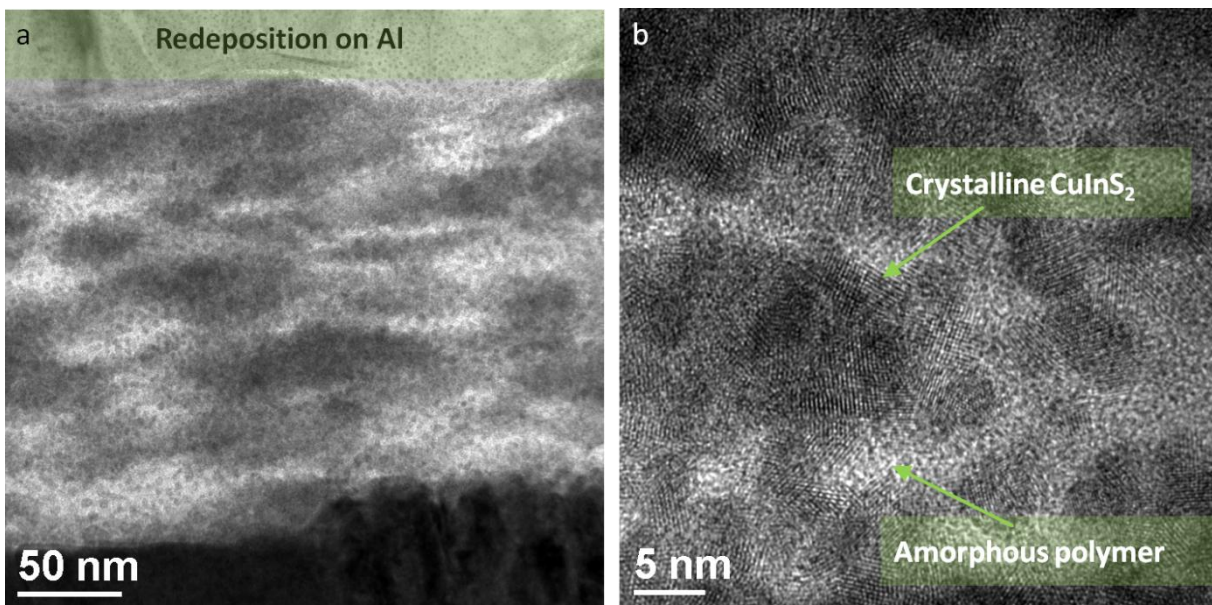


Figure 31: Investigation of FIB cut shown in figure 30; Redeposition is visible on the Al layer (a); both crystalline CuInS_2 and amorphous polymer are visible in the active layer (b).

Figure 30 shows a TEM-BF image of a FIB lamella. The individual layers can be identified. Figure 31a shows the active layer. On top of the image, redeposition can be seen on the Al layer. Figure 31b

shows a HRTEM image of the active layer. Lattice fringes from the crystalline CuInS_2 are visible, the amorphous lighter parts are attributed to the polymer. While polymers tend to be damaged quickly by processing in the FIB,⁸¹ lattice fringes are still visible from the nanoparticles – no amorphization occurred. Quantification of the Ga content was below 1 at%.

Figure 32 shows a comparison of cross-section and top-down view. In both cases a cloud like structure of the CuInS_2 agglomerates within the polymer is visible. Structures are comparable in size, but in case of the cross-section elongation in xy-direction is visible. The formation of the nanocomposite layer is accompanied by a mass loss due to evaporation of remaining solvent and the volatile byproducts of the thermal decomposition of the precursor. While initially an isotropic distribution of the nanoparticles can be assumed, due to the mass loss shrinking in z-direction occurs and causes the elongation of the agglomerates in xy-direction.

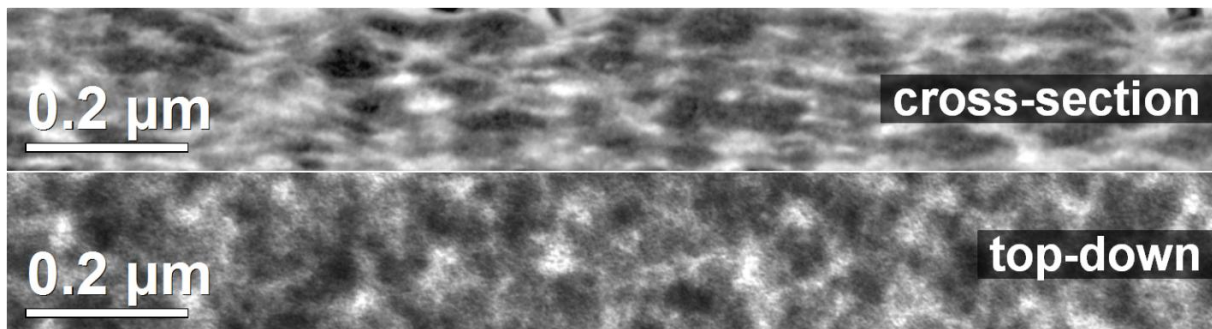


Figure 32: Comparison of active layer in cross-section and top-down view for CIS/MDMO-PPV.

4.2.4.4 Cross sections using the Gatan Ilion+

The Gatan Ilion+ (model 693) allows the preparation of planar cross sections for SEM. Samples are mounted on a sample blade and polished using an ion beam (Argon) from two separate ion guns. A cooling stage helps minimizing the beam damage during the milling process.

The sample (solar cell on glass-ITO) was cut down to a 5 x 5 mm piece and attached piggy-back to the sample blade using conductive silver. A Gatan Ilion+ (model 693) was used for preparation of a planar cross section at 3.5 kV at -150°C . Both ion guns were at an angle of 0° .

The combination of the Ilion+ with SEM is a powerful addition to FIB/TEM. Figure 33 shows a comparison between specimens from the same solar cell prepared via both routes. In both cases the detector (BSE for SEM, HAADF for TEM) yields a Z-contrast image. While resolution is better in STEM-HAADF, the layers within the specimen can even be identified using SEM. Obviously FIB/TEM can be used for further analyses that are not possible in SEM because of the limited resolution, but the preparation using Ilion+/SEM is a useful addition in cases where only imaging of the layer structure is necessary as it allows to use less complex and expensive instrumentation.

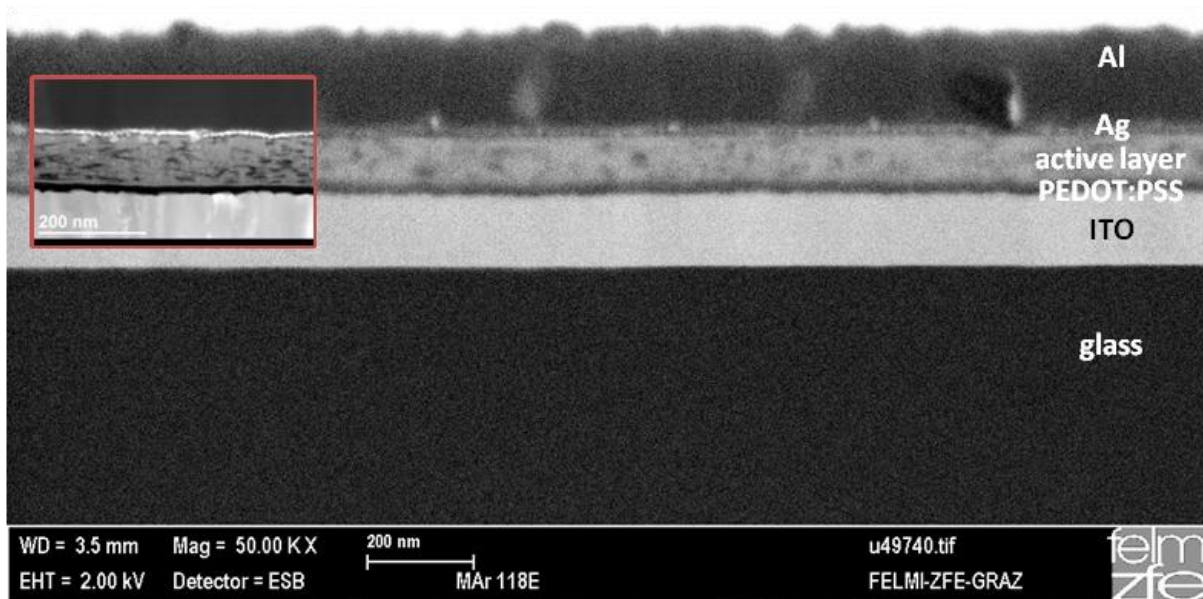


Figure 33: SEM-BSE image of a SEM sample of a device using CIS/PSiF-DBT with an Ag/Al electrode prepared using the Ilion+ and STEM-HAADF image of a TEM specimen prepared using the FIB (inset).

4.2.4.5 Comparison of preparation methods

Each of the methods investigated has its unique advantages and disadvantages. Thin films prepared on single NaCl crystals are a high throughput and inexpensive method for the preparation of specimens for top down investigation. This type of specimen preparation is ideal for the comparison of specimens from different systems or systems where parameters have been systematically changed.

However, thin film specimens miss the other layers of a device, which can only be investigated in cross sections from real devices. FIB processing enables access to these types of investigations. The milling conditions have to be chosen carefully to avoid amorphization of the crystalline materials and delamination of the layers. Additionally the Ilion+ is a less instrumentally complex alternative for polishing cross sections destined for SEM investigations.

In summary both the methods of investigation (top-down vs. cross-section) as well as the preparation methods (low-tech thin films vs. high-tech FIB processing) complement each other well and were both used depending which method was necessary to understand the scientific goals.

4.3 Formation of CuInS_2

The active layer of nanocomposite solar cells is composed of a mixture of semiconducting inorganic nanoparticles and a semiconducting polymer. In principle, there are two routes towards this goal: synthesis of nanoparticles and mixing them into the polymer, and *in situ* formation inside the polymer.

4.3.1 CuInS_2 from synthesis

Similar to $\text{Cu}_2\text{ZnSnS(e)}_4$ nanoparticles CuInS_2 nanoparticles can also be synthesized using the synthesis route described by Hyeon et al.^{24,25}

CuI and InCl_3 are dissolved in oleylamine (170°C, 30 min). After cooling down to room temperature sulfur is added in oleylamine and the reaction is heated again (minutes to hours, depending on desired outcome). The solution is cooled down to room temperature and precipitated using methanol, nanoparticles are washed and dried. Further details are described elsewhere.⁸⁵

Figure 34 shows CIS nanoparticles prepared via conventional synthesis at 220°C for 15 minutes. The nanoparticles are in the range of 7-13 nm; XRD and SAED (not shown) match the JCPDS reference for CIS (JCPDS #42127).

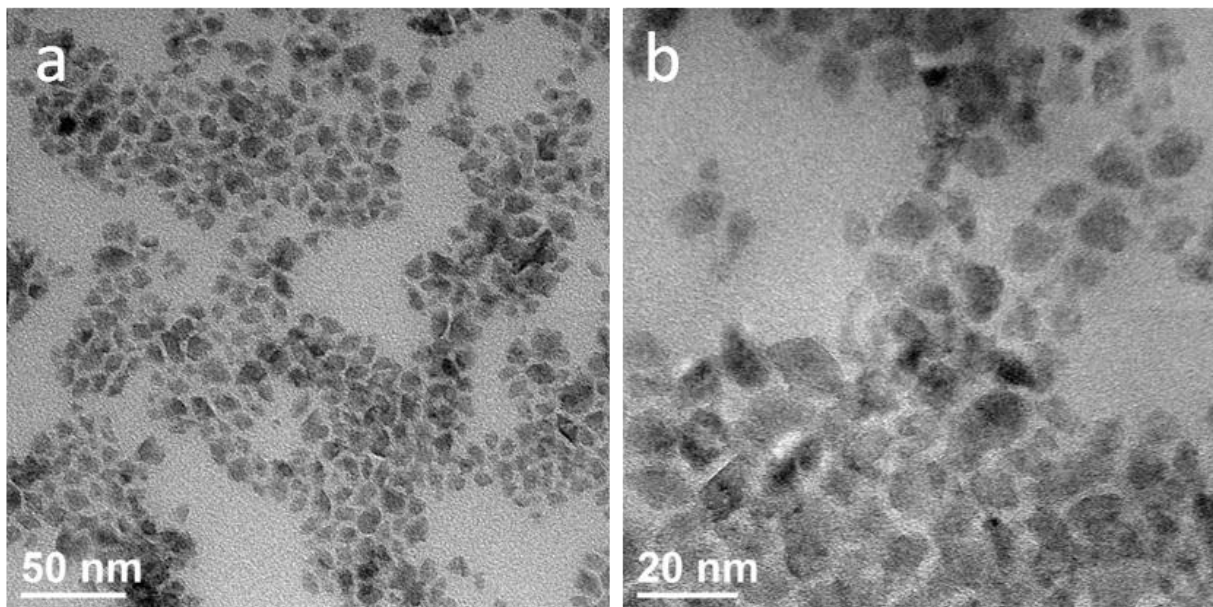


Figure 34: TEM-BF for CIS nanoparticles from conventional synthesis.

An essential part of classical synthesis is the addition of a capping agent (e.g. olyelamine) to avoid agglomeration of the nanoparticles. However the capper also acts as an insulator and by reducing the conductivity of the resulting solar cell the performance is also decreased. This can be overcome by using the capper-free *in situ* method.

4.3.2 *In situ* method

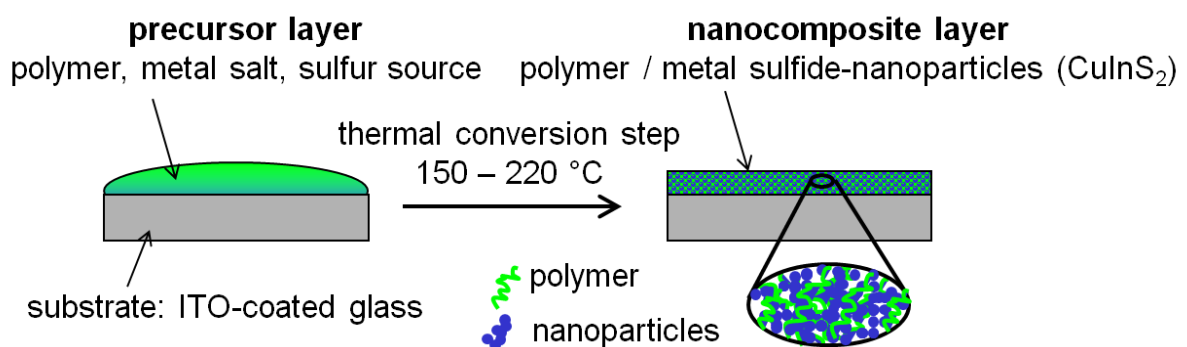


Figure 35: Schematic of *in situ* formation of CuInS_2 ; image by T. Rath.

Instead of intermixing already synthesized nanoparticles they are formed inside the polymer from a precursor. Figure 35 shows the principle of the *in situ* formation process of CuInS_2 . In the first step, a precursor solution is coated on the anode made of ITO-coated glass. The precursor solution contains the polymer (e.g. P3EBT), metal salts (e.g. CuI and InCl_3) and a sulfur source (e.g. thioacetamide). Figure 5 (see page 9) gives an overview about polymers, metal salts and sulfur sources used primarily in this work. In a thermal conversion step, usually inside a tube furnace (Heraeus 4/25), the precursors react forming CuInS_2 and volatile components. For the formation of the inorganic phase,

usually high temperatures up to 400°C are used. In an investigation of CuInS₂ formed from CuAc, InCl₃, and thiourea, chlorine was still found when a conversion temperature of 200°C was used, most likely from not fully removed decomposition products. Samples prepared at 300 or 400°C did not show this impurity.⁸⁶ However, the polymers used in this work are not stable at these temperatures, hence temperatures as high as possible, but as low as needed to not destroy the polymers were used – in practice between 150-220°C.

As mentioned before, the size and distribution of nanoparticles is a key factor for good solar cell performance. Examples for the distribution of nanoparticles and the respective device performance will be shown in chapter 4.4.

4.3.3 *In situ* formation of CuInS₂ inside the ESEM

To gain a deeper understanding about the formation of CuInS₂ the formation process was investigated in an ESEM. Figure 36a & b show the measurement set-up used in these investigations. A glass-ITO plate coated with the xanthate precursors Cu(S₂OC₇H₁₃) and In(S₂OC₇H₁₃)₃ in F8T2 was mounted on a gold-coated heating stage. The stage was heated using an ITC502 temperature controller (Gatan), the temperature was measured using a Pt100 temperature sensor. Contamination on the SSD detector (color fringes) which was located closely above the sample and exposed to the volatile components can be seen in figure 36c.

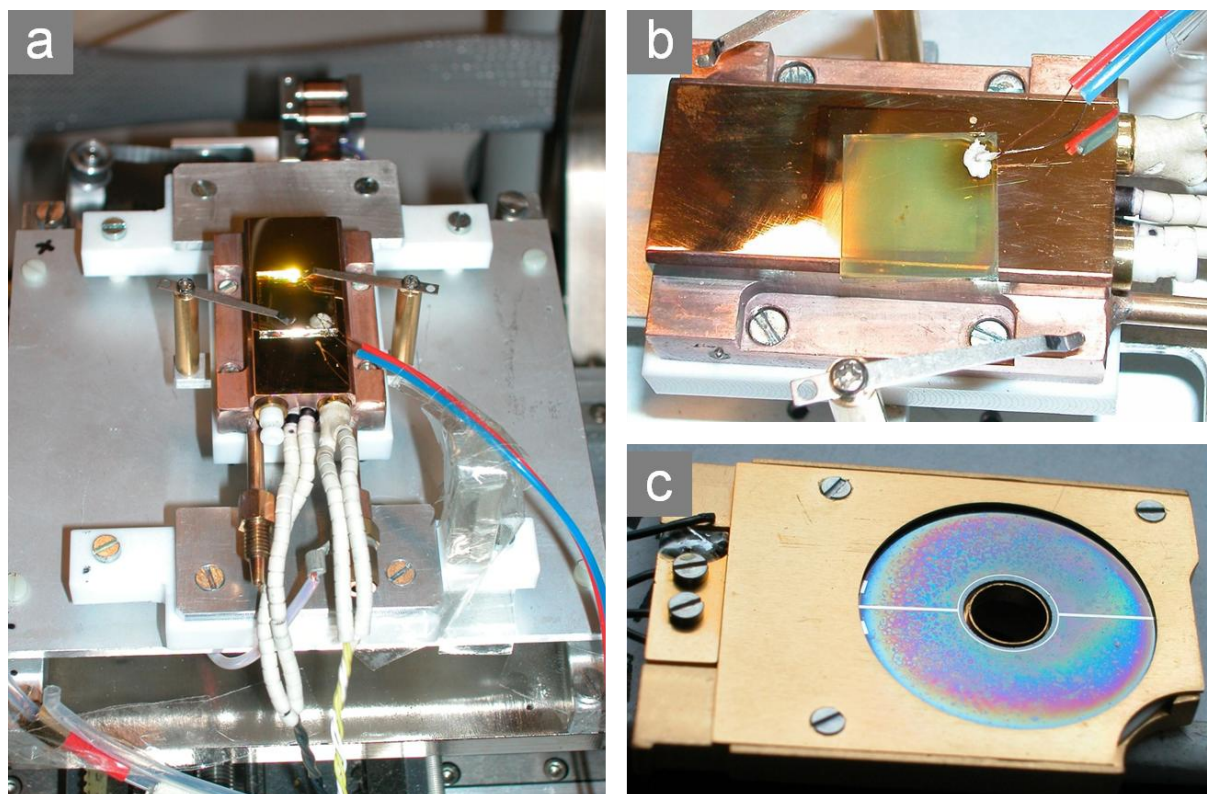


Figure 36: Measurement set-up inside the FEI Quanta 600 (a), gold-coated heating stage with specimen and Pt100 temperature sensor attached (b), contamination on the SSD detector (c).

For each temperature images were acquired at 4000x and 15000x magnification (corresponding to a field of view of 34.0 and 9.0 μm respectively) in both SE and BSE mode. Once the images had been taken, the temperature was increased to the next step and held for approximately 2-3 minutes for image acquisition. Initially the measurements were made in the same spot to ensure reproducibility by looking at the same area, as shown in figure 37 and figure 38. In general, these images show only

low contrast in both SE and BSE mode and could correspond to the non-reacted sample after coating. However, this seems not to be the case as in figure 39, which was taken at lower magnification at 86°C, a huge difference between the central region and the outer regions can be noticed. The central region is the area, which had been scanned in the previous images and appears to be completely flat in the SE image (figure 39a). The backscatter image (figure 39b) shows this region to be much brighter. It can be assumed, that this is a special case of beam damage: The energy of the electron beam catalyzed the xanthate precursor to decompose before its decomposition temperature was reached. Subsequently CuInS_2 was formed while the volatile byproducts were evaporated, leaving behind a CIS/F8T2 layer with higher average Z. As a consequence, all following images were recorded on regions that were not exposed to the electron beam before. At 86 and 104°C (figure 40 and figure 41) a regular structure can be observed in both SE and BSE images. The contrast starts to disappear at 119°C (figure 42) and is gone at 135°C (figure 43). Additionally the area already converted by the electron beam at 86°C and below was no longer recognizable, which is a good indication that the same conversion had happened because of heating to the rest of the sample as well.

TGA measurements of pure xanthate precursors and precursors mixed into polymers show a decrease of the onset decomposition temperature to a range of approximately 100°C.³⁰ This is in good accordance with the results observed here. To make sure that the observed effects were not related to changes in the polymer, a sample consisting only of F8T2 was heated to 200°C. No visible change was noticed during the whole heating process, figure 44 shows the sample at 100°C.

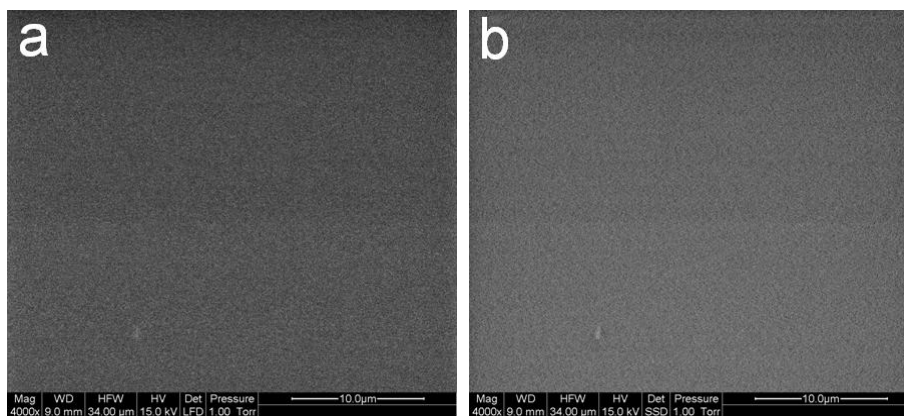


Figure 37: CIS/F8T2 ESEM-heating experiment; 25°C; SE at 4000x (a), BSE at 4000x (b).

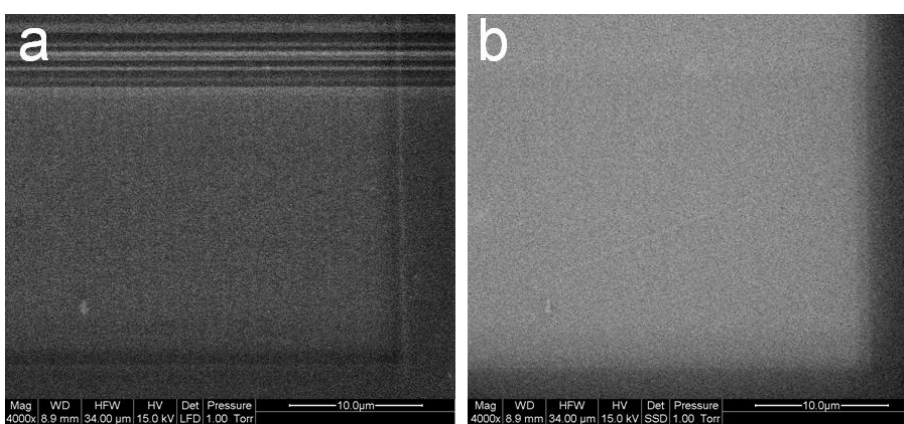


Figure 38: CIS/F8T2 ESEM-heating experiment; 69°C; SE at 4000x (a), BSE at 4000x (b).

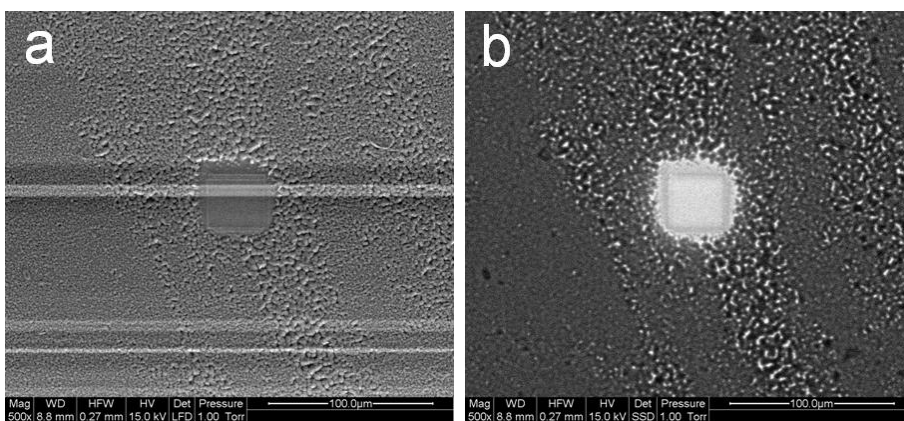


Figure 39: CIS/F8T2 ESEM-heating experiment; 86°C; SE at 500x (a), BSE at 500x (b).

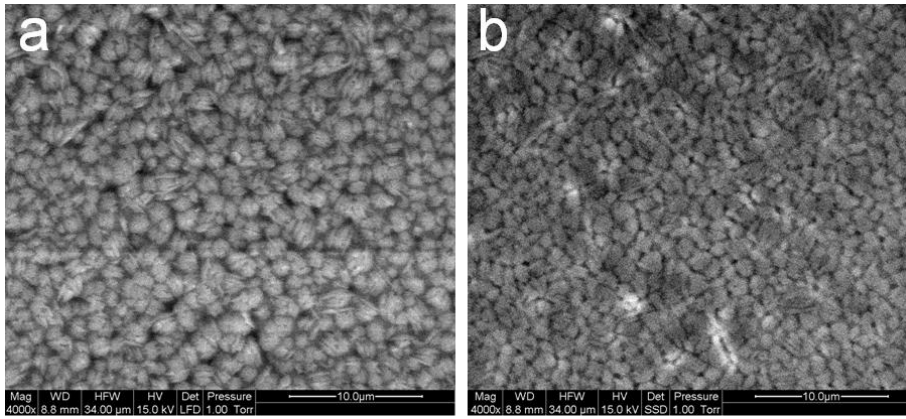


Figure 40: CIS/F8T2 ESEM-heating experiment; 86°C; SE at 4000x (a), BSE at 4000x (b).

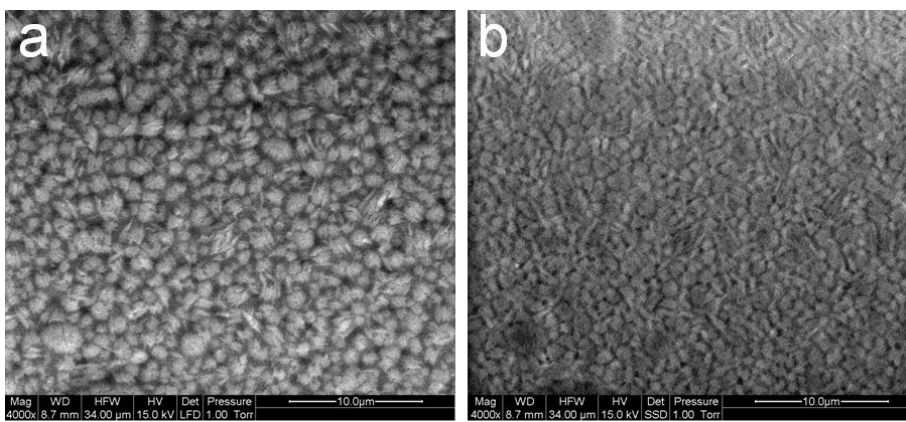


Figure 41: CIS/F8T2 ESEM-heating experiment; 104°C (decomposition temperature); SE at 4000x (a), BSE at 4000x (b).

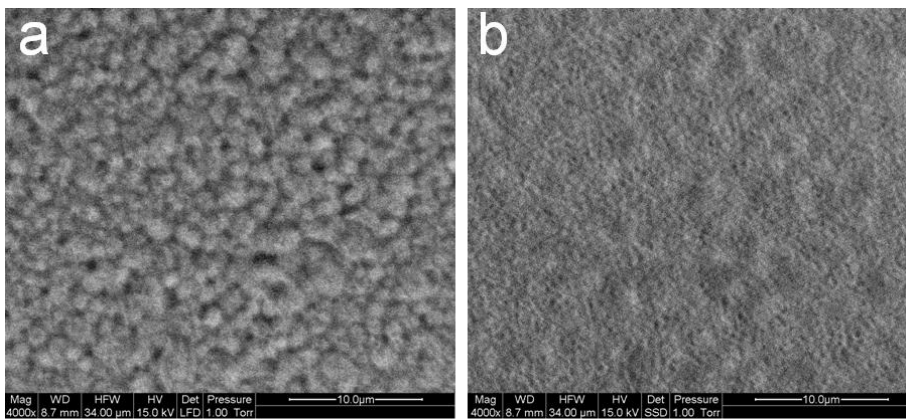


Figure 42: CIS/F8T2 ESEM-heating experiment; 119°C; SE at 4000x (a), BSE at 4000x (b).

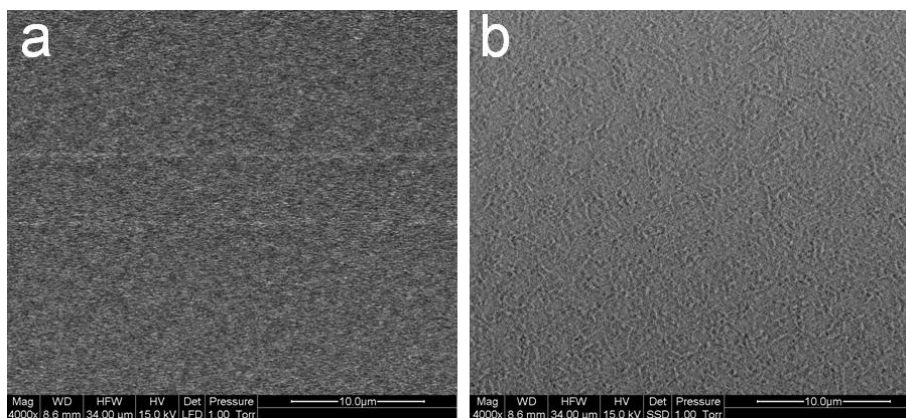


Figure 43: CIS/F8T2 ESEM-heating experiment; 135°C; SE at 4000x (a), BSE at 4000x (b).

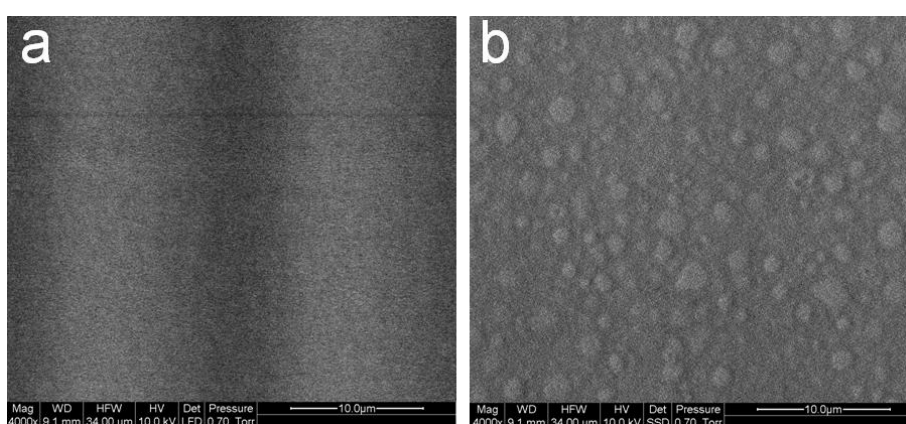


Figure 44: CIS/F8T2 ESEM-heating experiment; Reference sample (F8T2 only) at 100°C; SE at 4000x (a), BSE at 4000x (b).

In a similar experiment using synchrotron radiation for a Grazing Incidence Wide Angle X-ray Scattering (GIWAXS) analysis, the xanthate precursor was heated up in a PSiF-DBT matrix. The GIWAXS pattern (see figure 45) shows the emerging reflex at 28° (corresponding to the (1 1 2) reflex of CIS) at 160°C . This value is approximately 20°C higher than the results in the ESEM show, however the GIWAXS analysis observes the actual crystal lattice formation whereas the ESEM experiment notices the change in morphology. Considering both experiments find the decomposition in approximately in the same range of $140 - 160^\circ\text{C}$ it makes sense to use a higher temperature (200°C) for the formation process to evaporate byproducts and make sure the conversion process is complete.

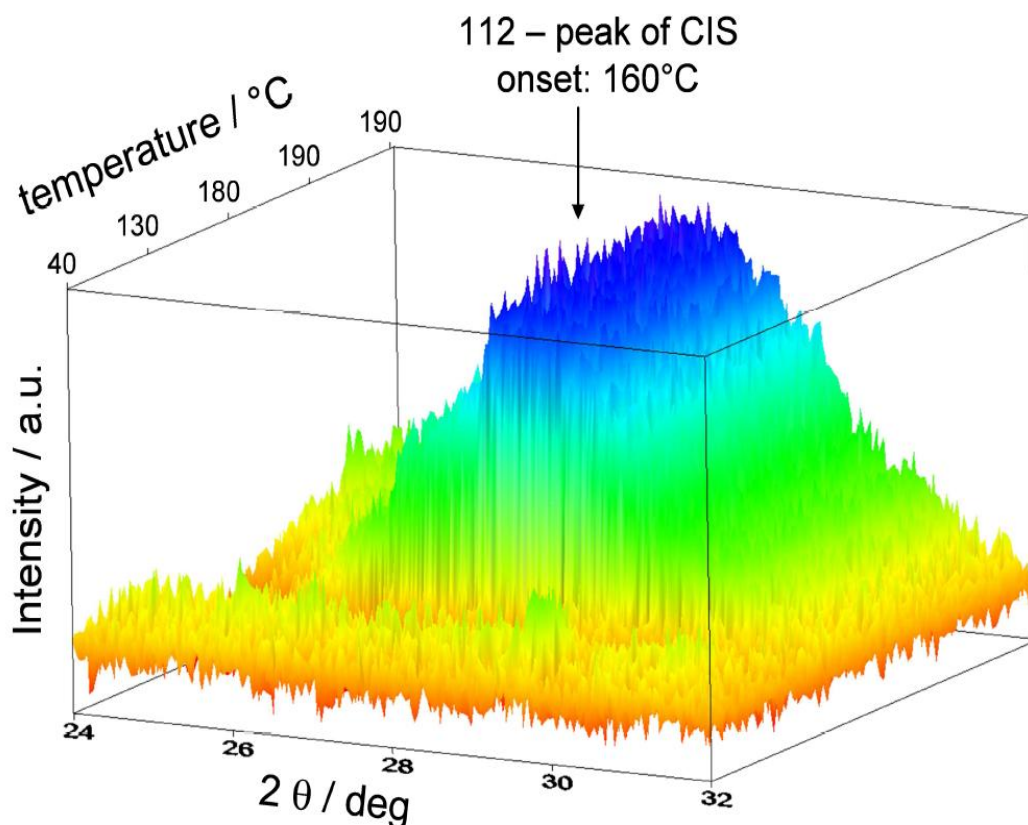


Figure 45: GIWAXS analysis of the formation of CIS from xanthate precursor in PSiF-DBT. (Results from PhD thesis Michael Edler³¹)

4.3.4 *In situ* transformation in TEM

Thermal annealing yields nanoparticles, but as it was observed in ESEM, the high energy of the electron beam can do the same. The reaction was observed by preparing a thin film TEM specimen for top-down analysis on a specimen (Xanthate/MDMO-PPV) which had not yet been thermally annealed. The specimen was placed in a Tecnai 12 microscope operated at 120kV. As soon as the specimen was exposed to the electron beam, a change in contrast could be observed. To decrease the intensity of the beam, conditions were chosen to illuminate a wide area. Observation of the reaction was done in SAED mode at a camera length of 1350 mm with spot size 1, C2=50%, C2=200 μm, emission = 1,5 μA. Images were taken every 5 seconds with an exposure time of 0.25s.

Figure 46 shows the evolution of the SAED pattern for CuInS_2 over a time of 400s. While no rings are visible in the SAED image (figure 46a, black line in c), a ring shaped pattern matching the reference data (JCPDS #42127) for CuInS_2 (figure 46b, red line in c) emerges over a time of 400s. The peaks are very wide though, most likely due to low crystallinity of the nanoparticles.

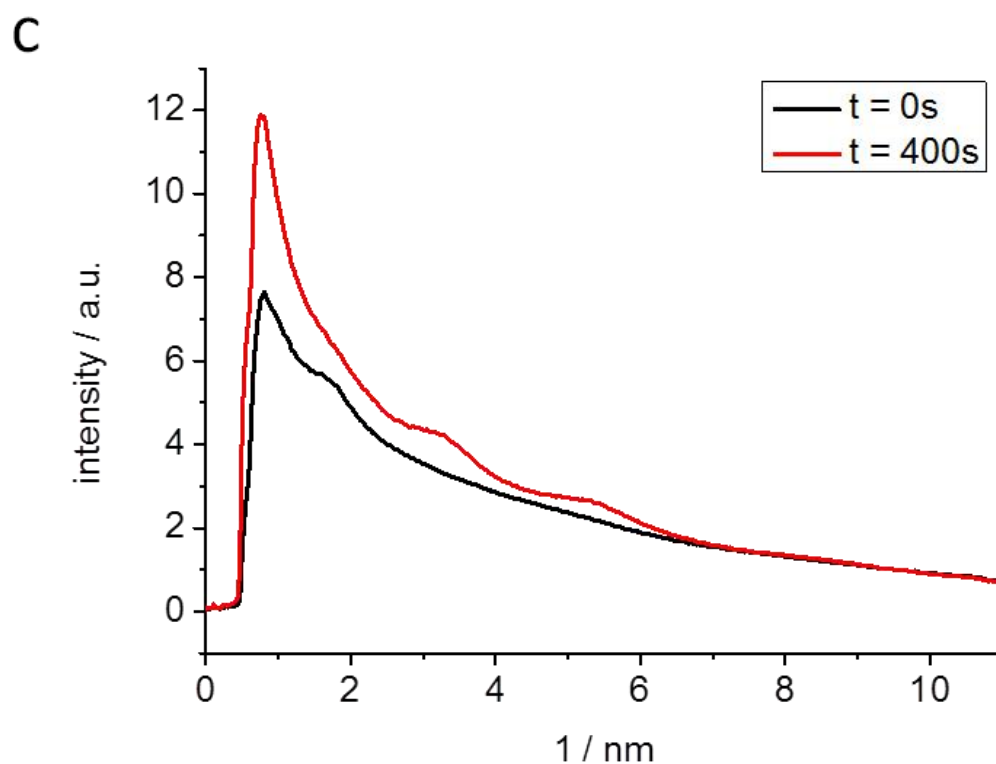
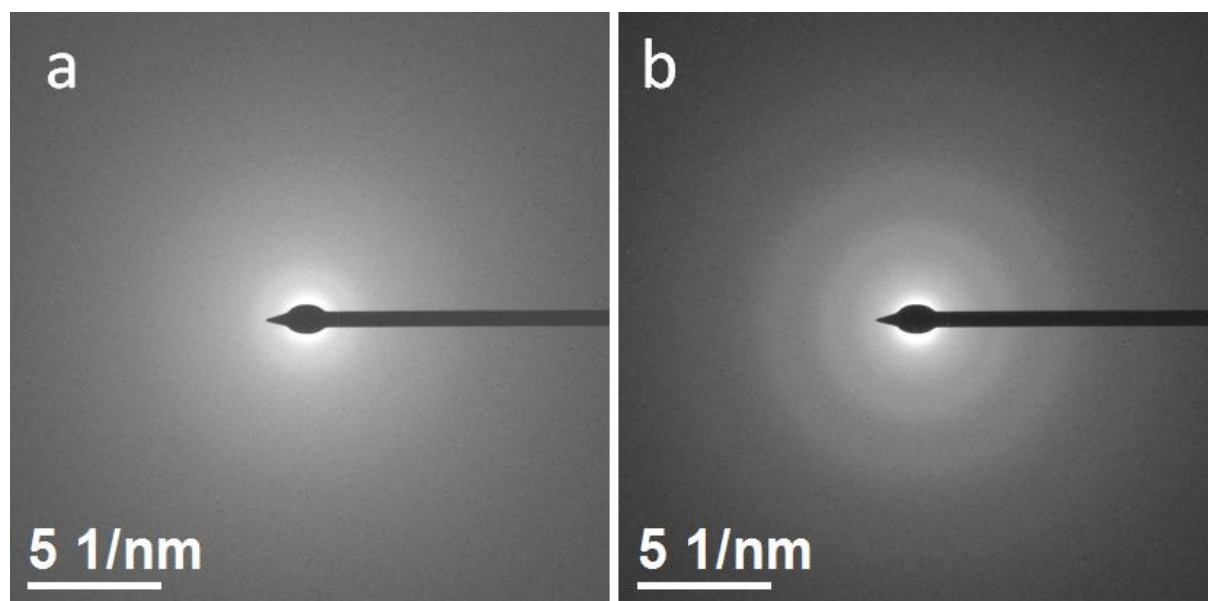


Figure 46: Xanthate/MDMO-PPV *in situ* TEM experiment; a) SAED at start ($t=0\text{s}$); b) SAED at $t=400\text{s}$; c) Radial intensity profile for $t=0\text{s}$ and $t=400\text{s}$.

Figure 47a shows an optical image of the area exposed to the electron beam. A change in color is visible, most likely due to a change in thickness during decomposition of the precursor, but also potentially due to change of the polymer because of beam damage. Figure 47b shows nanoparticles inside the nanocomposite layer. They are in the range of 2-4 nm and distributed regularly. A well connected network including percolation paths is to be expected, which could make this method an interesting alternative for thermal processing – of course the issues of beam damage and up scaling would need to be addressed. The crystallinity of the nanoparticles should also be investigated using HRTEM. This was avoided as it would require bringing the specimen into one of the high end microscopes and potentially contaminating them with volatile byproducts.

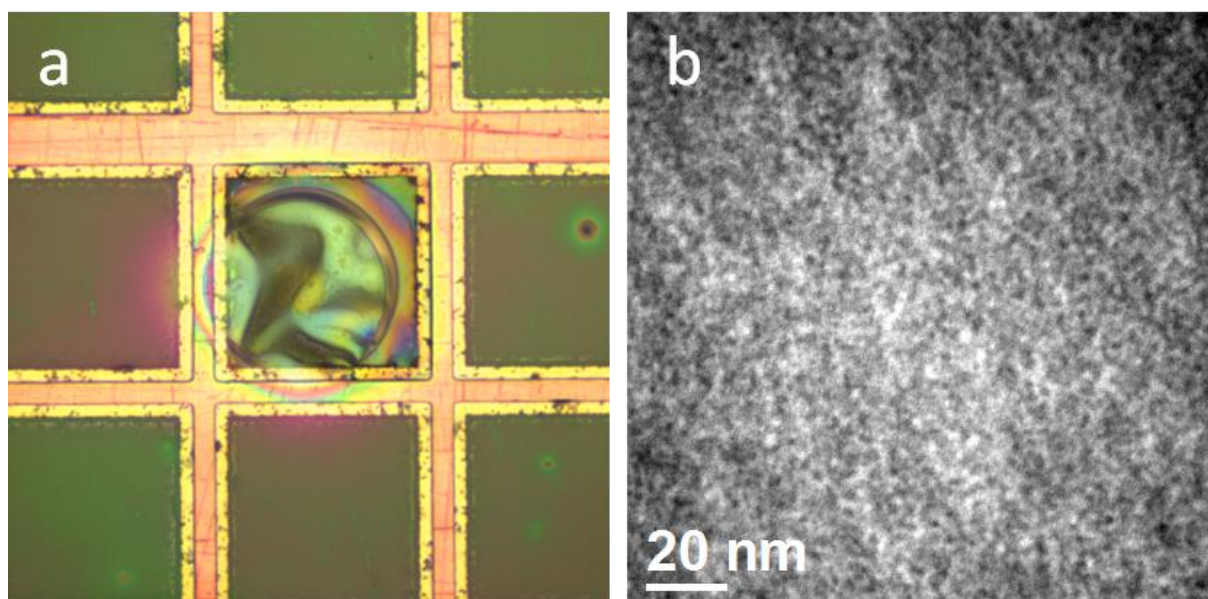


Figure 47: Xanthate/MDMO-PPV *in situ* experiment; a) Optical microscope image of the area affected by the electron beam; b) TEM-BF image showing the formation of nanoparticles.

4.4 Comparison of different precursor/polymer systems

Combining inorganic nanoparticles with organic polymers yields an almost endless number of combinations. Finding the perfect system with good device performance is not a simple task. Theoretical approaches can be applied, such as matching the band-gap of the polymer and inorganic phase. This method allows pre-selecting combinations that are likely to have good theoretical open circuit voltage. However data is often not available or reliable, especially in case of the polymers. The precursor materials for the inorganic phase and the polymer need to be dissolved, coated and transformed into a nanocomposite solar cell. These practical aspects cannot be answered by theoretical assumptions and require experimental work. Screening material combinations can be tedious, and often the only feedback from the experiment is the I-V-curve. Here electron microscopy can help in understanding the experimental results and why one system is performing well whereas the other one is not.

4.4.1 Metal sulfides in P3EBT

As mentioned before the combination of various organic donor and inorganic acceptor materials opens a multitude of possible systems for nanocomposite solar cells. In a first step, different combinations of P3EBT and metal sulfides were tested for their feasibility as solar cell materials. Of these materials, CIS was already established successfully in the project and hence not included in this study. PbS, CdS and ZnS were investigated as potential alternatives in P3EBT. They were

synthesized starting from metal salts and thiourea, coated on NaCl as thin films and characterized using TEM. Additionally devices were built for electrical characterization. Details of the experimental procedure (both preparation and investigation) for PbS, CdS and ZnS nanoparticles is described elsewhere.²⁷

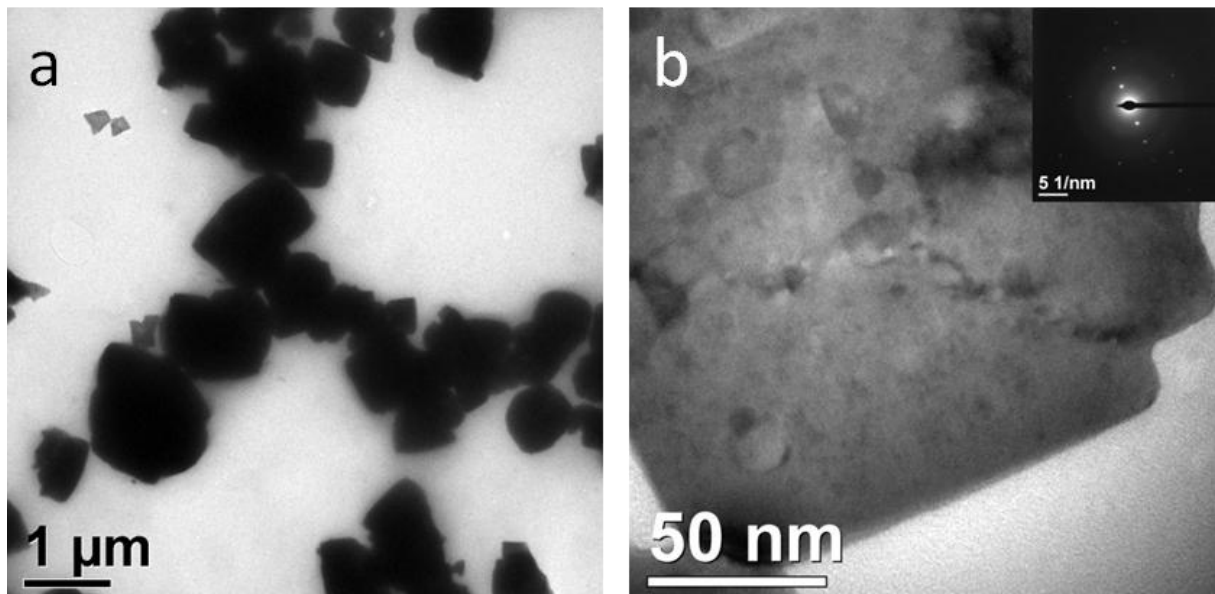


Figure 48: TEM-BF for PbS/P3EBT synthesized from metal salts and thiourea. Overview image (a), higher magnification and SAED (b).

TEM-BF imaging of the PbS/P3EBT specimen (figure 48a) shows that the resulting particles are in the range of 500-1000 nm. SAED (see figure 48b, inset) shows the diffraction pattern of a single PbS crystal in [0 0 1] orientation.

Considering the intended thickness of the active layer is in the range of 60-200 nm, the PbS nanoparticles are too large and not usable. Hence no devices were built and investigated.

A network of CdS nanoparticles with a size of 5-10 nm can be observed in TEM-BF (figure 49a). SAED shows good correlation with the JPCDS reference pattern 41-1049 for wurtzite CdS. The HRTEM image shows a single CdS nanoparticle with a d-spacing of 0.336 nm, which corresponds to the (0 0 2) spacing. The current-voltage plot of a device built using CdS/P3EBT (figure 50) reveals that the open circuit voltage (510 mV) is acceptable, the current density ($460 \mu\text{A}/\text{cm}^2$) and fill factor (0.28) are rather low, yielding a power conversion efficiency is below 0.1%.

TEM-BF imaging (figure 49b) shows ZnS nanoparticles with a size of 2-5 nm. SAED shows a good match for sphalerite structure (JCPDS 5-566). The HRTEM image shows a single nanoparticle with a d-spacing of 0.315 nm, which corresponds to the (1 1 1) spacing. An open circuit voltage of 610 mV was measured, but the short current density ($8 \mu\text{A}/\text{cm}^2$) is not higher than the one of devices built using only P3EBT without inorganic phase. The calculated power conversion efficiency is below $10^{-3}\%$, which can be considered as no photoelectric activity.

A comparison between the two specimens shows that the CdS nanoparticles are larger and seem to build up a better network with percolation paths than in the ZnS specimen. Considering the poor current density within the ZnS device, a better connection between the nanoparticles, allowing efficient transfer of the current, could provide an improvement.

Of the three alternatives to CIS investigated here CdS showed the best initial results. The usage of Cd, especially in environmentally friendly products such as solar cells, is often frowned upon. Hence CdS was not included for further research and CIS remained the main inorganic phase for the project.

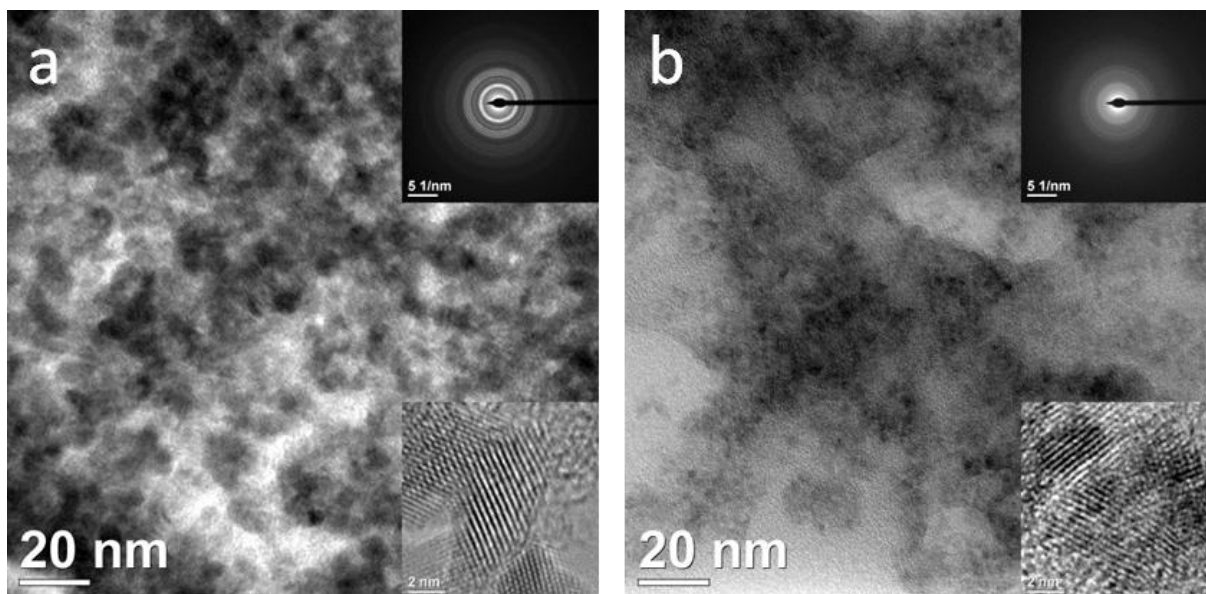


Figure 49: TEM-BF for CdS/P3EBT synthesized from metal salts and thiourea. (a); TEM-BF for ZnS/P3EBT synthesized from metal salts and thiourea (b). Insets show the SAED and HRTEM.

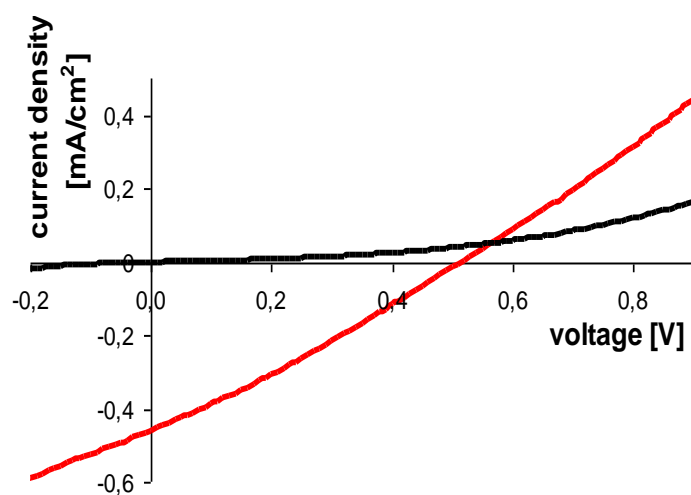


Figure 50: I-V curve of a device using the CdS/P3EBT system; measured by E. Maier

Table 9: Parameters for CIS/PPV and CIS/P3EBT (V_{oc} — open circuit voltage; J_{sc} — short circuit current density; FF — fill factor; PCE — power conversion efficiency).

System	V_{oc} / mV	J_{sc} / mA/cm ²	FF	efficiency / %
CdS/P3EBT	510	0.460	0.28	<0.1
ZnS/P3EBT	610	0.008	0.22	<10 ⁻³

4.4.2 CIS from metal salts in polymers

Two systems, both using metal salts and different sulfur sources (thioacetamide/thiourea) were investigated: CIS/PPV and CIS/P3EBT.

In the CIS/PPV system nanoparticles are synthesized from metal salts and thioacetamide. Additionally, unlike the other systems investigated in this work, PPV was not simply dissolved, but also formed from a precursor during the thermal conversion step. For experimental details see elsewhere.²⁹

In the CIS/P3EBT metal system salts and thiourea are used as precursor materials for the formation of CIS and ZCIS (CIS doped with small amounts of zinc in the precursor solution) nanoparticles in P3EBT. The details on the procedure can be found elsewhere.²⁸

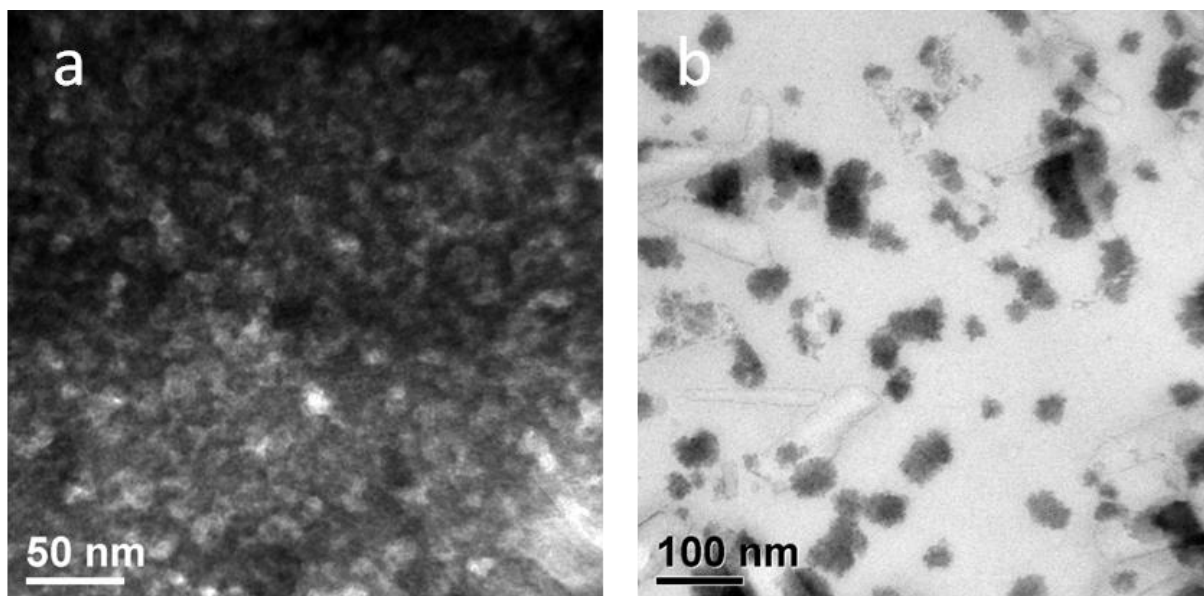


Figure 51: TEM-BF images of CIS/PPV of specimens with high CIS concentration (a) and low CIS concentration (b).

Figure 51a shows a dense network of CIS nanoparticles; however some bright areas, consisting only of polymer can be seen. The image taken from a specimen with lower CIS concentration (figure 51b) shows some CIS agglomerates with a size of 30-70 nm and large areas, where only polymer is present. As no percolation pathways are present throughout the polymer, the current density in this case would be highly reduced. Even in the case of a higher CIS concentration it can be assumed that intermixing between polymer and CIS is limited.

The TEM-BF images in figure 52 show ZCIS, most likely in form of agglomerates, whereas the light regions consist only of polymer. While an area with low content of the inorganic phase was investigated for better visibility, the images show that separation of the phases is also an issue in this system and connected pathways to the electrodes may only appear at high concentrations of the inorganic phase. Additionally some of the agglomerates are significantly darker than the rest. As the images are the two-dimensional projection of a three-dimensional film this could be because of overlapping particles in the Z-direction, but also because of Bragg contrasts. The specimen was tilted to various angles towards the beam, e.g. 10° (see figure 52b) to investigate this possibility. No change was observed, ruling out Bragg contrast.

To validate the assumption that the dark areas are agglomerates of smaller nanoparticles, dark field imaging was used. Figure 53 shows a TEM-BF image of an agglomerate (a). Four TEM-DF images (b) were taken at different rotation angles by placing the objective aperture in diffraction mode on the ring corresponding to the (2 0 4) reflection. They show individual crystals with a size of 4-6 nm within the agglomerate. Additionally a composite image (c) shows an overlap of the images in (b).

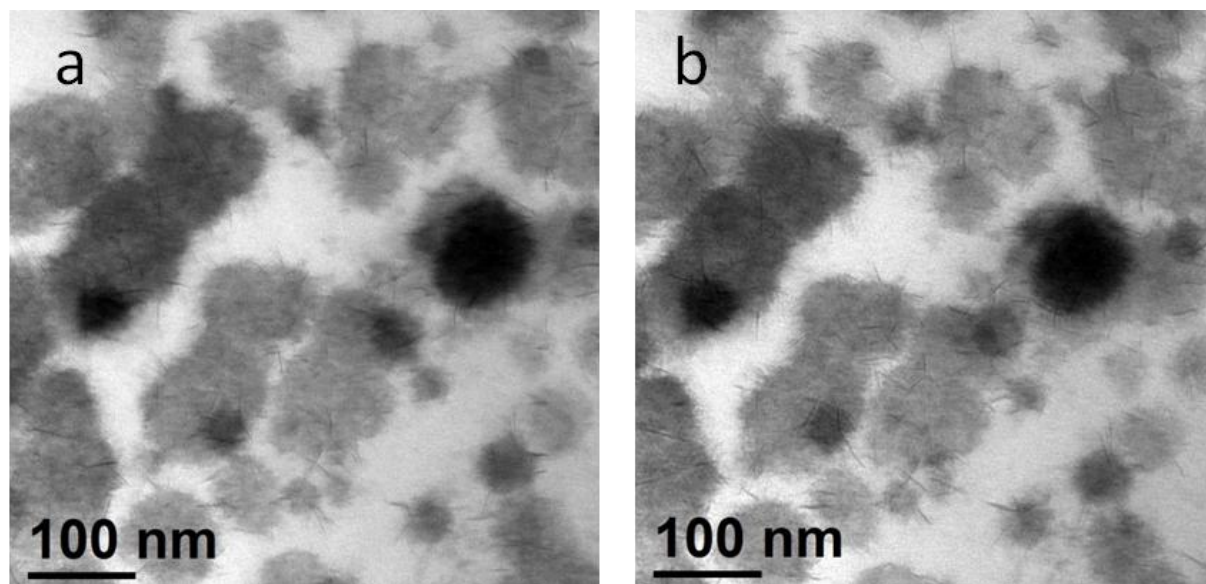


Figure 52: TEM-BF images of ZCIS/P3EBT taken at a tilt angle of 0° (a) and 10° (b).

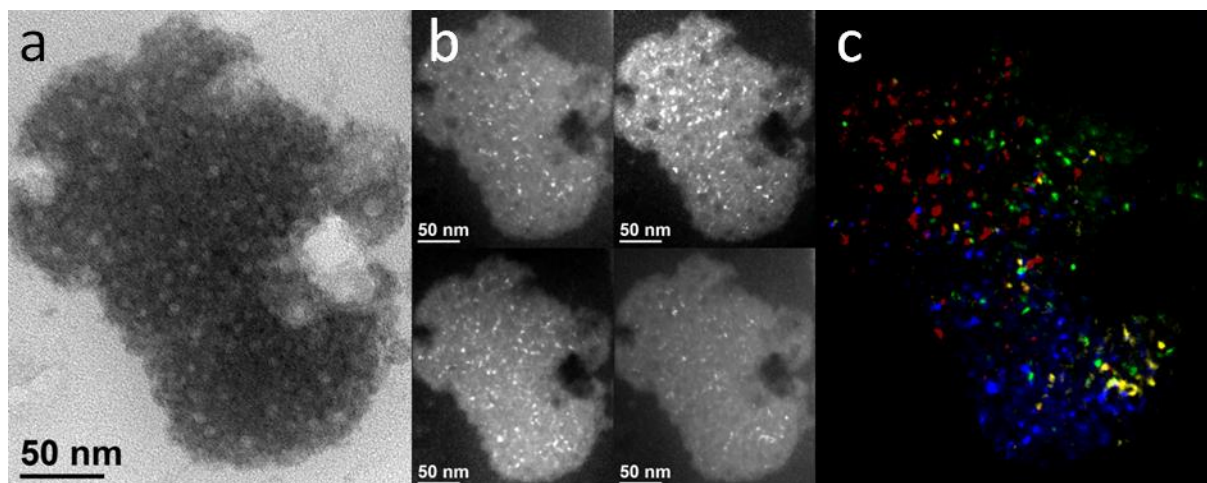


Figure 53: TEM-BF of ZCIS/P3EBT; (a), TEM-DF (b) and composite image of the four TEM-DF images (c).

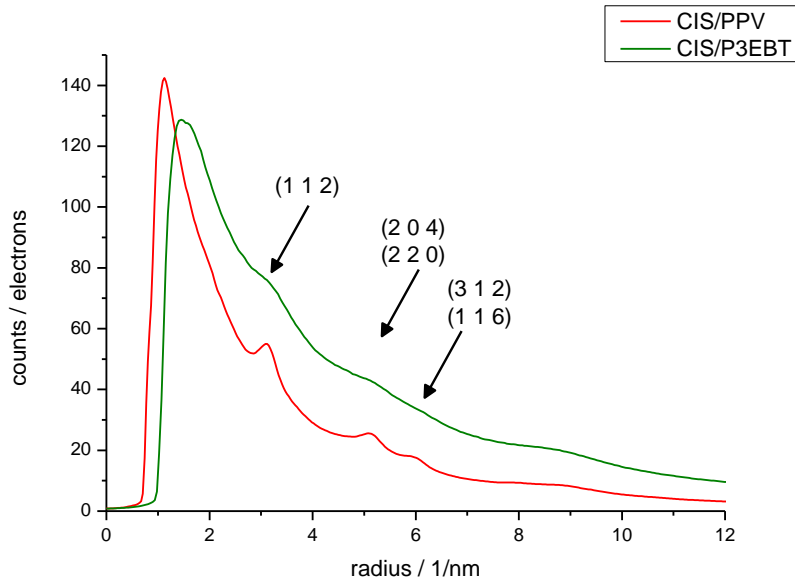


Figure 54: Radial intensity profile gained from SAED for CIS/PPV and ZCIS/P3EBT.

Radial intensity profiles from SAED are shown in figure 54. While both specimens are in good agreement with literature (JCPDS #42127), the peaks are very broad for the CIS/P3EBT system. This can be caused by a very small size of the crystallites, or simply a thick sample. As the crystallite size was already determined by DF imaging (figure 53), this effect can be attributed to sample thickness.

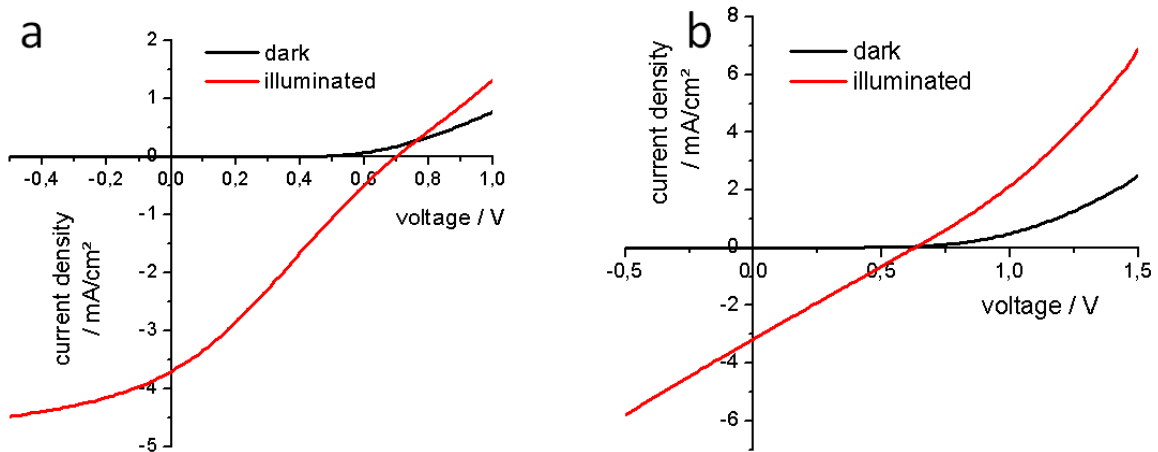


Figure 55: I–V curve of a device using the CIS/PPV system (a); I–V curve of a device using the ZCIS/P3EBT system (b); measured by T. Rath.

Figure 55 shows the I–V curves for devices using CIS/PPV (a) and ZCIS/P3EBT (b). The key parameters for both systems are listed in table 10. In both systems the open circuit voltage is good, but the short circuit current density is rather low. This effect can be explained by the phase separation observed in TEM and a lack of pathways for charge transport. Additionally, the fill factor is low for both systems. In case of the CIS/PPV system the curve is also s-shaped. This usually occurs when excitons cannot be separated due to lack of interfaces within the range of their lifetime (~ 15 nm). Figure 51b shows an area with lower CIS concentration, in which this scenario is fulfilled. The CIS agglomerates shown

there are in the range of 30-150 nm in diameter, with regions consisting only of polymer between them. Apart from problems in exciton separation additional issues are caused by the lack of percolation pathways.

Table 10: Parameters for CIS/PPV and CIS/P3EBT (V_{oc} — open circuit voltage; J_{sc} — short circuit current density; FF — fill factor; PCE — power conversion efficiency).

System	V_{oc} / mV	J_{sc} / mA/cm ²	FF	efficiency / %
CIS/PPV	700	3.7	0.27	0.6
CIS/P3EBT	630	3.2	0.25	0.5

Overall the device performance and reproducibility of the CIS/PPV system was low. Using a water-based precursor solution and a precursor polymer was identified as one of the factors needing improvement in this system. On the other hand CIS delivered the most promising results for further development. As a consequence CIS was chosen for further optimization and other polymers were investigated.

Initial experiments with CIS/P3EBT were promising, but attempts for further optimization yielded only small progress. Separation of the phases as seen in TEM seems to prevent an increase in the short circuit current. This could most likely be solved by increasing the solubility of the precursors to gain a more homogeneous film. However, in a high resolution mass spectrometry experiment melamine was found to be present in the nanocomposite layer.²⁸ The decomposition products of thiourea can form melamine through trimerization.⁸⁷ Due to the high decomposition and evaporation temperature of melamine no removal from the nanocomposite layer is possible. This was identified as a critical issue with this precursor system and steps were taken to replace thiourea by using a different precursor for sulfur.

4.4.3 Xanthate based precursor systems (CIS/F8T2, CIS/PSiF-DBT)

Ideally the precursor materials should decompose into volatile products at rather low temperatures. The ability for solving precursor materials and polymer is important for gaining a homogeneous nanocomposite layer. As shown before, the combination of metal salts and thiourea/thioacetamide was had drawbacks both concerning solubility as well as the formation of non-volatile byproducts, such as Melamine. In an effort to find new precursor materials xanthates were identified as a perfect candidate. The xanthate precursor is shown in figure 56. Unlike the previously mentioned systems the sulfur source is already contained in the metal salt. As a consequence, only the two xanthates need to be intermixed with the polymer. The solubility of the precursor can be tuned by variation of the side group. As a consequence stable and homogeneous solutions and coatings are possible.

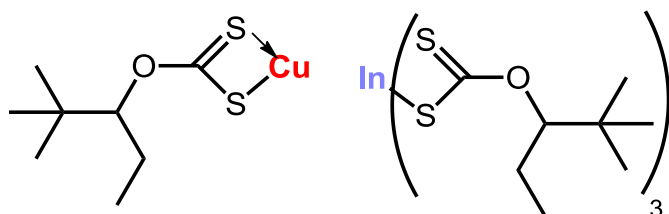


Figure 56: Chemical structure of the Cu- and In-xanthate precursor.³⁰

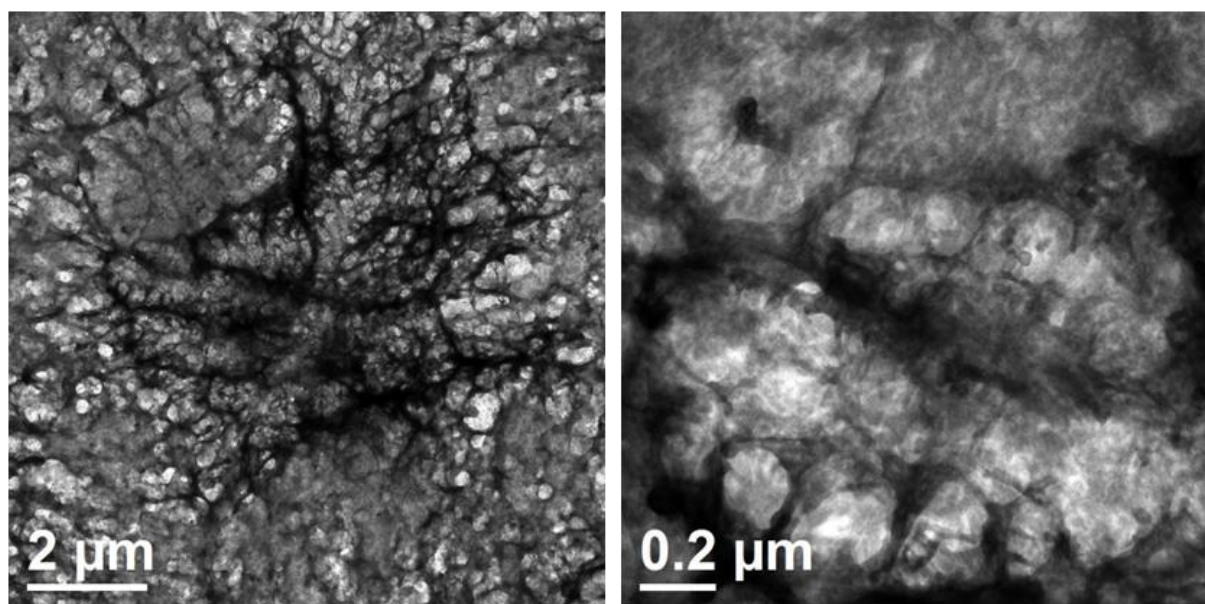


Figure 57: TEM-BF images of the CIS/F8T2 system using a xanthate precursor.

A xanthate based precursor was used in combination with F8T2. The TEM-BF images in figure 57 show a huge improvement CIS/PPV (figure 51) and ZCIS/P3EBT (figure 52). These two systems are based on metal salts and a separate sulfur source (thiourea, thioacetamide) and exhibit strong phase separation. In case of the xanthate system phase separation is highly decreased and a network of small nanoparticles is formed during the thermal conversion step. No huge agglomerates are found, nor regions consisting of only polymer. On a larger scale bubble like structures can be seen, and also side walls of the bubbles in which the nanocomposite seems to be thicker than in the other regions. AFM measurements (not shown) confirm that the surface is very uneven. It is known from literature that F8T2 can be subject to these morphological changes because of recrystallization during

heating/cooling.⁸⁸ Consequently steps were taken to optimize the heating program in an attempt to minimize these effects; please refer to chapter 4.5.2 for details.

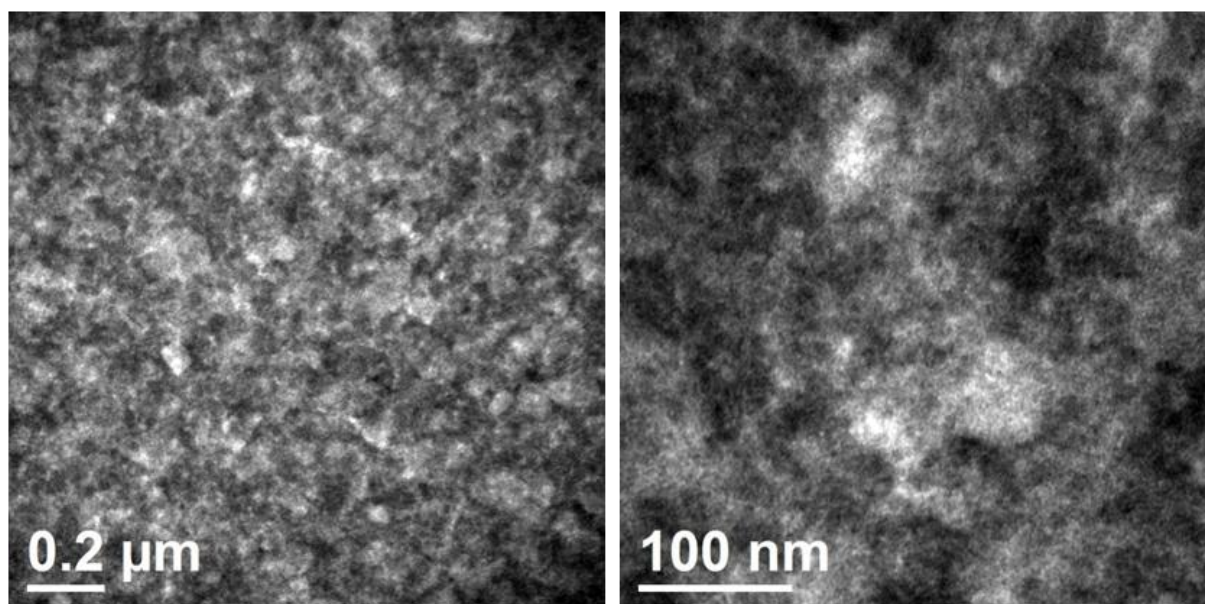


Figure 58: TEM-BF images of the CIS/PSiF-DBT system using a xanthate precursor.

Figure 58 shows TEM-BF images of the xanthate precursor based CIS/PSiF system. Similar to the system using F8T2 small, evenly distributed nanoparticles can be observed. Overall the specimen looks more homogeneous, no bubbles or strings can be found. Compared to the metal salt / thiourea or thioacetamide based systems there is much less phase separation – as long as precursor is present small nanoparticles are formed to build up a network. The even distribution of the nanoparticles confirms that the precursor is solved homogeneously in the polymer.

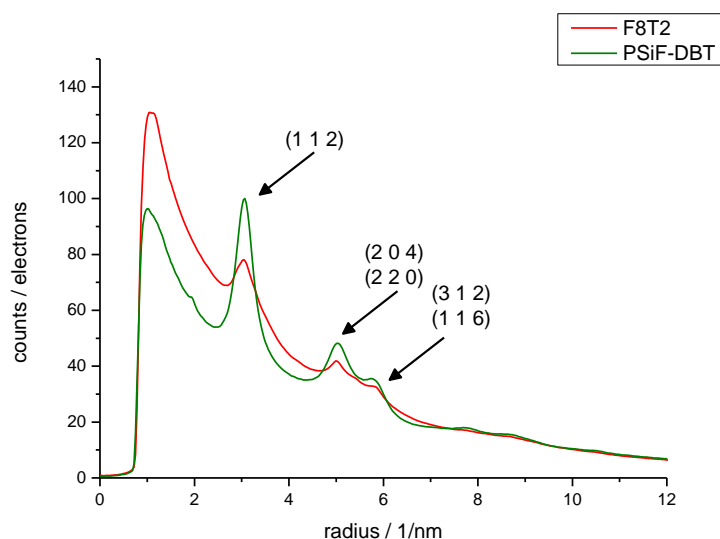


Figure 59: Radial intensity profile gained from SAED for CIS/F8T2 and ZCIS/CIS/PSiF-DBT.

Figure 59 shows radial intensity profiles from SAED for both systems. In case of F8T2 the peaks are less distinctive than in the PSiF-DBT based specimen. This is most likely due to multiple scattering within the thick regions specimen.

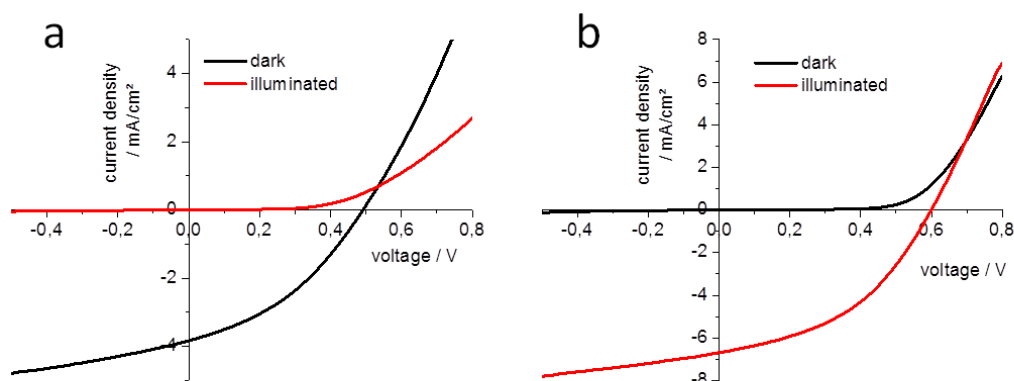


Figure 60: I–V curve of a device using the CIS/F8T2 system (a); I–V curve of a device using the CIS/PSiF-DBT system; measured by M. Edler.

Table 11: Parameters for CIS/F8T2 and CIS/PSiF-DBT, (V_{oc} — open circuit voltage; J_{sc} — short circuit current density; FF — fill factor; PCE — power conversion efficiency).

System	V_{oc} / mV	J_{sc} / mA/cm ²	FF	efficiency / %
CIS/F8T2	490	3.8	0.38	0.7
CIS/PSiF-DBT	600	6.7	0.43	1.7

Figure 60 and table 11 show the I-V plots and relevant key parameters for the two xanthate based systems. Both of them outmatch the previously discussed systems using metal salts and thiourea (CIS/P3EBT) or thioacetamide (CIS/PPV) as precursor. The system using F8T2 has a rather low open circuit voltage. Its short circuit voltage is in the same range as CIS/PPV and CIS/P3EBT, most likely due to the variation between thick and thin regions not providing ideal pathways for charge transport to the electrodes. The fill factor of the xanthate based system using F8T2 is better than CIS/P3EBT and CIS/PPV, and the I-V curve does not feature the s-shaped look of the CIS/PPV system (see figure 55). These parameters result in higher device efficiency than CIS/P3EBT and CIS/PPV. The device using PSiF-DBT outperforms all previous devices including the xanthate based F8T2 system with good open circuit voltage, short circuit current density and fill factor, yielding an overall power conversion efficiency of 1.73%. This is in good accordance with the network of small nanoparticles found in TEM.

4.5 Process optimization of xanthate based systems

Due to good solubility and processing properties the xanthate precursor opened up new possibilities of polymers. Both F8T2 and PSiF-DBT showed good results in the first experiments and further steps were taken to optimize the systems. Additionally, new polymers (MEH-PPV and MDMO-PPV) were tested for their feasibility and included in the optimization experiments.

Special attention was paid to the Cu/In ratio. The inorganic phase is used as an electron acceptor material, so an n-type semiconductor is necessary. However, Cu-rich or stoichiometric CIS is a p-type semiconductor. An excess of indium turns CIS into an n-type semiconductor.⁸⁹

Early optimization experiments on the CIS/P3EBT system found that the indium precursor ($InCl_3$) is highly volatile. In order to gain an excess of indium in the nanocomposite solar cell an even higher excess of $InCl_3$ is needed to compensate the evaporation losses, which were approximately one third of the indium precursor used according to SEM-EDXS measurements. Devices using different precursor ratios were built and compared. A Cu/In ratio of 1/1.7 yielded the best results in device

performance.²⁸ Using the same precursor ratio on the xanthate precursor system, a Cu/In ratio of 1/1.6 was found using TEM-EDXS after processing. However, indium losses were smaller in this case. Obviously the type of precursor (different metal salts or xanthate) will influence the amount of indium lost during conversion due to its decomposition behavior and general volatility. To understand and optimize the process, the conditions, especially those leading to a loss of indium need to be understood. Otherwise the chemical composition of the nanocomposite layer will often be undetermined or random, resulting in a bad over device performance. In this chapter, the influence of temperature, pressure, precursor ratio and the type of oven used for the thermal decomposition step will be examined.

4.5.1 Variation of temperature profile during CIS formation (F8T2)

With good initial results in the CIS/F8T2 system, steps were taken to optimize the thermal conversion step for F8T2. As mentioned before, recrystallization is the main issue of F8T2, causing the polymer to form bubbles and thick strings, whereas other regions remain thin.

Three different heating programs were compared for their effect on thin films produced on NaCl single crystals:

Temperature program 1: 25°C – ramp to 200°C in 7 minutes – hold for 15 minutes – cool down

Temperature program 2: 25°C – ramp to 200°C in 20 minutes – hold for 15 minutes – cool down

Temperature program 3: 25°C – ramp to 120°C in 4 minutes – hold for 20 minutes - ramp to 200°C in 3 minutes – hold for 15 minutes – cool down

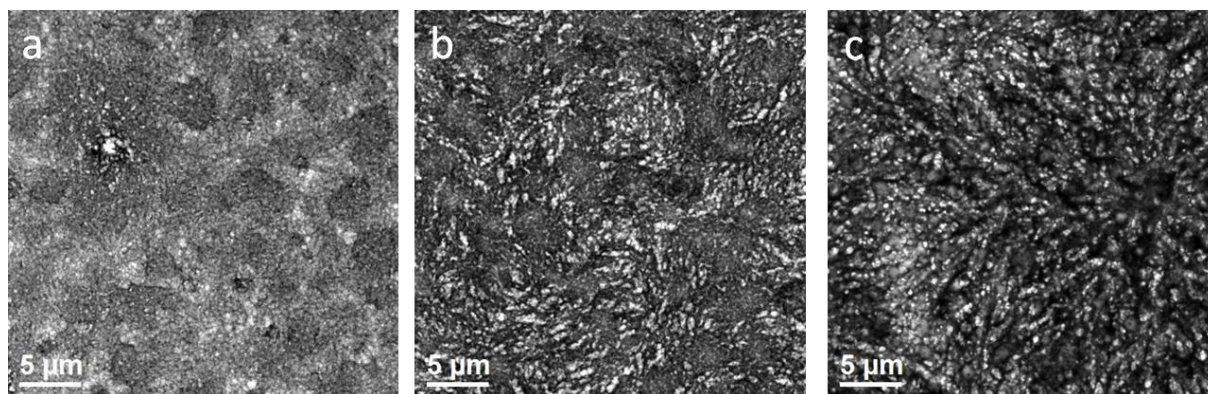


Figure 61: TEM-BF images CIS/F8T2 thin films processed using temperature program 1 (a), 2 (b), 3 (c).

TEM-BF images for specimens produced using the three previously mentioned temperature programs are shown in figure 61. There is an increasing trend to form bubbles and strings with longer heating times (program 2 and 3). This can also be observed in the radial intensity profiles from SAED (figure 62). Only broad peaks can be seen for program 2 and 3. The TEM-BF images in figure 57 and table 11 correspond to program 1 and are the best results that could be gained with this system. Solar cells produced using program 2 and 3 yielded devices with no or very poor power conversion efficiency; hence no I-V-curves can be shown. Since increasing the heating time had negative impact on device performance, the heating time should be reduced – which conflicts with the formation process of CIS from the xanthate precursor. Consequently F8T2 was abandoned in favor of PSiF-DBT and new polymers (MDMO-PPV/MEH-PPV).

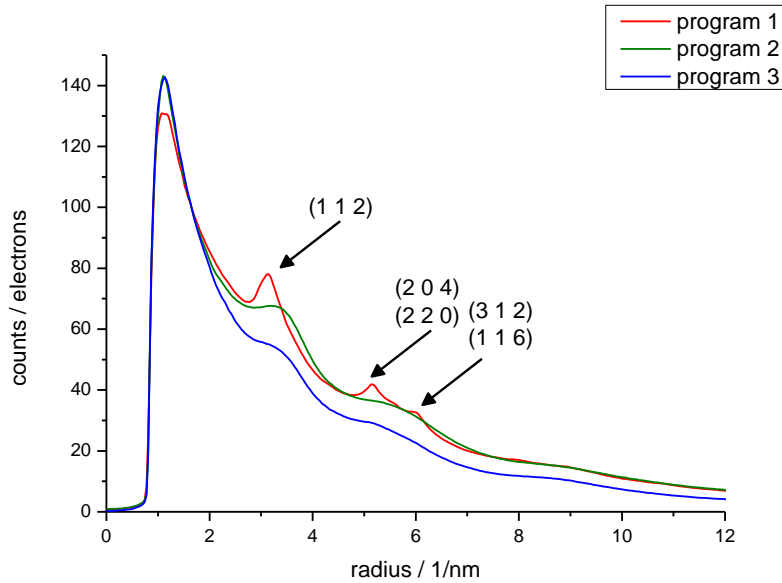


Figure 62: Radial SAED intensity profiles for samples processed using temperature program 1 (a), 2 (b), 3 (c).

4.5.2 Comparison of heating conditions (MEH-PPV)

Initially two types of set-ups were tested for the thermal conversion step: A furnace oven, where the devices were heated under vacuum conditions and a heating plate in argon atmosphere. The atmosphere plays an important role in the process – on one hand volatile byproducts are formed during the process, on the other hand indium is known to evaporate during heating. As mentioned before the Cu/In ratio is an important factor in device performance. While the composition of inorganic phase obviously depends on the ratio between precursors the influence of the conditions during the heating step also needs to be considered.

Solar cells and TEM specimens were made from two starting ratios (Cu/In 1/1 and 1/1.7). In one case they were heated in the furnace oven under vacuum conditions, the second set-up consisted of the heating plate in argon atmosphere. The composition of the resulting nanocomposite films was investigated in TEM-EDXS. MEH-PPV was used as polymer in this experiment.

Table 12: Experimental details and results from TEM-EDXS for specimens A-D

specimen	A	B	C	D
Cu/In	1/1	1/1	1/1.7	1/1.7
Oven	furnace oven	heating plate	furnace oven	heating plate
Conditions	vacuum	argon	vacuum	argon
Cu /at%	25.1±1.1	25.4±1.4	19.3±1.6	19.4±0.6
In /at%	25.2±0.6	27.7±0.3	31.4±0.5	34.1±0.4
S /at%	49.8±1.0	46.9±1.2	49.3±1.7	46.5±0.5
Cu/In 1/x	1.00	1.09	1.63	1.76
(Cu+In)/S 1/x	1.01	1.13	1.03	1.15

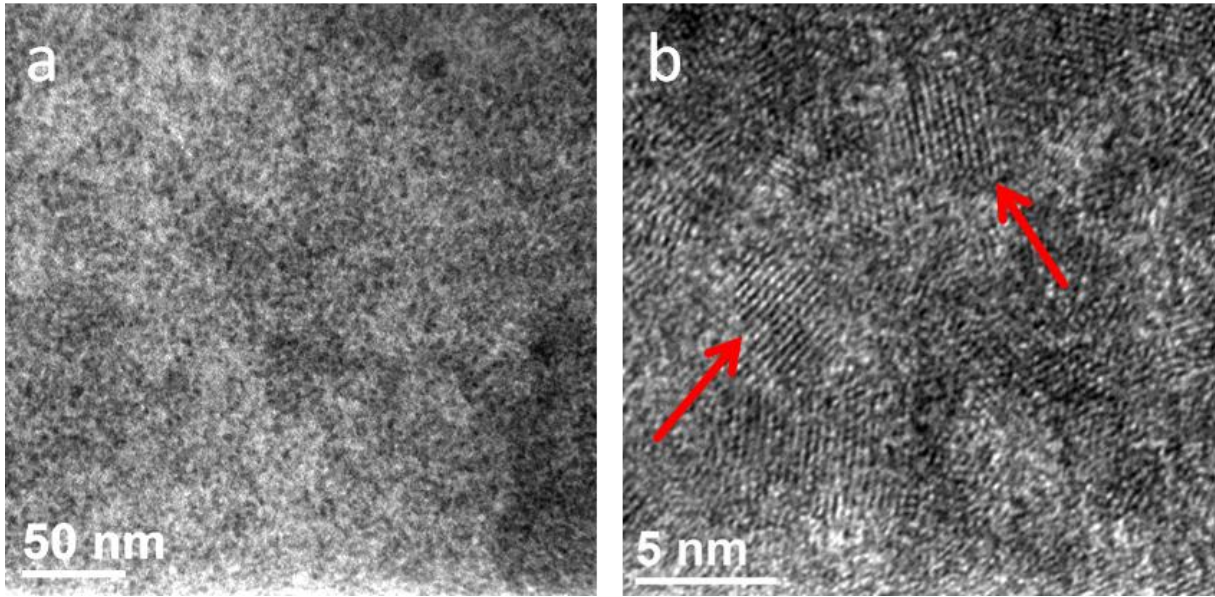


Figure 63: TEM-BF (a) and HRTEM showing individual nanoparticles (b) for specimen C.

Figure 63 shows typical TEM-BF and HRTEM images for specimen C. An intermixed network between polymer and nanoparticles can be observed. The HRTEM image shows individual nanoparticles in the range of 5 nm.

Table 12 gives an overview of the specimens and experimental conditions used in this experiment. In both cases of a precursor ratio (Cu/In 1/1 and 1/1.7) more indium is present when using the heating plate than in the furnace oven. However, this ratio can easily be adjusted by changing the precursor ratio.

The ratio between the metals (Cu+In) and S should ideally be 1, which is matched very well when using the furnace oven. In case of the heating plate, this ratio is in favor of the metals – sulfur is missing in the CIS, or even some other phase has been formed. This may be explained by the fact, that the heating plate only heats the sample from one direction, potentially creating a heat gradient inside of it, while the furnace oven is providing heat from all sides.

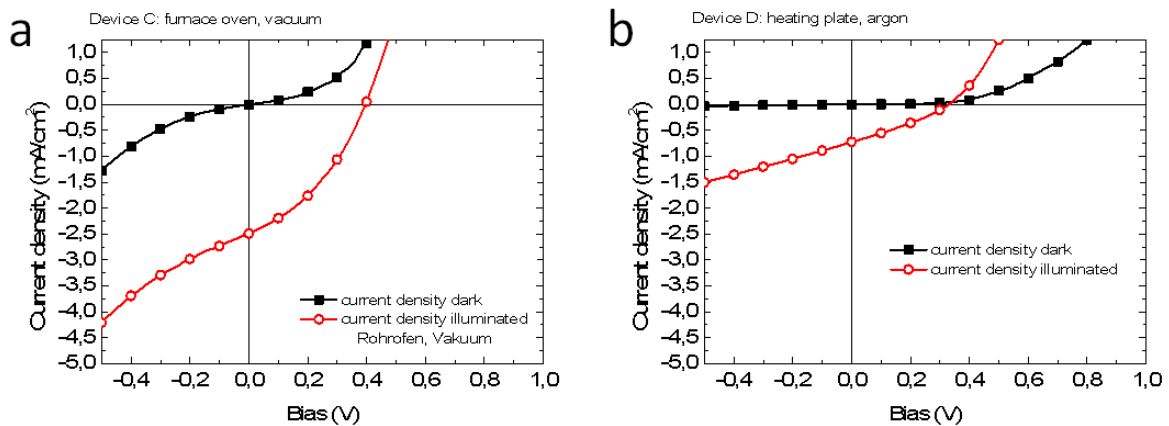


Figure 64: I-V curves for specimen C (furnace oven) and D (heating plate, argon); measured by T. Rath.

Table 13: Parameters for CIS/PPV and CIS/P3EBT (V_{oc} — open circuit voltage; J_{sc} — short circuit current density; FF — fill factor; PCE — power conversion efficiency).

Specimen	Cu/In	V_{oc} / mV	J_{sc} / mA/cm ²	FF	efficiency / %
A (furnace oven, vacuum)	1/1	0.18	0.73	0.29	0.04
B (heating plate, argon)	1/1	0.34	1.20	0.31	0.13
C (furnace oven, vacuum)	1/1.7	0.40	2.49	0.36	0.36
D (heating plate, argon)	1/1.7	0.34	0.73	0.29	0.07

Table 13 shows the key parameters for devices made using the parameters described. The efficiency of devices using a Cu/In ratio of 1/1 is poor – which can be expected due to formation of a p-type semiconductor. Devices using a Cu/In ratio of 1/1.7 show higher power conversion efficiency, their I-V curves are listed in figure 64. Using the furnace oven yielded better results than the heating plate. Additionally they were more reproducible than with the heating plate and as a consequence the furnace oven under vacuum conditions became the standard method for device preparation.

4.5.3 Variation of temperature profile during CIS formation (MDMO-PPV)

The influence of the temperature profile during the thermal conversion was investigated. For this purpose the Cu- and In-xanthates were used in MDMO-PPV at a Cu/In rate of 1/2.2 and polymer/CIS rate of 1/9. Films were spin-coated on NaCl single crystals at 300 rpm*s⁻¹//1000rpm//30 s.

Temperature program 1: 25°C – ramp to 160°C in 7 minutes – hold for 15 minutes – cool down

Temperature program 2: 25°C – ramp to 200°C in 7 minutes – hold for 15 minutes – cool down

Temperature program 3: 25°C – ramp to 250°C in 8 minutes – hold for 15 minutes – cool down

The conversion temperatures chosen for the experiment reflect the range limited by the materials: 160°C was found to be the lower limit for the decomposition of the precursor and the formation of CIS; 250°C is the critical limit where most polymers start to degrade. 200°C is a good compromise between these two factors, ensuring both full conversion of the precursor to CIS and limiting the damage to the polymer.

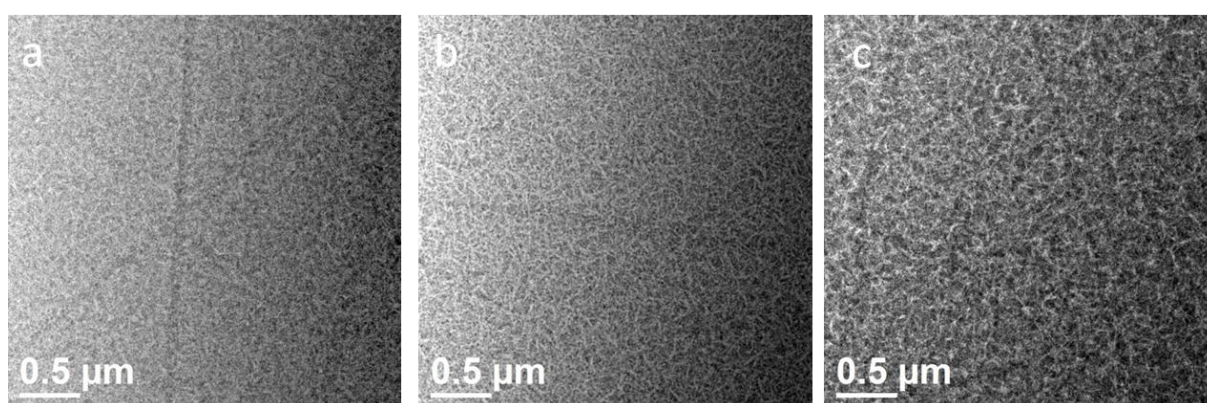


Figure 65: TEM-BF images of CIS/MDMO-PPV after heating programs 1 (a), 2 (b) and 3 (c).

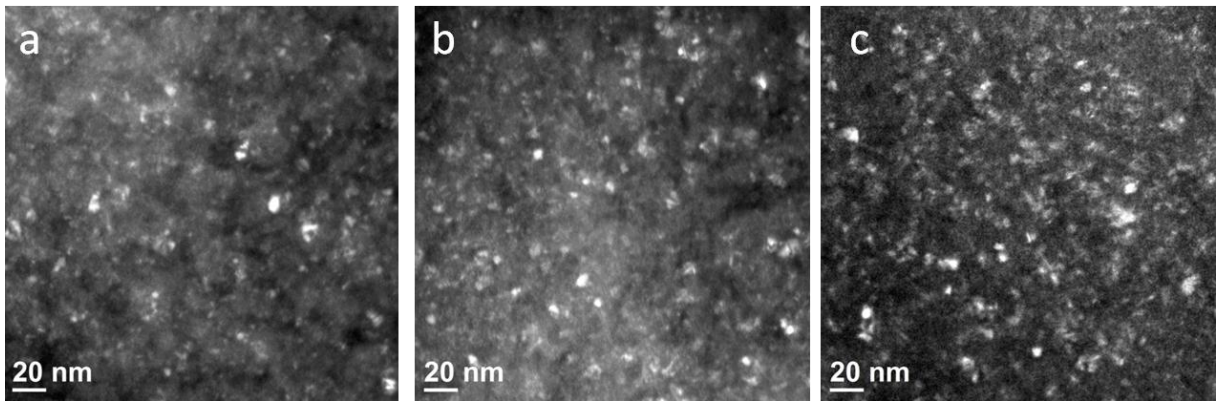


Figure 66: TEM-DF images of CIS/MDMO-PPV after heating programs 1 (a), 2 (b) and 3 (c).

TEM-BF images for the three specimens (figure 65) show that there are only small differences between the specimens recognizable. Only in case of temperature program 3 separation between bright (polymer-rich) and dark (CIS-rich) areas seems to be slightly stronger.

TEM-DF was used to identify individual crystallites within the nanocomposite layer. The images in figure 66 show very little variation in particle size between the temperatures, in general nanoparticles in the range from 2-6 nm are observed in all specimens.

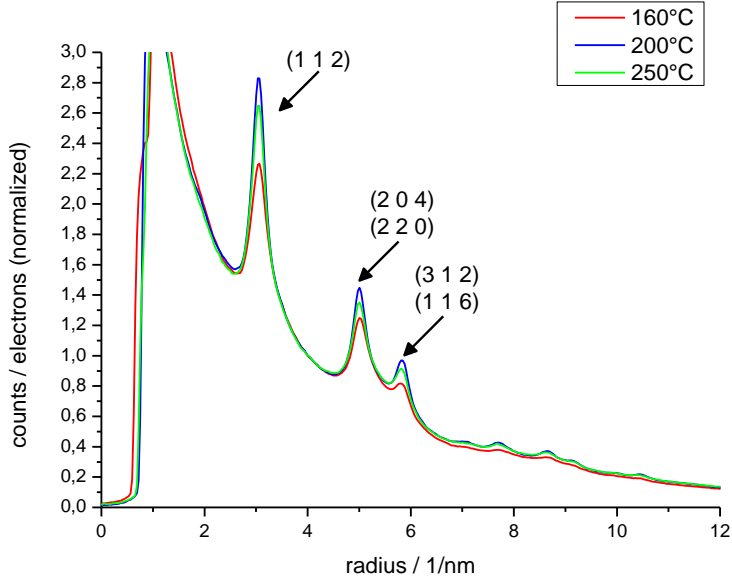


Figure 67: Radial SAED intensity profiles for CIS specimens processed using a variation of temperature programs.

Figure 67 shows radial intensity profiles from SAED. All three specimens are a good match for CIS (JCPDS #42127) and exhibit clearly defined peaks. The peaks for temperature program 2 (200°C) are the most clearly defined ones. This may relate to the crystallinity of the nanoparticles, but even though all specimens were produced using the same parameters, it could also be related to small variations in the specimen thickness.

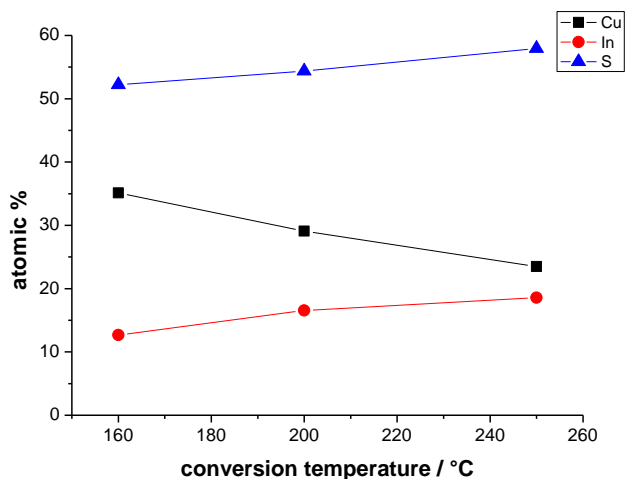


Figure 68: Composition of CIS in specimens made using temperature programs 1-3 (160, 200, 250°C) measured via TEM-EDXS.

For a deeper understanding devices were also built using the same heating parameters as the TEM-specimens – however their performance was poor compared to previous experiments. The reason was found by quantitative TEM-EDXS investigations (figure 68). All the specimens contain an excess of copper compared to indium – ideally the ratio should be reversed. Additionally, a dependency of the Cu/In ratio (and sulfur content) on the heating temperature/rate can be observed.

After checking for obvious mistakes (mistakes during production of the precursor solution, quantification errors, etc), the pressure during the conversion step was identified as the reason for the change in the Cu/In ratio. Due to improvements in sealing of the vacuum line better lower pressure was reached. This caused a significantly higher part of the volatile indium to be depleted during the conversion process and steps were taken to systematically understand the influence of the vacuum conditions.

4.5.4 Variation of Cu/In-precursor ratio

As a lesson from the previous chapter three factors need to be considered for the final composition of the device:

- Conversion temperature/heating rate
- Precursor ratio
- Pressure

Since no huge differences in particle size were observed in the range between 160 and 250°C (but changes in the Cu/In ratio), temperature program 2 (200°C for 15 minutes) was used as standard program.

The influence of precursor ratio and pressure was investigated by variation of one parameter while keeping the other one at a defined value. The experimental details for these specimens are similar to the ones in chapter 4.5.3, except for the parameter, that was varied. Pressure was set at 0.2 mbar.

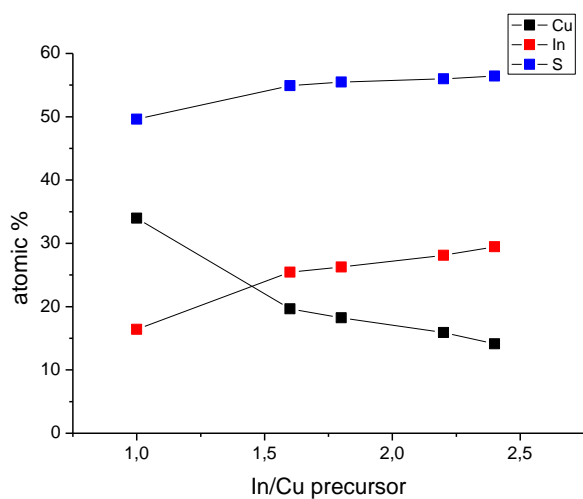


Figure 69: Composition of CIS in specimens made using various precursor ratios at 200°C and 0.2 mbar measured via TEM-EDXS.

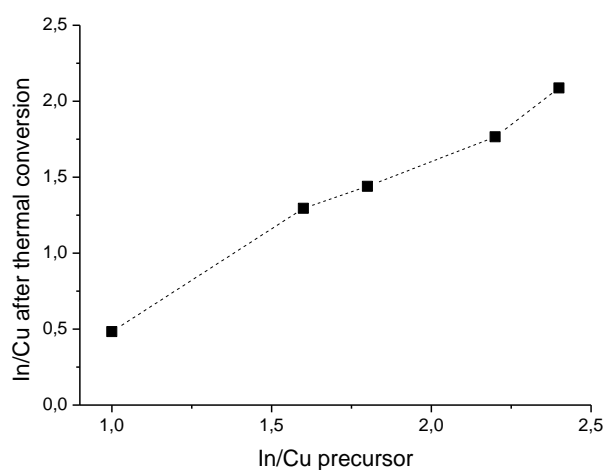


Figure 70: In/Cu ratio after thermal conversion using various precursor ratios at 200°C and 0.2 mbar measured via TEM-EDXS.

Table 14: Chemical composition (at%, from TEM-EDXS) and In/Cu ratio as shown in figure 69 and figure 70.

In/Cu precursor	Cu / at%	In / at%	S / at%	In/Cu ratio
1.0	34.0	16.4	49.6	0.48
1.6	19.7	25.5	54.9	1.30
1.8	18.2	26.3	55.5	1.44
2.2	15.9	28.1	56.0	1.77
2.4	14.1	29.5	56.4	2.09

Figure 69 and table 14 show the chemical composition of CIS measured with TEM-EDXS. The amount of indium found in the specimens is much lower than expected, e.g. at a Cu/In ratio of 1/1 in the precursor only half as much indium is found in the nanocomposite after processing. This is in contradiction to previous results, where a Cu/In ratio of 1/1 was found after processing (see table 12). However these specimens were made under different (at that time undocumented) vacuum conditions. With increasing indium concentrations in the precursor, higher concentrations of indium are also found in the resulting specimens. In figure 70 the ratio of In/Cu in the precursor is plotted against the ratio in the processed specimens. At a precursor rate Cu/In 1/2.2 an ideal rate of 1/1.7 is found in the resulting specimens.

4.5.5 Variation of vacuum pressure

In this experiment the influence of the vacuum pressure was investigated by variation of pressure while keeping the precursor ratio fixed at Cu/In 1/2.2. The experimental details for these specimens are similar to the ones in chapter 4.5.3. Pressure was set to 0.2, 2.0 and 20 mbar.

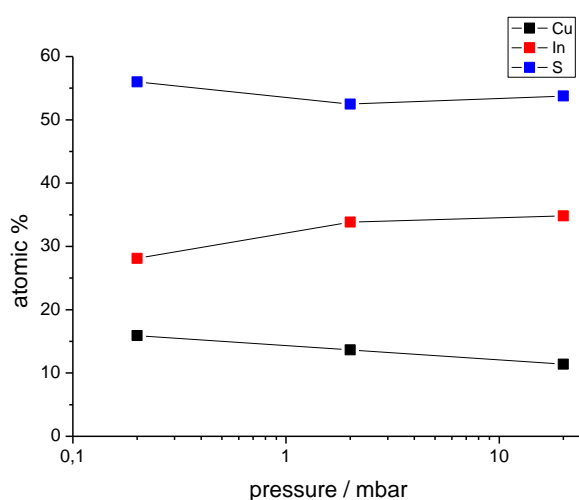


Figure 71: Composition of CIS in specimens made using various pressure setting (0.2, 2.0 and 20 mbar) at a precursor rate of Cu/In 1/2.2 measured via TEM-EDXS.

Table 15: Chemical composition (at%, from TEM-EDXS) and In/Cu ratio as shown in figure 71 and figure 72.

pressure / mbar	Cu / at%	In / at%	S / at%	In/Cu ratio
0.2	15.9	28.1	56.0	1.77
2	13.6	33.9	52.5	2.48
20	11.4	34.8	53.8	3.06

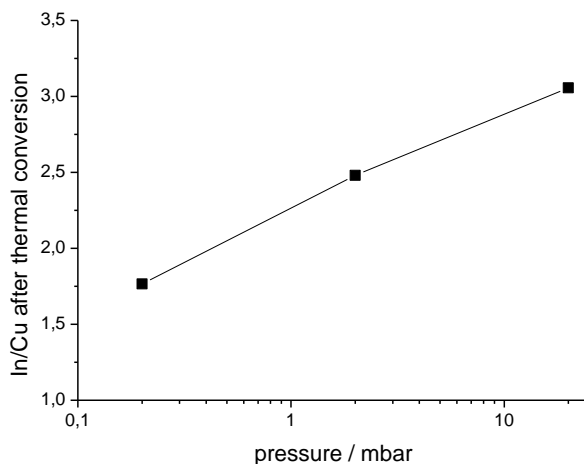


Figure 72: In/Cu ratio after thermal conversion using various pressure setting (0.2, 2.0 and 20 mbar) at a precursor rate of Cu/In 1/2.2 measured via TEM-EDXS.

The chemical composition of the specimens is shown in figure 71 and table 15. With higher pressure the indium concentration is also higher. This is in good agreement with the fact that indium is prone to being evaporated in low vacuum conditions. Comparison to the data in chapter 4.5.2 implies that the pressure in these earlier measurements was lower than 0.2 mbar.

The Cu/In ratio under different vacuum conditions is plotted in figure 72. At 0.2 mbar the desired ratio of Cu/In 1/1.7 is reached.

4.5.6 Conclusion of optimization experiments

While the need for an indium-rich phase was understood already in the early project stages, the relevant factors for a controlled process had to be studied in order to have a reproducible process. For the xanthate precursor system the composition of CIS after thermal processing is determined by 4 factors:

- Type of oven used (furnace / heating plate)
- Precursor ratio
- Vacuum pressure
- Temperature program

The furnace oven under vacuum was identified as the superior system due to sulfur losses on the heating plate with an argon atmosphere. Precursor ratio, vacuum pressure and temperature were found to influence the final composition and parameters for the conversion were found. As shown in this chapter, small changes any of these three parameters can significantly change the composition of the resulting CIS phase. TEM-EDXS has proven to be an essential tool for controlling the chemical composition of the CIS phase and helped finding a set of parameters that yield the desired Cu/In ratio of 1/1.7. A set of standard conditions can be derived: 200°C conversion temperature, precursor ratio Cu/In of 1/2.2 and 0.2 mbar.

4.6 Investigations on devices

4.6.1 CIS/PSiF-DBTⁱⁱ

A device was built using CIS from the xanthate precursor and PSiF-DBT, PEDOT:PSS (acting as hole transport layer) and aluminum electrodes. A photograph of the device is shown in figure 73a. A FIB lamella was prepared from the area marked with the red 'x' using the lift-out method. The individual layers of the device can be identified in TEM-BF (figure 73b): glass substrate (~1 mm, 1), ITO (180 nm, 2), PEDOT:PSS (40 nm, 3), active layer (85 nm, 4), aluminum electrode (270 nm, 5), protective platinum layer from FIB processing (6). The active layer is considerably thin, even though it was made using a two step process by doctor-blading of the first layer, waiting for it to dry, then doctor-blading of the second one. No border between the two layers can be observed in TEM. It can be assumed that the top of the first layer is partially dissolved during coating of the second layer, resulting in one homogeneous layer.

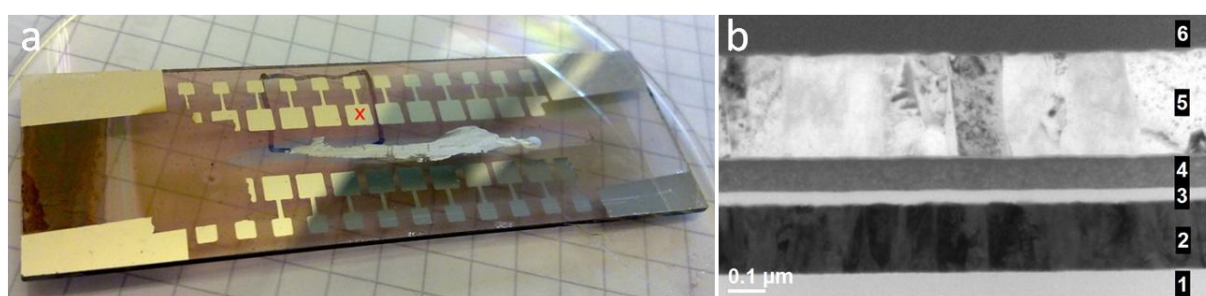


Figure 73: Photograph of the CIS/PSiF-DBT device, the red 'x' marks the electrode investigated via FIB/TEM (a), TEM-BF image showing the layers of the FIB lamella (b). 1 glass, 2 ITO, 3 PEDOT:PSS, 4 CIS/PSiF-DBT, 5 Al, 6 Pt

Figure 74a shows a thin film specimen that was floated off a NaCl single crystal in top-down view. Similar to the FIB lamella a dense network of nanoparticles with only a small tendency to form agglomerates can be observed. A high resolution image of the same specimen (figure 74b) shows the lattice fringes of individual nanoparticles in the range of 3-5 nm.

As mentioned in chapter 4.5 an excess of indium is needed to turn CIS into an n-type semiconductor. Using TEM-EDXS measurements and quantification via the thin film method a ratio of Cu/In 1/1.6 was found. This is slightly below the desirable ratio of Cu/In 1/1.7, and can be attributed to losses during the conversion step in the furnace oven caused by variations in the vacuum conditions (see chapter 4.5.5).

ⁱⁱ Parts of this chapter are already published in: Rath, T.; Edler, M.; Haas, W.; Fischereder, A.; Moscher, S.; Schenk, A.; Trattnig, R.; Sezen, M.; Mauthner, G.; Pein, A.; Meischler, D.; Bartl, K.; Saf, R.; Bansal, N.; Haque, S. A.; Hofer, F.; List, E.; Trimmel, G. A Direct Route Towards Polymer/Copper Indium Sulfide Nanocomposite Solar Cells. *Advanced Energy Materials* **2011** 6, 1046 – 1050.

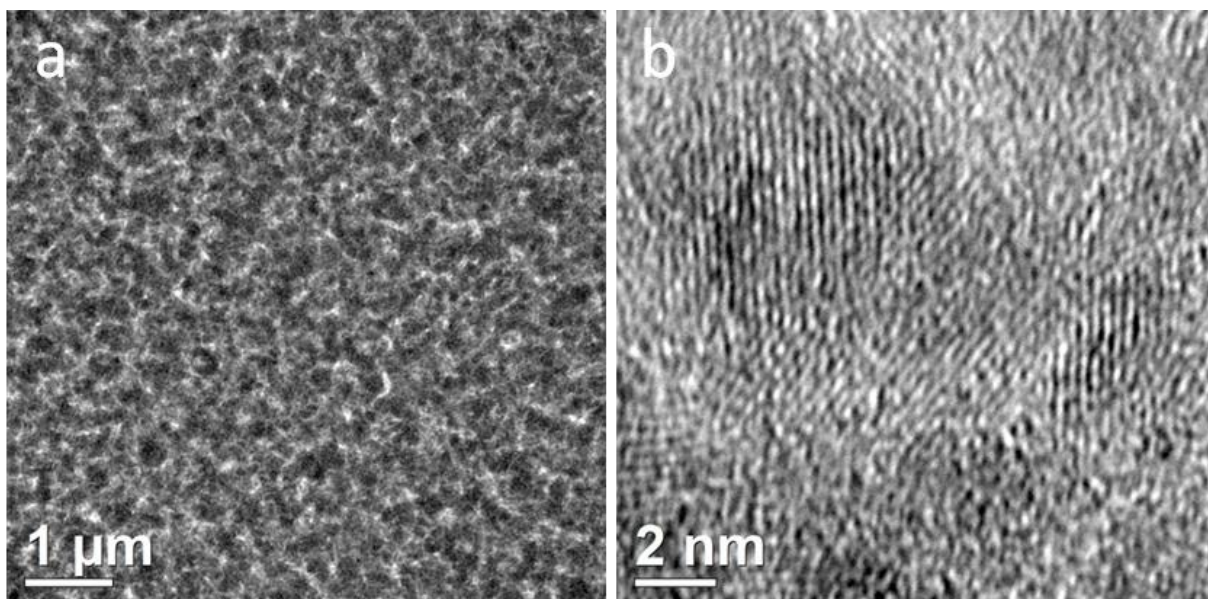


Figure 74: Top-down view TEM-BF image from a thin film CIS/PSiF-DBT specimen made on NaCl single crystals (a), HRTEM showing individual nanoparticles in the range of 3-5 nm (b).

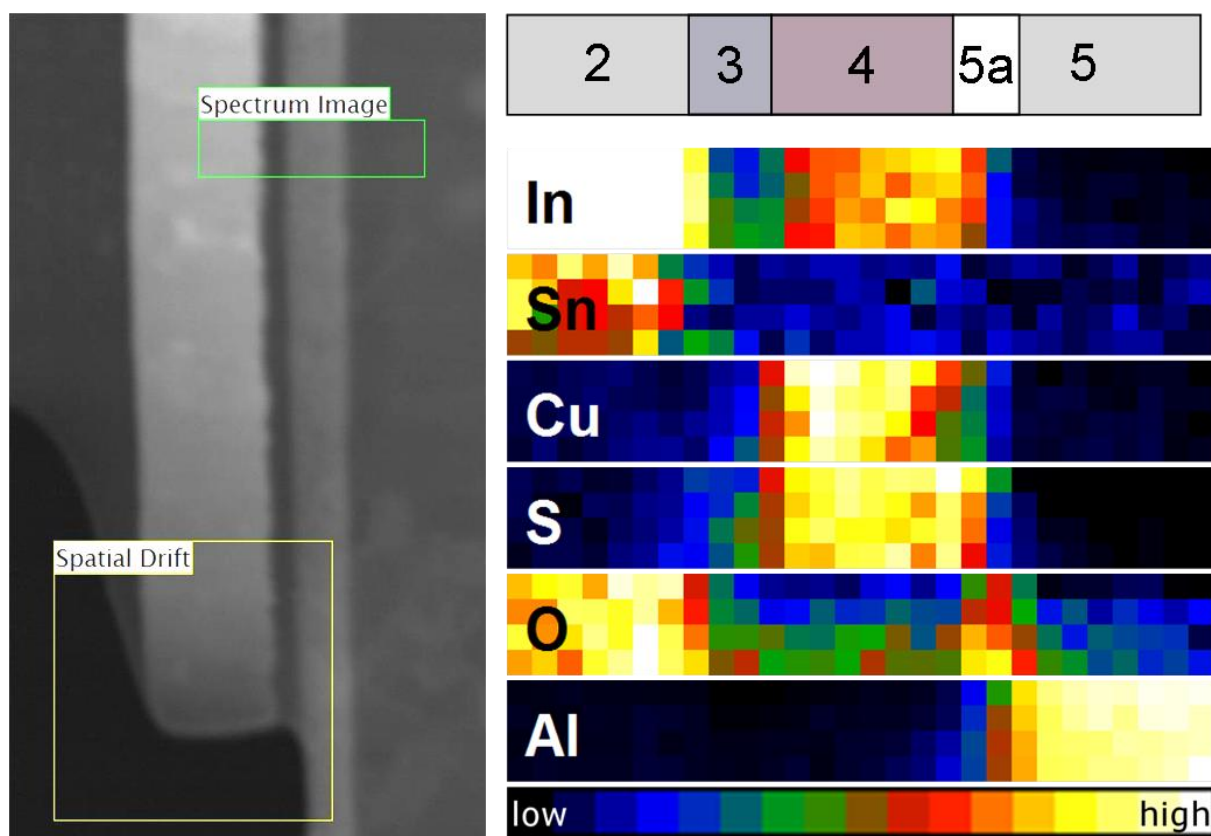


Figure 75: Spectrum image overview (STEM-HAADF) and chemical maps extracted from EDX SI data for CIS/PSiF-DBT specimen. 2: ITO; 3: PEDOT:PSS; 4: nanocomposite layer; 5a: aluminum oxide; 5: Al

The FIB lamella was investigated with TEM-EDXS spectrum imaging on the FEI Tecnai 20. Figure 75 shows an overview image (STEM-HAADF) and chemical maps extracted from the EDX SI data. An area

of 290 x 41.5 nm² was investigated using 28x4 pixels (60 seconds live time per pixel, 10.37 nm/px). The Al K, Cu K, In L, O K, Sn K and S K lines were used to extract the chemical maps. Indium (along with tin and oxygen) can be found in the ITO layer. While indium is also present in the nanoparticles inside the nanocomposite layer, the ITO layer is more compact and contains more overall indium, resulting in higher signal intensity. As expected, copper and sulfur are also found in the nanocomposite layer. At the interface between the nanocomposite layer and the aluminum electrode an aluminum oxide layer can be observed. It is unclear, if this layer has formed after exposure of the thin FIB lamella to air during transport to the microscope, or already has been there since fabrication of the device. In practice, most nanocomposite solar cells built in the project using aluminum electrodes showed to be sensitive to air (oxygen/water vapor) in long term investigations as their performance decreased. It can be assumed that the formation of an isolating oxide layer at the Al-electrode is part of the degradation process of devices.

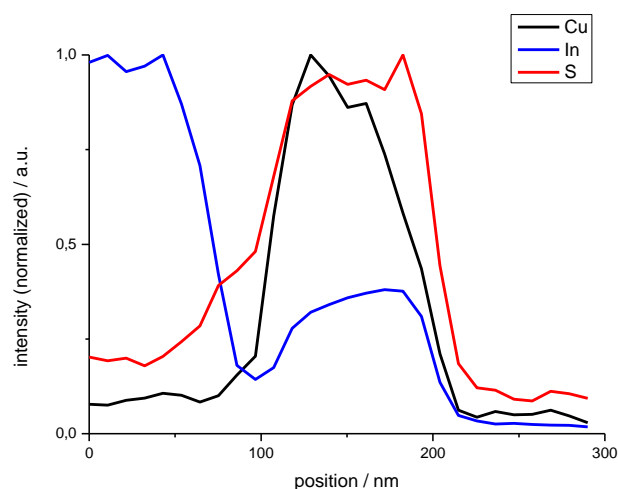


Figure 76: Normalized signal profiles for Cu, In and S signal extracted from the elemental maps in figure 75.

Profiles for Cu, In and S were extracted from the data in figure 75 by summing up the lines in horizontal direction (figure 76). As the signals were normalized, the indium signal reaches its maximum inside the ITO electrode, whereas the maxima for the copper and sulfur signal are located in the active layer. For both copper and indium a gradient throughout the active layer can be observed: Indium increases towards the aluminum electrode, while copper decreases. The reason behind the gradients and its impact on device performance is not fully understood. The indium signal in the PEDOT:PSS layer between the ITO electrode and the active layer is slightly increased, when compared to the indium signal in the aluminum layer. Leaking of indium into PEDOT:PSS has been previously observed in literature.⁹⁰

In a complementary experiment the Cu/In gradients were investigated using EELS spectrum imaging. Data was recorded using the Tecnai F 20 at spot size 3 with a pixel size of 5.2 nm. The Gatan Quantum GIF was used for recording EEL spectra with the 5 mm aperture at 460 eV, a dispersion of 0.3 eV / channel and an acquisition time of 1 second per pixel. To ensure the gradient was not a local artifact, a different area of the FIB lamella was investigated. The energy windows used for background subtraction (power law) and signal extraction are shown in table 16. Due to the overlap between the indium and oxygen edge a short window was chosen for the background subtraction of oxygen.

Table 16: Energy windows used for background subtraction and signal extraction.

Element	Background (eV)	Signal (eV)
In	416 – 442	485 – 526
O	514 – 527	529 – 565
Cu	900 – 928	945 – 1015

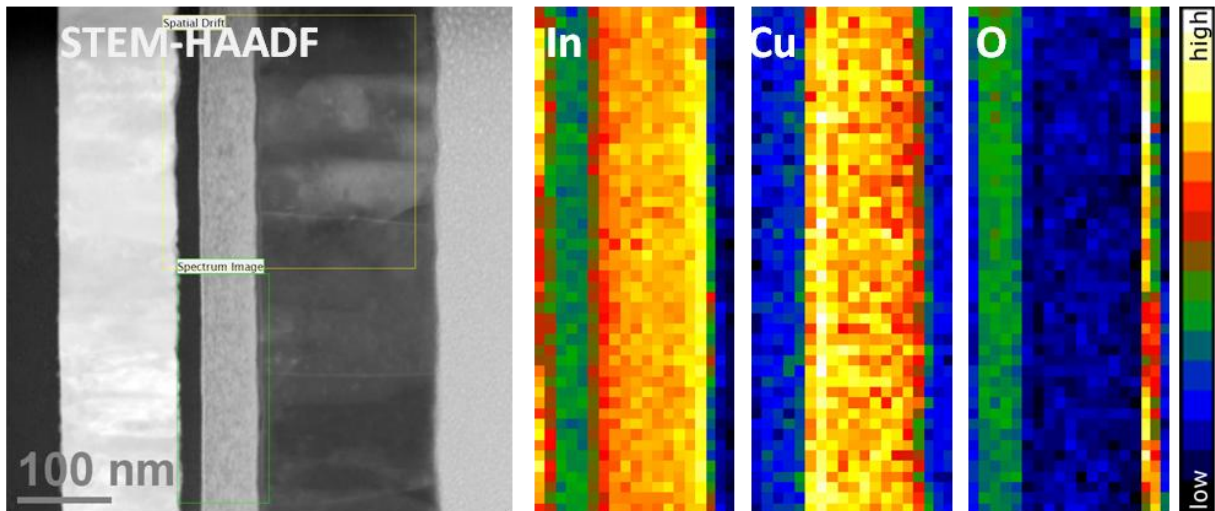


Figure 77: Spectrum image overview (STEM-HAADF) and chemical maps extracted from EELS data for CIS/PSiF-DBT specimen.

Figure 77 shows maps extracted from the spectrum image using the energy windows presented in table 16. Just like in the EDX spectrum image the gradients can clearly be seen for indium and copper, and an increase of the indium signal in the PEDOT:PSS layer. Additionally the better resolution of this image shows the sharp boundaries of the aluminum oxide layer. Profiles generated from the EELS spectrum image are shown in figure 78, confirming the previous findings once more.

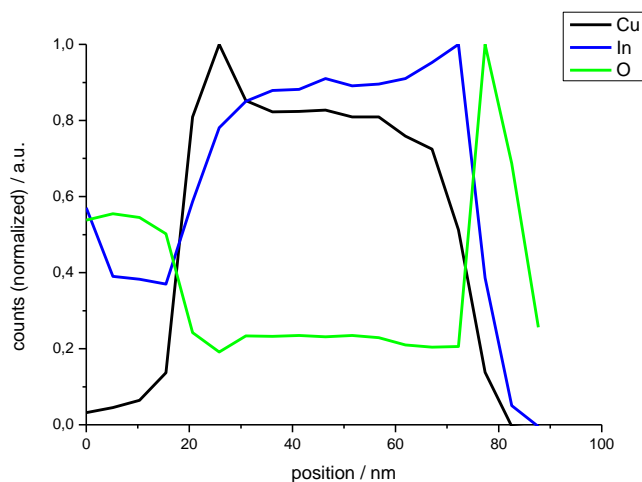


Figure 78: Normalized signal profiles for Cu, In and O signal gained from the elemental maps in Figure 77.

The I-V curve for this device is depicted in figure 79 and the parameters are shown in table 17. The combination of PSiF-DBT and the aluminum electrode yields a considerably high open circuit voltage of 540 mV. The short circuit current density is also very good, which can be attributed to efficient and dense percolation pathways to the electrode. The good fill factor indicates good mixing between nanoparticles and the polymer.

All three parameters (V_{OC} , J_{SC} and FF) are very high, resulting in a record performance of 2.8%.

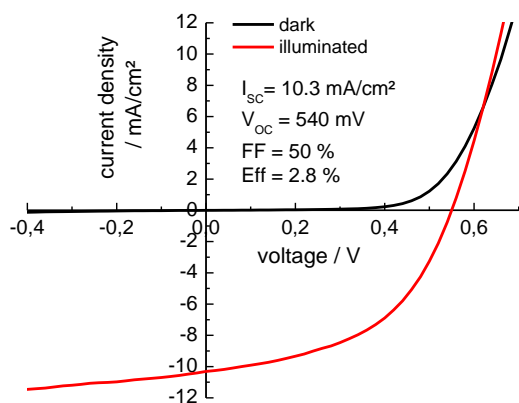


Figure 79: I-V curve of the CIS/PSiF-DBT device; measured by M. Edler.

Table 17: Parameters for CIS/PSiF-DBT device, (V_{OC} — open circuit voltage; J_{SC} — short circuit current density; FF — fill factor; PCE — power conversion efficiency).

V_{OC} / mV	J_{SC} / mA/cm ²	FF	efficiency / %
540	10.3	0.50	2.8

4.6.2 CIS/MDMO-PPV device – defect analysis

After initial I-V-characterization with good power conversion efficiency of 1.5% this device was investigated in the FIB. Surface characterization with SEM-SE showed some unusual characteristics on the whole device surface, which was not encountered in any other device.

Figure 80 shows an optical microscope image of the electrode (a) and SEM-SE images (b, c) of the surface of the aluminum electrode. A series of rifts, covering the whole surface can be seen. Since the device was working with quite acceptable parameters a decision was made to cut out a FIB lamella to investigate the nature of the rifts (see figure 84 and discussion below).

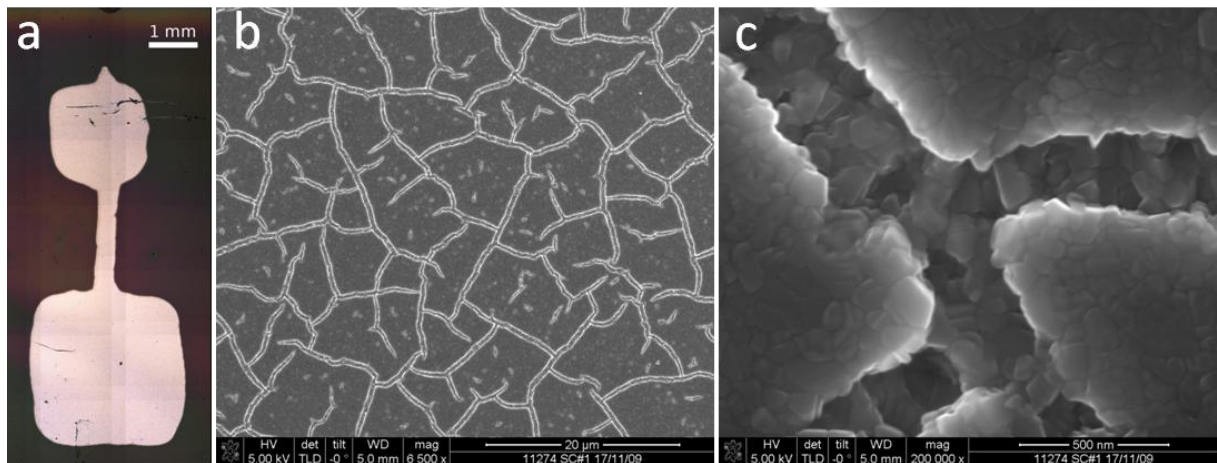


Figure 80: Optical microscope image of the electrode (a), SEM-SE images of the aluminum electrode showing rifts (b, c) on the CIS/MDMO-PPV device.

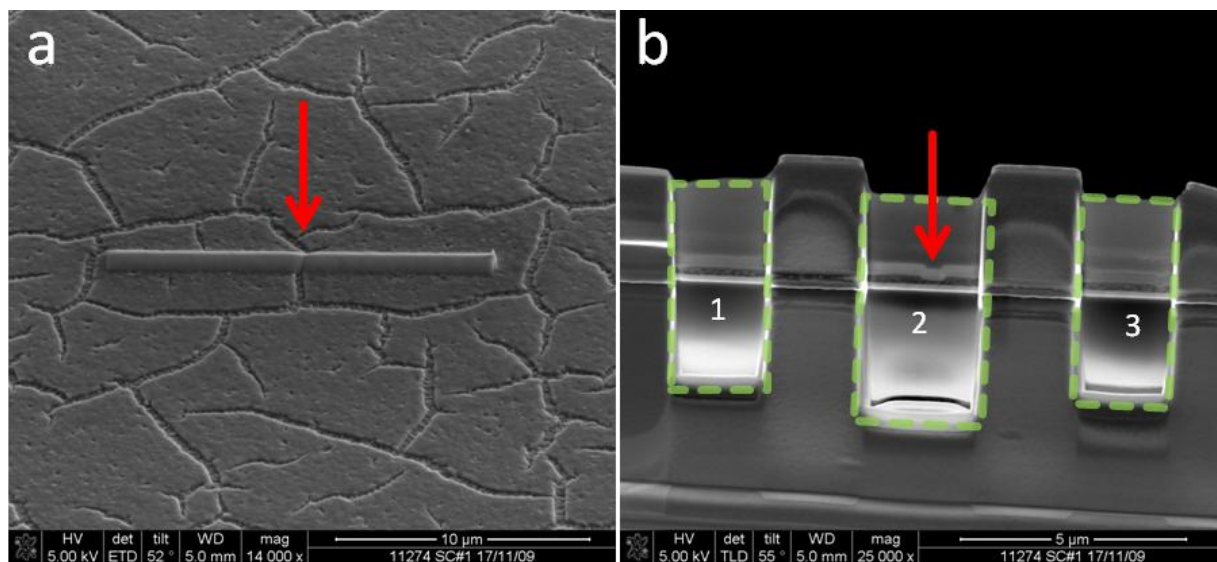


Figure 81: The protective platinum layer marks the area selected for the FIB lamella including one of the rifts in the central region of the CIS/MDMO-PPV device, top view SEM-SE image (a), cross section SEM-SE image of the lamella after thinning of three windows (b). The areas thinned to electron transparency (1-3) are marked in green, the rift is marked in both (a) and (b).

The area for cutting out a FIB lamella was chosen in a way that one of the rifts would be inside the lamella in cross section for TEM investigation. Figure 81a shows the protective platinum layer on the electrode surface including one of the rifts. After milling and transfer to a TEM grid three windows were thinned, as shown in figure 81b. The three windows are marked in green (1-3). The central window (2) contains the rift located in the middle of the platinum deposition shown in figure 81a. A layer structure including the defect can already be observed in the SEM-SE image. A more detailed investigation was carried out using TEM.

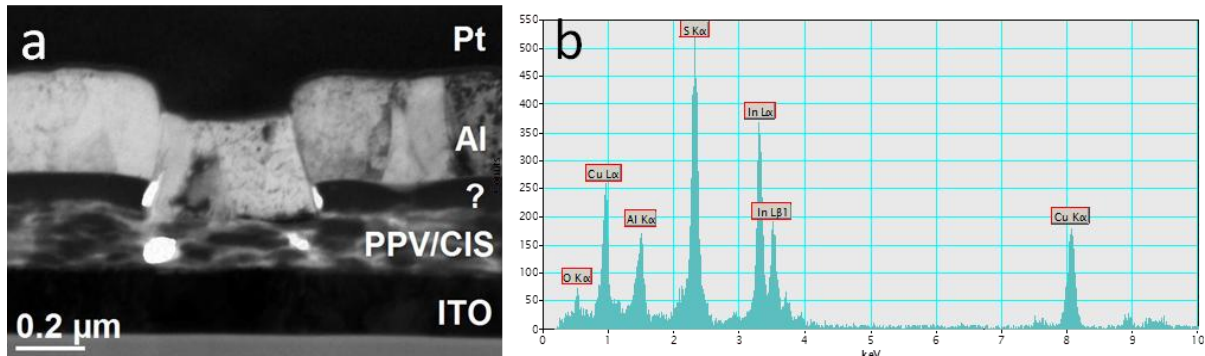


Figure 82: TEM-BF image of the lamella cut from the CIS/MDMO-PPV device showing the individual layers, including an unidentified one (a), EDX spectrum of the unidentified layer (b).

A TEM-BF image of the defect is exhibited in figure 82a. The cause of the rift can be explained by a hole in the layer between the nanocomposite layer and the aluminum electrode, which causes the aluminum to sink in. This layer is not part of the typical layout of the nanocomposite solar cell and an EDX spectrum was recorded for identification (figure 82b). Cu, In, S and Al (which can be attributed to the proximity of the Al electrode) were found in EDXS. No carbon was found, which is usually present in the nanocomposite layer because of the polymer. As the generation of X-rays for carbon is low the presence of small amounts of carbon cannot be ruled completely out, but usually at least a small peak is present when recording EDX spectra of the nanocomposite layer.

Furthermore the distribution of CIS in the nanocomposite layer is not as homogeneous as in the previously shown device using PSiF-DBT. Areas consisting mostly of CIS and areas consisting mostly of polymer can be identified. The CIS-rich areas are 30-50 nm in z-direction and 150-400 nm in xy-direction. The elongation can most likely be attributed to the shrinking process discussed in chapter 4.2.4.3.

Figure 83 shows a BF ZL image of the area and corresponding elemental maps from EFTEM investigations. The irregular CIS layer shows no carbon in the irregular CIS layer, confirming the findings of EDXS. The sulfur map corresponds to the distribution of CIS and shows an inverse image of the carbon map in the nanocomposite layer. CIS rich areas appear bright in the sulfur map and dark in the carbon map and vice versa. The aluminum electrode, covered by an oxide layer, fills the hole in the irregular CIS layer. The oxygen map shows an oxidation layer at the borders of the aluminum layer. The aluminum covering the rift is slightly separated from the rest of the layer, which caused an oxide layer to appear in between the grains.

The reason for the massive CIS layer without polymer is not fully understood. As the nanocomposite layer was coated in a two step process, it can be assumed, that during production of the second layer either polymer was not present in the solution (problems with dissolving) and/or phase separation occurred. During evaporation of the solvent most likely the rifts appeared, which were then filled up with the aluminum electrode.

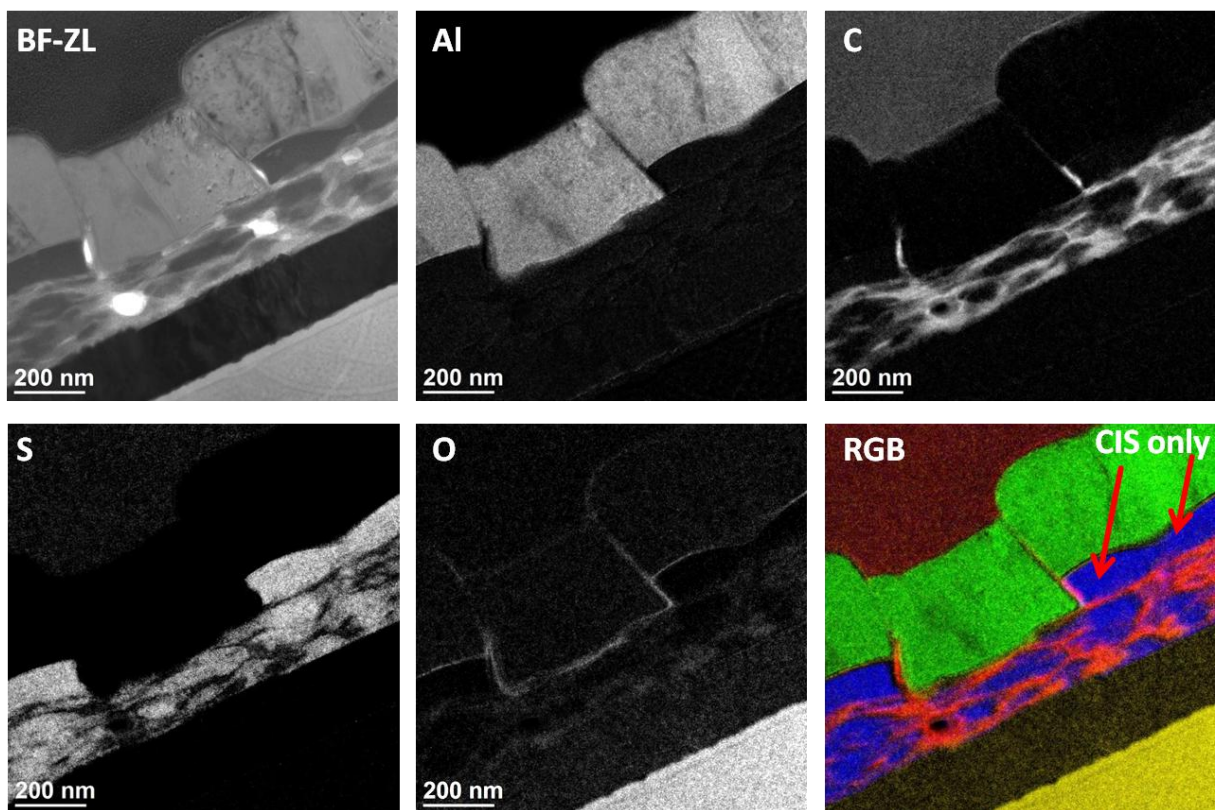


Figure 83: BF ZL and EFTEM elemental maps of the CIS/MDMO-PPV FIB lamella for Al, C, S, O and composite image (green = Al, red = C, blue = S, yellow = O)

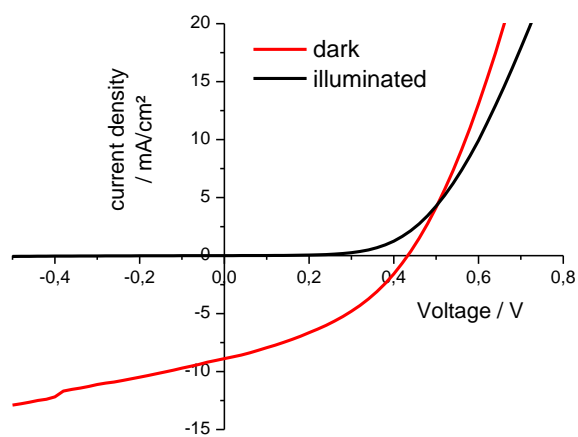


Figure 84: I-V curve of the CIS/MDMO-PPV device; measured by T. Rath.

Table 18: Parameters for CIS/MDMO-PPV device, (V_{oc} — open circuit voltage; J_{sc} — short circuit current density; FF — fill factor; PCE — power conversion efficiency).

V_{oc} / mV	J_{sc} / mA/cm ²	FF	efficiency / %
440	8.9	0.37	1.5

The performance of the device (figure 84, table 18) shows acceptable short circuit current. The open circuit voltage is around 100 mV lower than in devices using PSiF-DBT. The shape of the curve and consequently the fill factor are not optimal, resulting in an overall performance of only 1.5%. The reason for the low fill factor can be explained by the distribution of the nanoparticles in the nanocomposite layer. There is a tendency to form elongated cloud-like structures with high amounts of CIS, whereas some regions contain only little CIS. This results in a decreased contact area between the phases, hence the low fill factor. Additionally the CIS-only layer contains no polymer at all, so the only contact area is at the interface to the actual nanocomposite layer. While the rifts are immediately visible as a defect, their influence is most likely less problematic for device performance than the distribution of CIS.

4.6.3 CIS/PCDTBT device – defect analysis

During device preparation problems with the solubility of a newly acquired charge of PCDTBT were noticed. Despite these problems devices were successfully built and characterized. Investigations using optical microscopy showed indications of surface defects in all devices using the new batch of polymer. To understand the impact of the solubility problems on device performance a specimen was prepared using FIB and TEM.

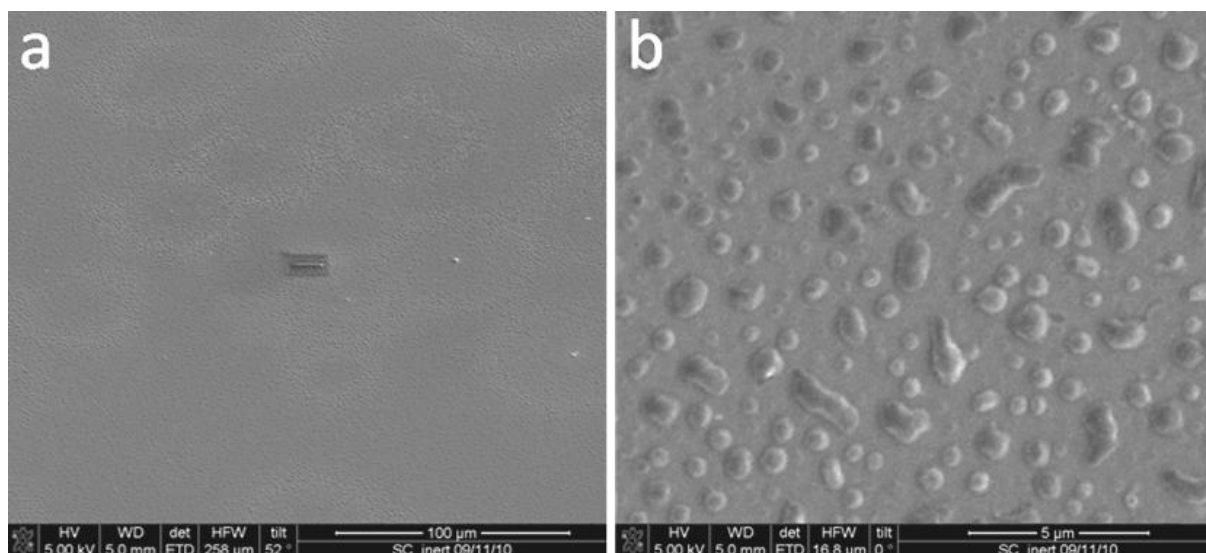


Figure 85: SEM-SE images taken during preparation of a FIB lamella from a CIS/PCDTBT device: Overview image including platinum deposition where the lamella was cut out (a), bubbles on the surface (b)

An overview image including the platinum deposition covering the area of the FIB lamella is shown figure 85a. An image taken at higher magnification (figure 85b) shows bumps on the surface of the aluminum electrode.

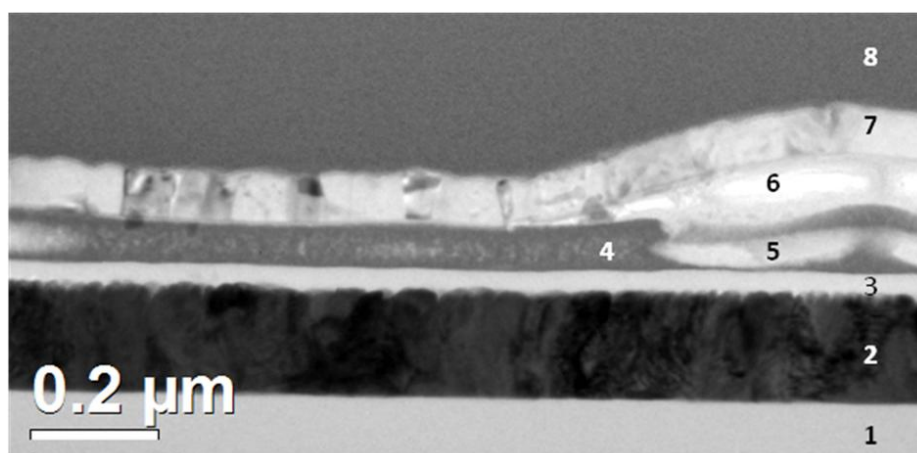


Figure 86: TEM-BF image of cross the section of a CIS/PCDTBT device. 1 glass, 2 ITO (170 nm), 3 PEDOT:PSS (35 nm), 4 CIS/PCDTBT (70 nm), 5 PCDTBT, 6 hole due to delamination, 7 Al (90 nm), 8 Pt

A TEM-BF image of the FIB-lamella is depicted in figure 86. On the left side the typical layer structure of the nanocomposite solar cell can be seen: glass (1), ITO (2), PEDOT:PSS (3), nanocomposite layer

(CIS/PCDTBT, 4), aluminum (7), platinum (protective layer, 8). On the right side of the image one of the bumps is shown in cross section. Inside the active layer a bright area, which can be interpreted to consist only of the polymer, can be seen. Above the active layer delamination of the aluminum electrode can be observed (6). Outside the defective areas CIS and polymer are very well intermixed, no cloud like phase separation as in the MDMO-PPV specimen can be observed.

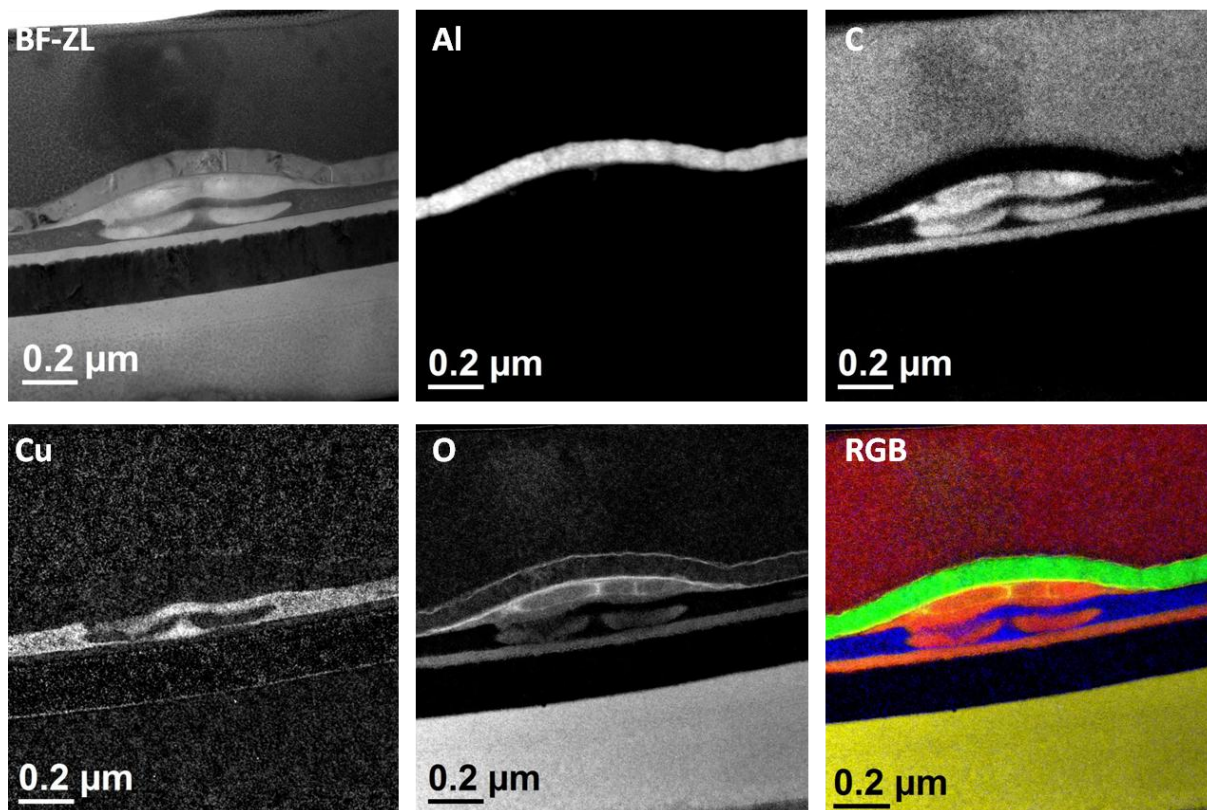


Figure 87: BF ZL and EFTEM elemental maps of FIB cut of a CIS/PCDTBT device showing Al, C, Cu, O and composite image (green = Al, red = C, blue = Cu, yellow = O)

Elemental maps from EFTEM investigations are shown in figure 87. The bright structures inside the nanocomposite layer contain carbon. When comparing the carbon to the copper map (which can in general be assumed to be representative for the distribution of CIS), it becomes evident that the carbon rich areas contain no CIS. A slightly different picture can be observed in the area above the nanocomposite layer, which is responsible for the surface bumps. Again, carbon from the polymer is observed, but no CIS. The borders of the polymer seem to be surrounded by oxygen, most likely caused by oxidation after the delamination and probably during the FIB cut. Furthermore an oxide layer can be observed on both borders of the aluminum layer.

Gel permeation chromatography (GPC) analysis of the polymer showed that two fractions with different molecular weight were present. It can most presumably be assumed that the lower mass fraction is soluble in the solvent and forms the intermixed nanocomposite layer with CIS. The higher mass fraction is also partially soluble in the precursor solution, but does not intermix with the CIS precursor. As the size of the insoluble parts is larger than the thickness of the nanocomposite layer, they stick out of the surface.

The I-V curves for this device are shown in figure 88 and the measured parameters are listed in table 19. The open circuit voltage is rather high. Due to the good mixing between CIS and polymer the fill factor and the form of the curve are excellent. However, the overall efficiency of 1.9% is rather low. This is caused by the low short circuit current density which is only 5.9 mA/cm². Only the areas consisting of both PCDTBT and CIS are active while the areas consisting only of polymer are not. The combination of CIS and PCDTBT is responsible for the good open circuit voltage and fill factor, but due to the severely reduced active area the short circuit current is decreased. Assuming an inactive area of at least one third of the area (see figure 85b) a short circuit current density of approximately 9 mA/cm² could be assumed, which would make this device comparable to the CIS/PSiF-DBT and CIS MDMO-PPV devices shown before.

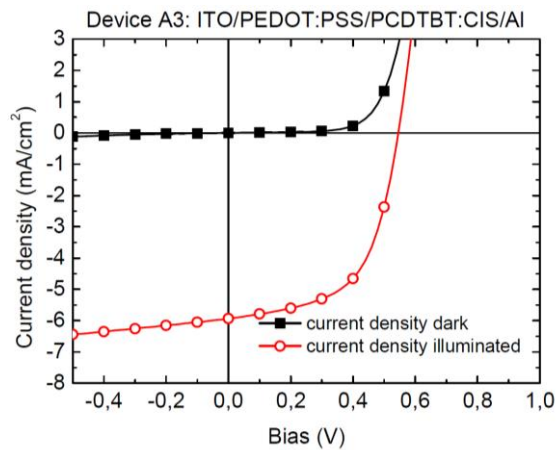


Figure 88: I-V curve of the CIS/PCDTBT device; measured by R. Trattnig.

Table 19: Parameters of the CIS/PCDTBT device, (V_{oc} — open circuit voltage; J_{sc} — short circuit current density; FF — fill factor; PCE — power conversion efficiency).

V_{oc} / mV	J_{sc} / mA/cm ²	FF	efficiency / %
540	5.9	0.58	1.9

4.6.4 Devices using PSiF-DBT and silver/aluminum electrodesⁱⁱⁱ

Devices using aluminum electrodes provide a high open circuit voltage, but their long term stability is rather low. As mentioned in chapter 4.6.1 it can be assumed that the formation of an oxide layer may be responsible for device degradation. Replacing aluminum by silver electrodes⁹¹ results in devices with much higher long term stability, but due to the work function of silver a lower open circuit voltage is gained. As a consequence the overall power conversion efficiency is reduced when compared to aluminum electrodes.

Using a combination of a thin silver layer and an aluminum electrode, an open circuit current between silver and aluminum can be expected as well as a higher stability than compared to devices using aluminum only electrodes. Devices built using this set-up were characterized by FIB-TEM and TOF-SIMS.

Figure 89a shows a STEM-HAADF image of a FIB lamella cut from a CIS/PSiF-DBT device with an Ag/Al electrode. The individual layers can be identified accordingly. The silver layer (4) is not continuous, but instead small islands of silver with a size of 5-8 nm can be observed. While there is generally a fine dispersion of the nanoparticles in the active layer, some dark areas that consist mainly of PSiF-DBT can be observed in STEM-HAADF. In most areas the thickness is below 15 nm, which should not oppose exciton separation significantly, however these areas provide no percolation pathways.

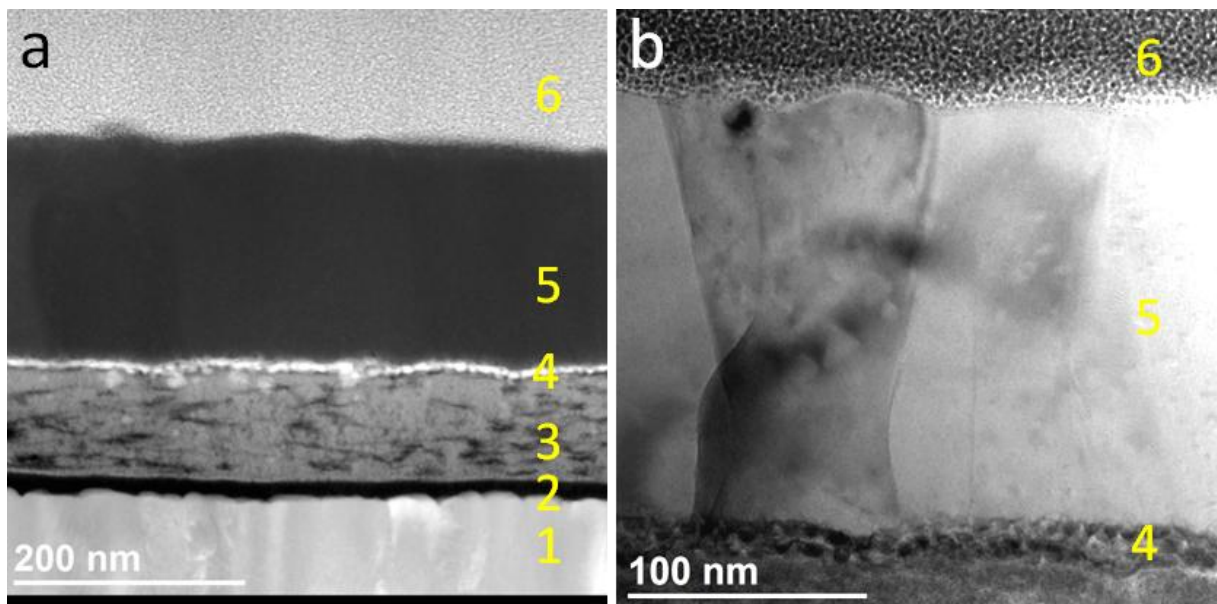


Figure 89: STEM-HAADF image of a FIB lamella for a CIS/PSiF-DBT device with Ag/Al electrode (a), TEM-BF image of the aluminum and silver layer. 1 ITO, 2 PEDOT:PSS, 3 nanocomposite layer, 4 Ag, 5 Al, 6 Pt

An area of 154 x 81 nm² was investigated using EDX spectrum imaging with 38x20 pixels (15 seconds live time per pixel, 4.05 nm / px). The Al K, Cu K, In L, O K, Sn K, Ag K, C K and S K lines were used extraction of the chemical maps (see figure 90). The silver layer can clearly be seen next to the aluminum layer; however the resolution is too low to resolve the individual silver particles visible in STEM-HAADF. No continuous oxide layer can be seen at the border of the aluminum electrode. As

ⁱⁱⁱ Parts of this chapter are already published in: Arar, M.; Pein, A.; Haas, W.; Hofer, F.; Norrman, F.; Krebs, F.C.; Rath, T.; Trimmel, G.; Comprehensive Investigation of Silver Nanoparticle/Aluminum Electrodes for Copper Indium Sulfide/Polymer Hybrid Solar Cells **2012**, 116 (36), 19191–19196

the formation of an oxide layer is considered to be responsible for performance degradation over time, absence of the oxide layer could explain increased stability of Ag/Al electrodes. However, when investigating another device from this experimental series, an oxide layer was found. The STEM-HAADF image shows some variations in the amount of CIS present in STEM-HAADF in the nanocomposite layer, which is reflected in the intensity of the sulfur signal. Dark regions consisting primarily of polymer yield lower sulfur intensities, bright regions in HAADF result in higher sulfur intensities. Copper and indium follow that distribution, however copper is enriched on the left side towards the ITO layer, whereas indium reaches its maximum towards the Ag/Al electrode. This is consistent with the gradients observed in previous investigations (see CIS/PSiF-DBT, chapter 4.6.1). The carbon signal corresponds to the information gained in HAADF in the upper half of the spectrum image. The regions low on CIS show a higher carbon signal. In the second half of the image, the carbon signal is increased. This can be attributed to contamination of the specimen during measurement.

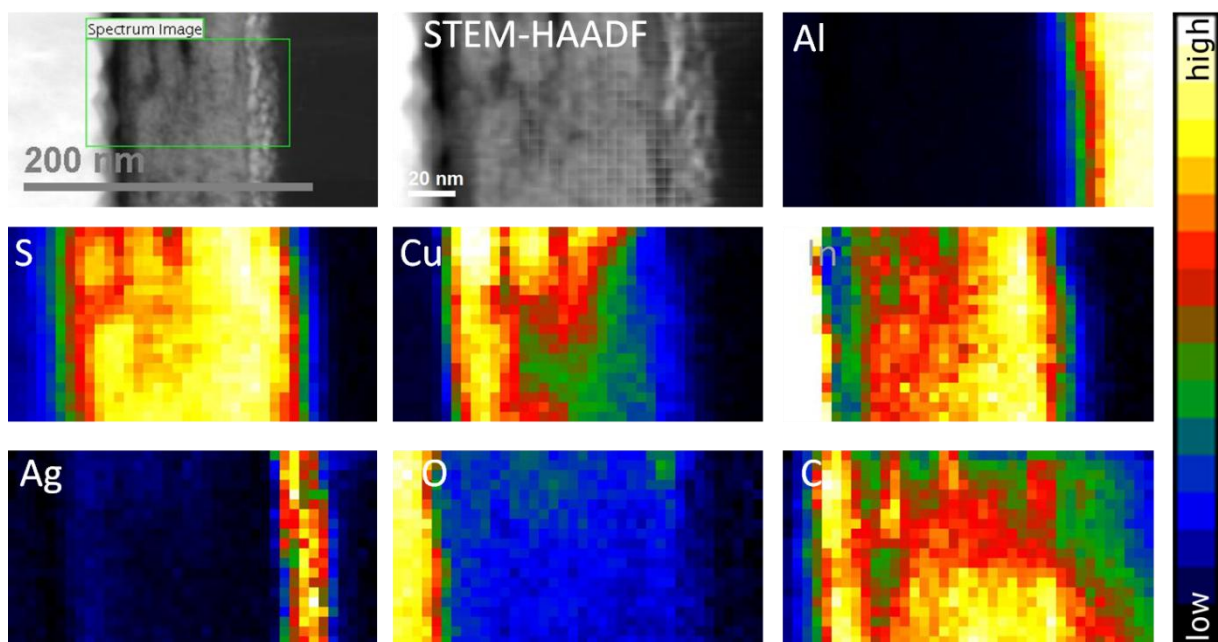


Figure 90: STEM-HAADF image of the cross section of a CIS/PSiF-DBT device with Ag/Al electrode, area selected for spectrum imaging and chemical maps extracted from EDX SI data.

One of the devices was also investigated using a TOF-SIMS IV (ION-TOF GmbH, Münster, Germany) at the Department of Energy Conversion and Storage, Technical University of Denmark, in Roskilde. 25 ns pulses of 25 keV Bi⁺ (primary ions) were bunched to form ion packets with a nominal temporal extent of <0.9 ns at a repetition rate of 10 kHz, yielding a target current of 1.0 pA. The analysis area (200 × 200 μm²) was centered in the sputter area of 300 × 300 μm². 30 nA of 3 keV Xe⁺ was used as sputter ions. Electron bombardment (20 eV) was used to minimize charge buildup at the surface. Desorbed secondary ions were accelerated to 2 keV, mass analyzed in the flight tube, and postaccelerated to 10 keV before detection.

Normalized depth profiles for positive and negative ion mode are shown in figure 91. During the sputter process some of the material is pushed into deeper layers, which causes tailing in the depth profiles. Furthermore, the thick aluminum layer causes a decrease in resolution in the active layer. Still, useful information can be extracted from the TOF-SIMS profiles.

The silver layer found in the profiles overlaps with aluminum oxide. While no oxide was found in the specimen investigated in figure 90, investigation of the device also used for TOF-SIMS also showed an oxide layer. The intensity profiles for copper, indium and sulfur correspond to the results from EDXS

spectrum imaging. There is however a mismatch between CIS (InCu) and polymer (Si) in positive ion mode. This can be interpreted as a tendency for polymer enrichment towards the Ag/Al electrode, either in the device, or during the TOF-SIMS measurement.

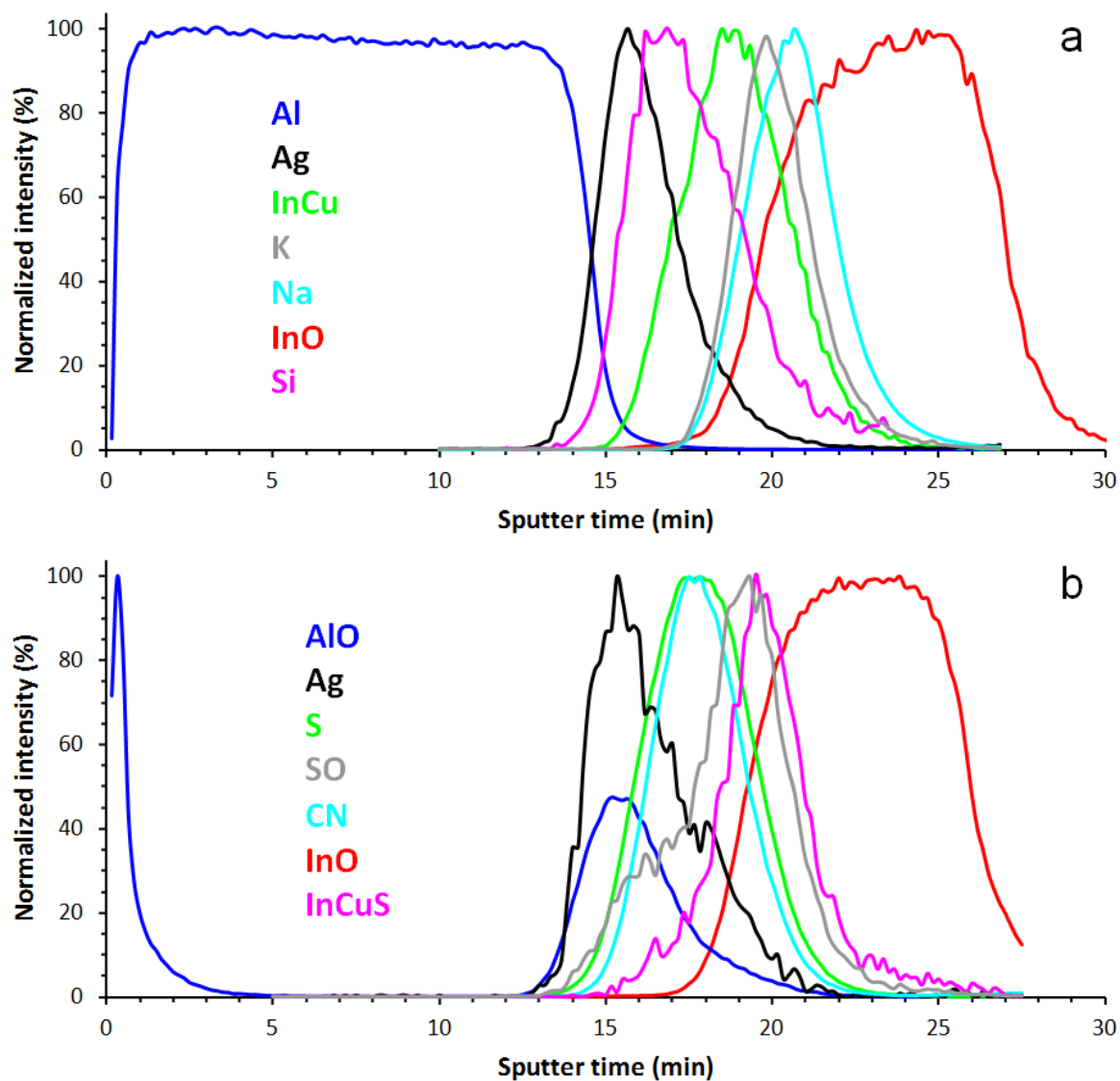


Figure 91: TOF-SIMS depth profiles. (a) Positive ion mode: InCu is a marker for CIS, Na is a marker for PEDOT:PSS, InO is a marker for ITO, and Si is a marker for PSiF-DBT. (b) Negative ion mode: AlO is a marker for aluminum oxide, S is a marker for both CIS and PSiF-DBT, and InCuS is a marker for CIS; measured by Kion Norrman, Frederik C. Krebs.

During the TEM investigation some dark grains could be noticed inside the aluminum layer in TEM-BF (e.g. figure 89b). Due to the polycrystalline nature of the aluminum layer this could be interpreted as Bragg contrast. However, STEM-HAADF investigations of the lamella show bright spots inside the aluminum layer. A stitched panorama image of the whole thinned area of the lamella in is depicted in figure 92. Several bright spots can be observed.

One of these grains was examined with EDX spectrum imaging. An area of $150 \times 100 \text{ nm}^2$ was covered using 15×10 pixels (20 seconds live time per pixel, 10 nm/px). Chemical maps were extracted using the Al K, Ag K and S K lines (see figure 93). STEM-HAADF shows a variation of brightness (and hence the atomic number Z) over the area investigated. Corresponding to the brightness in STEM-HAADF silver is present in the aluminum layer. The higher the brightness, the more silver and less aluminum is present. Both silver and aluminum electrodes are deposited in a two step thermal evaporation process. Recent investigations on organic devices show diffusion of silver into polymer layer during the thermal evaporation process.⁹² However, as the aluminum electrode is fabricated after the silver layer, it is not possible that the silver found inside the aluminum electrode is placed there during deposition. Most likely silver from the electrode is creeping into the aluminum layer over time. Therefore it can be expected that this effect cannot be observed in TOF-SIMS.

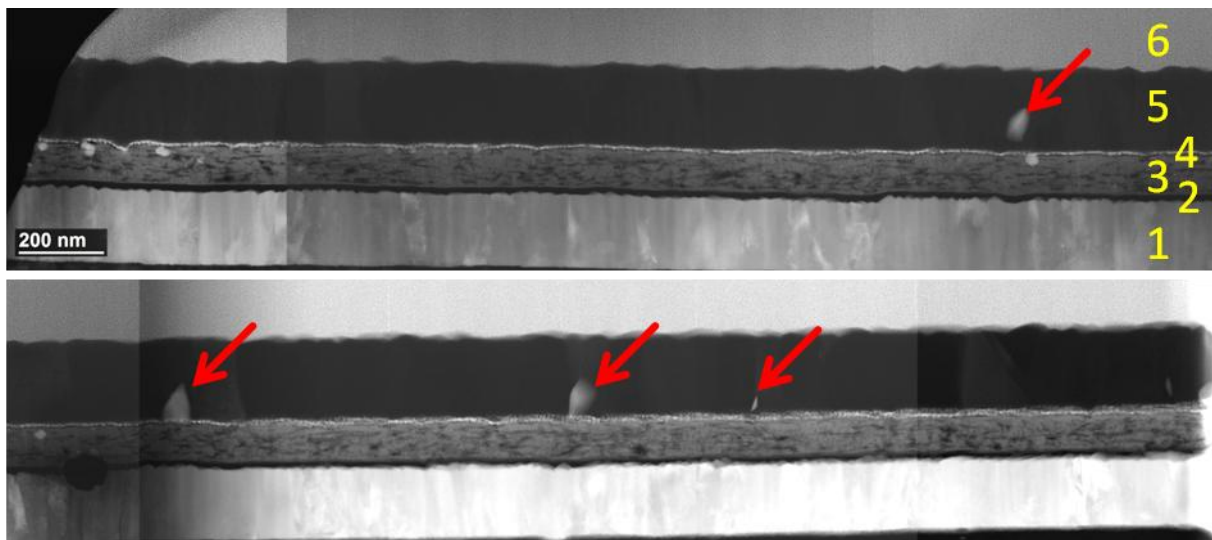


Figure 92: Stitched STEM-HAADF images covering the whole thinned area of a FIB lamella showing the diffusion of Ag into the Al layer. 1 ITO, 2 PEDOT:PSS, 3 nanocomposite layer, 4 Ag, 5 Al, 6 Pt

As the lamella was prepared using FIB it may be possible that these silver grains are an artifact caused by preparation. Due to the small thickness of the lamella some aging processes may also be accelerated by the accessibility for oxygen and water vapor. A cross section was prepared from the same device and polished with the Gatan Ilion+ (chapter 4.2.4.4). Similar bright areas could also be observed in SEM (see figure 33). Unless polishing with the Ilion+ introduced similar artifacts, which is unlikely, it can be assumed that this is an actual issue of Ag/Al electrodes. Ag is prone to melting during FIB processing; hence the artifacts observed here could be Ag on the surface of the lamella, which was molten during FIB processing. Tilting one of the FIB lamellae could help understanding this issue and should be done on the next available specimen (all current ones are in degraded condition due to aging processes).

The I-V curve for this device is presented in figure 94 and the I-V characteristics are listed in table 20. The open circuit voltage is lower than in similar devices using aluminum electrodes, but still higher than in silver-only devices. The short current density and fill factor are quite acceptable, resulting in an overall efficiency of 1.9%. As mentioned before, the areas found consisting only of polymer could slightly decrease the performance of this device. While Ag/Al electrodes are a promising approach to solve the problems of aluminum electrodes, the effects of the silver diffusion and the impact on device performance and long-term stability need to be investigated further.

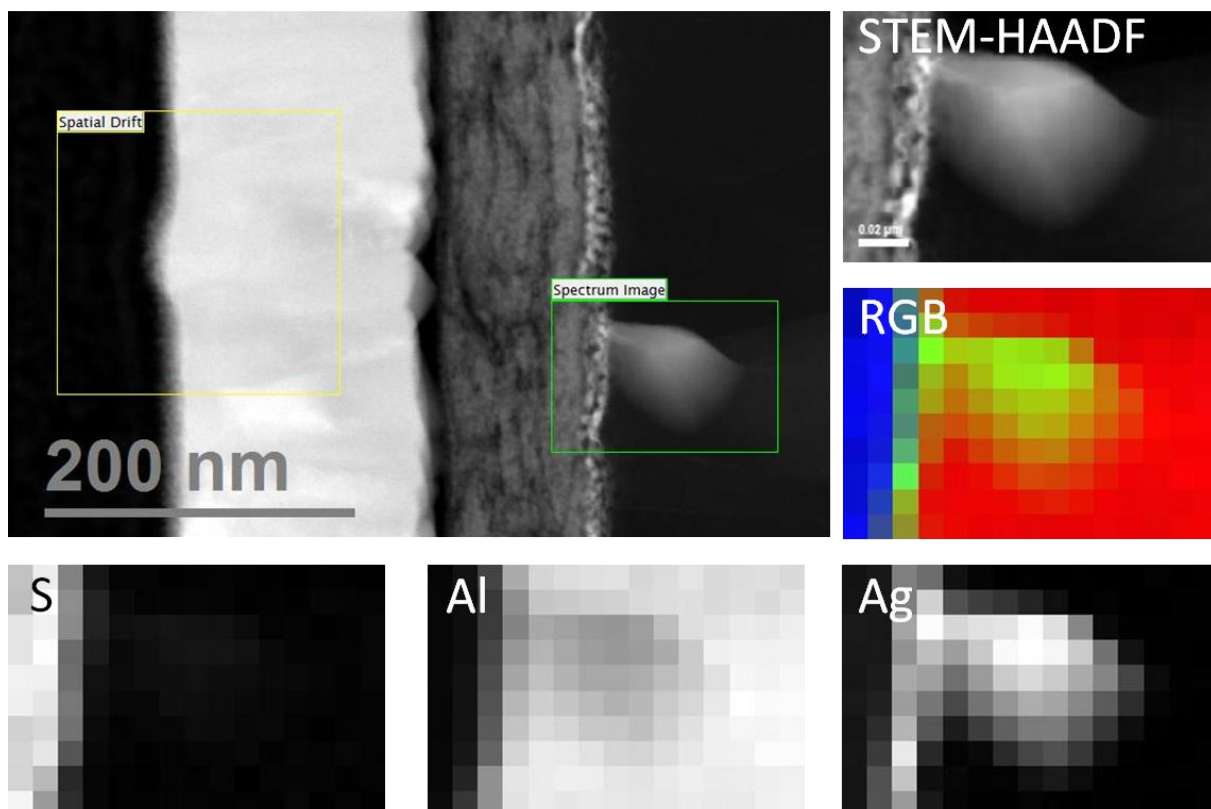


Figure 93: STEM-HAADF image of the cross section of a CIS/PSiF-DBT device with Ag/Al electrode, area selected for spectrum imaging and chemical maps extracted from EDX SI data. The RGB composite image shows red = Al, green = Ag, blue = S.

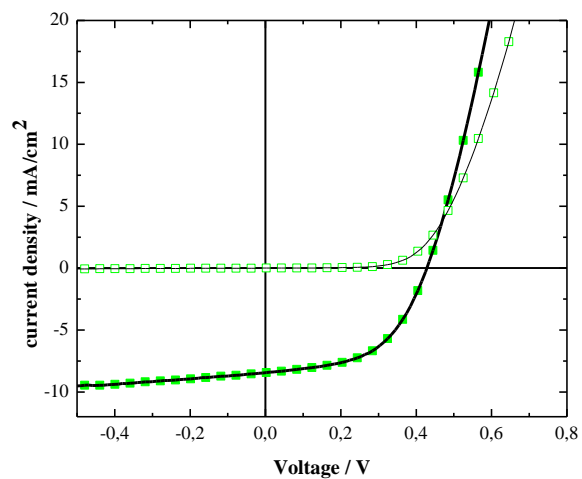


Figure 94: I-V curve for CIS/PSiF-DBT device with Ag/Al electrode; measured by M. Arar.

Table 20: Parameters of the CIS/PSiF-DBT device, (V_{oc} — open circuit voltage; J_{sc} — short circuit current density; FF — fill factor; PCE — power conversion efficiency).

V_{oc} / mV	J_{sc} / mA/cm ²	FF	efficiency / %
425	8.43	0.53	1.9

4.6.5 Conclusion of the device investigations

Using FIB it is possible to cut out specimens showing both regular as well as defective regions from a device. The investigation of cross-sections of defects can help understanding why a certain device is not functioning perfectly and why one of the parameters is unusually low, even though the other ones are good. This has been shown on the PCDTBT device, where approximately one third of the active area was simply inactive due to solubility issues with the polymer. In other cases, defects such as rifts may be clearly visible, but not mainly responsible for a decrease in device performance. The investigation of the device with the rifts showed that phase separation seems to have decreased the fill factor of the device. Finally, the understanding what makes a device successful allows tuning and addressing the relevant parameters to yield devices with high efficiency and stability.

5 Summary and Outlook

The investigation of CZTS and CZTSe nanoparticles at high magnifications and using analytical techniques requires proper specimen preparation. The type of film used on the TEM grids and the preparation technique were identified to have significant impact on the contamination behavior of specimens. Quantifoil grids showed to contaminate least compared to other TEM grids and were subsequently used throughout this work. Removal of the solvent and organic components from the nanoparticle solution is necessary to avoid specimen contamination. For this purpose the method using heat and filter paper proved successfully in getting specimens that could be measured in (S)TEM-EDX for times of over one hour. However, the irregular arrangement of the nanoparticles on these specimens was not satisfactory. Slowly evaporating the solvent at lower temperatures yields more regular arranged nanoparticles, but specimens contaminate quickly. As a consequence these specimens can only be used for imaging purposes. While these two strategies provide specimens for both scenarios, imaging and analytical work, no specimen preparation that results in regularly arranged nanoparticles without contamination issues was found. This is most likely an intrinsic problem with the type of nanoparticles and the synthesis used in this work. Despite the fact that many experiments were already made to improve the specimen preparation future work to resolve this issue would be needed.

Analytical investigations on CZTS and CZTSe nanoparticles showed that while CZTS nanoparticles can easily be prepared, CZTSe is a more complex system. Synthesis of stoichiometric CZTSe requires tuning of the precursor materials. Overview methods like SEM-EDX, XRD and Raman are not sufficient to prove the formation of stoichiometric CZTSe as the nanoparticles are chemically inhomogeneous, which was observed in both EDXS and EELS measurements of single nanoparticles. Furthermore indications of chemical inhomogeneity were also found within those nanoparticles using EDX spectrum imaging on the Tecnai F20. Analysis on the FEI Titan confirmed this assumption. For these investigations measurement conditions needed to be optimized to yield high signal intensities in EDXS while avoiding damage to the specimen caused by the electron beam at the same time. Once the beam damage is minimized the specimen drift becomes the limiting factor to the total measurement time. Times up to 600-1000 seconds were reached before significant artifacts were introduced due to cumulative errors in the drift correction engine. Compared to the measurements executed on the Tecnai F20 these results cover a larger field of view at a better resolution, but the amount of data acquired is not sufficient for quantification of the data. To improve further measurements, more data would need to be recorded. Improving the already high beam current could reintroduce the problem of beam damage; hence the measurement time should be increased. As Bruker Esprit does not offer options for its drift correction module, this could be done in Digital Micrograph. For this purpose the engine needs to mimic the behavior of the Bruker Esprit fast scanning mode, which is not implemented yet. Once the necessary changes have been made tests with Digital Micrograph's drift correction module could show, if longer acquisition times are possible.

Specimen preparation of nanocomposite solar cells was made using two different approaches. The preparation of thin films on single NaCl crystals was used for top view investigations of the active layer. Since no cutting (FIB or ultramicrotomy) is involved in the preparation, the presence of artifacts due to the processing conditions can be ruled out. Furthermore this method proved to be a high throughput method, allowing characterizing and comparing specimens from a series of samples made under varying conditions (see chapter 4.4).

The preparation of cross sections with ultramicrotomy was tested several times without success. The variation in hardness between the individual layers seems to cause delamination and breaking of the individual layers of the nanocomposite solar cell. Furthermore glass substrates cannot be cut and need to be replaced with polymers, e.g. PET. While the long term strategy is using polymer substrates for roll to roll processing, the current devices are usually built on glass substrates.

Cutting out cross sections from FIB was initially tested with reservations, as amorphization of the crystalline inorganic phase and damage to the polymer can be expected under FIB conditions. Due to carefully selected mild milling conditions the investigation of FIB lamellae showed that both the polymer and nanoparticles inside the active layer were not significantly damaged. Crystalline CIS nanoparticles were found inside the active layer and even devices with defects could be cut out without delamination of the layers. In practice the biggest downside of the FIB preparation process is the lower availability and higher instrumental effort needed as compared to the preparation of thin films. As both methods were available they could complement each other during this work by characterizing systems and production parameters using the thin film preparation method and investigation of full devices using FIB.

The *in situ* formation of CIS was observed in heating experiments inside the ESEM. The initial intention of the investigations was to mimic the heating program inside the tube furnace. In practice, this objective could not be fulfilled at full extent. The heating process had to be stopped at each temperature for a few minutes for the acquisition of images. Despite these deviations from the original heating program the transformation could be observed at approximately 120°C, which was confirmed by GIWAXS experiments with synchrotron radiation. As a side effect the electron beam induced conversion of the precursor was observed as an artifact in these investigations and became subject of its own investigation in TEM. Here the quick conversion caused by the electron beam could be observed by the emergence of the CIS peaks in SAED. The peaks were rather broad, indicating low crystallinity. In the future beam induced formation of CIS could be used for structuring CIS from the xanthate precursor to build up comb-like structures for more efficient nanocomposite solar cells.

The combination of TEM investigations with theoretical modeling and simulations can help in understanding the connection between morphological parameters of solar cells and their I-V curves. Investigations of systems using metal salts and thiourea (CIS/P3EBT) and thioacetamide (CIS/PPV) showed a strong tendency for phase separation. In these systems performance was low due to a lack of percolation pathways and areas, where excitons could not be separated due to the lack of interfaces between polymer and CIS. Systems using the xanthate precursor were able to overcome these problems and showed better intermixing between the phases. The Cu/In ratio in the inorganic phase has a significant impact on the performance of devices and is dependent on the processing parameters due to indium losses in the thermal conversion step. Variation of one of the parameters (pressure, processing temperature and precursor ratio) while keeping the two other ones fixed showed that each of them needs to be adjusted to achieve the desired ratio in the nanocomposite layer. A set of parameters was identified to yield the desired Cu/In ratio of 1/1.7.

The analysis of devices using FIB/TEM allows the identification of morphological conditions responsible for good or bad device performance as well as the investigation of defects and their impact. Several devices, both with good device performance as well as ones chose due to problems during the production process, were investigated. The investigation of a well working device using CIS/PSiF-DBT (see chapter 4.6.1) showed a gradient in the Cu/In distribution across the nanocomposite layer. To ensure the validity of the results it was measured on different areas of the FIB lamella using complementary techniques, EDX and EEL spectrum imaging. Furthermore the gradient was also found in other devices and seems to be an intrinsic property of the production process. The cause of the gradient is not yet fully understood, as well as its impact on device performance and needs further investigation. The defects as shown in chapter 4.6.2 and 4.6.3 could already be seen using optical methods or SEM. Analytical TEM investigation of a FIB cross-section was an essential part in understanding the source of these defects as well as their influence on device performance. While increasing long term stability and acceptable open circuit voltage can be expected from devices using Ag/Al electrodes (chapter 4.6.4), creeping of silver into the aluminum electrode was observed in both FIB lamellae as well as cross sections made with the Gatan Iion+.

- (1) Huenteler, J.; Schmidt, T. S.; Kanie, N. *Energy Policy* **2012**, *45*, 6–11.
- (2) Van Vliet, M. T. H.; Yearsley, J. R.; Ludwig, F.; Vögele, S.; Lettenmaier, D. P.; Kabat, P. *Nature Climate Change* **2012**.
- (3) Wissner, M. *Applied Energy* **2011**, *88*, 2509–2518.
- (4) Li, G.; Zhu, R.; Yang, Y. *Nature Photonics* **2012**, *6*, 153–161.
- (5) NREL *2010 Solar Technologies Market Report*; 2011.
- (6) Haugeneder, A.; Neges, M.; Kallinger, C.; Spirkl, W.; Lemmer, U.; Feldmann, J. *Physical Review B* **1999**, *59*, 346–351.
- (7) Ravirajan, P.; Peiró, A. M.; Nazeeruddin, M. K.; Graetzel, M.; Bradley, D. D. C.; Durrant, J. R.; Nelson, J. *The journal of physical chemistry. B* **2006**, *110*, 7635–9.
- (8) Yu, G.; Gao, J.; Hummelen, J. C.; Wudl, F.; Heeger, A. J. *Science* **1995**, *270*, 1789–1791.
- (9) Brabec, B. C. J.; Winder, C.; Sariciftci, N. S.; Hummelen, J. C.; Dhanabalan, A.; Hal, P. A. Van; Janssen, R. A. J. *Advanced Functional Materials* **2002**, 709–712.
- (10) Kumar, A.; Zhou, C. *ACS Nano* **2010**, *4*, 11–14.
- (11) Hofer, F.; Warbichler, P.; Grogger, W. *Ultramicroscopy* **1995**, *59*, 15–31.
- (12) Hofer, F. *Microsc. Microanal. Microstruct.* **1991**, *2*, 215–230.
- (13) Mitterbauer, C.; Kothleitner, G.; Grogger, W.; Zandbergen, H.; Freitag, B.; Tiemeijer, P.; Hofer, F. *Ultramicroscopy* **2003**, *96*, 469–80.
- (14) Hunt, J. a.; Williams, D. B. *Ultramicroscopy* **1991**, *38*, 47–73.
- (15) Schaffer, B.; Kothleitner, G.; Grogger, W. *Ultramicroscopy* **2006**, *106*, 1129–38.
- (16) Phillipp, F.; Höschel, R.; Osaki, M.; Möbius, G.; Rühle, M. *Ultramicroscopy* **1994**, *56*, 1.
- (17) Horiuchi, S.; Matsui, Y.; Kitami, Y.; Yokoyama, M.; Suehara, S. *Ultramicroscopy* **1991**, *39*, 231–237.
- (18) Haider, M.; Rose, H.; Uhlemann, S.; Schwan, E.; Kabius, B.; Urban, K. *Ultramicroscopy* **1998**, *75*, 53–60.
- (19) Schlossmacher, P.; Klenov, D. O.; Freitag, B.; Von Harrach, H. S. *Microscopy Today* **2010**, *18*, 14–20.
- (20) Gubbens, A.; Barfels, M.; Trevor, C.; Twesten, R.; Mooney, P.; Thomas, P.; Menon, N.; Kraus, B.; Mao, C.; McGinn, B. *Ultramicroscopy* **2010**, *110*, 962–970.
- (21) Schaffer, B.; Mitterbauer, C.; Schertel, A.; Pogantsch, A.; Rentenberger, S.; Zojer, E.; Hofer, F. *Ultramicroscopy* **2004**, *101*, 123–128.
- (22) Tran, D. T.; Jones, I. P.; Preece, J. A.; Johnston, R. L.; Brom, C. R. *Journal of Nanoparticle Research* **2011**, *13*, 4229–4237.
- (23) Nottbohm, C. T.; Beyer, A.; Sologubenko, A. S.; Ennen, I.; Hu, A.; Eck, W.; Mayer, J.; Go, A.; Ro, H. *Ultramicroscopy* **2008**, *108*, 885–892.
- (24) Joo, J.; Na, H. Bin; Yu, T.; Yu, J. H.; Kim, Y. W.; Wu, F.; Zhang, J. Z.; Hyeon, T. *Journal of the American Chemical Society* **2003**, *125*, 11100–5.
- (25) Choi, S.-H.; An, K.; Kim, E.-G.; Yu, J. H.; Kim, J. H.; Hyeon, T. *Advanced Functional Materials* **2009**, *19*, 1645–1649.
- (26) Rath, T.; Haas, W.; Pein, A.; Saf, R.; Maier, E.; Kunert, B.; Hofer, F.; Resel, R.; Trimmel, G. *Solar Energy Materials and Solar Cells* **2012**, *101*, 87–94.
- (27) Maier, E.; Fischereeder, A.; Haas, W.; Mauthner, G.; Albering, J.; Rath, T.; Hofer, F.; List, E. J. W.; Trimmel, G. *Thin Solid Films* **2011**, *519*, 4201–4206.
- (28) Maier, E.; Rath, T.; Haas, W.; Werzer, O.; Saf, R.; Hofer, F.; Meissner, D.; Volobujeva, O.; Bereznev, S.; Mellikov, E.; Amenitsch, H.; Resel, R.; Trimmel, G. *Solar Energy Materials and Solar Cells* **2011**, *95*, 1354–1361.
- (29) Santis Alvarez, A. J. Investigation of copper indium disulfide / poly (p-phenylene vinylene) nanocomposite solar cells, Master thesis, TU Graz, 2009.
- (30) Rath, T.; Edler, M.; Haas, W.; Fischereeder, A.; Moscher, S.; Schenk, A.; Trattinig, R.; Sezen, M.; Mauthner, G.; Pein, A.; Meischler, D.; Bartl, K.; Saf, R.; Bansal, N.; Haque, S. a.; Hofer, F.; List, E. J. W.; Trimmel, G. *Advanced Energy Materials* **2011**, *1*, 1046–1050.

- (31) Edler, M. Preparation and Characterization of Nanostructured Solar Energy Materials and Nanocomposite Solar Cells, PhD thesis, TU Graz, 2011, p. 91ff.
- (32) Edler, M. Preparation and Characterization of Nanostructured Solar Energy Materials and Nanocomposite Solar Cells, PhD thesis, TU Graz, 2011, p. 104f.
- (33) Reichmann, A.; Poelt, P.; Brandl, C.; Chernev, B.; Wilhelm, P. *Oxidation of Metals* **2008**, *70*, 257–266.
- (34) Pennycook, S. J.; Jesson, D. E. *Ultramicroscopy* **1991**, *37*, 14–38.
- (35) Mitchell, D. R. G. CHT Diffraction Analysis http://donation.tugraz.at/dm/source_codes/142.
- (36) Mitchell, D. R. G.; Schaffer, B. *Ultramicroscopy* **2005**, *103*, 319–32.
- (37) Mitchell, D. R. G. *Ultramicroscopy* **2008**, *108*, 367–74.
- (38) *Product Data Titan™ G2 80-200, FEI company*; 2011.
- (39) Cliff, G.; Lorimer, G. W. *Journal of Microscopy* **1975**, *103*, 203–207.
- (40) Sheridan, P. J. *Journal of electron microscopy technique* **1989**, *11*, 41–61.
- (41) Grogger, W. Quantitative Mikrobereichsanalyse im Analytischen Elektronenmikroskop unter Verwendung eines HPGe-Röntgendetektors, PhD thesis, TU Graz, 1994.
- (42) Watanabe, M.; Williams, D. B. *Journal of microscopy* **2006**, *221*, 89–109.
- (43) Gubbens, A. J.; Brink, H. a.; Kundmann, M. K.; Friedman, S. L.; Krivanek, O. L. *Micron* **1998**, *29*, 81–87.
- (44) Kothleitner, G.; Hofer, F. *Micron* **2003**, *34*, 211–218.
- (45) Freitag, B.; Mader, W. *Journal of microscopy* **1999**, *194*, 42–57.
- (46) Hofer, F.; Warbichler, P.; Grogger, W. *Ultramicroscopy* **1995**, *59*, 15–31.
- (47) Titchmarsh, J. M. *Ultramicroscopy* **1989**, *28*, 347–351.
- (48) Egerton, R. F.; Li, P.; Malac, M. *Micron (Oxford, England : 1993)* **2004**, *35*, 399–409.
- (49) Kaelin, M.; Rudmann, D.; Tiwari, A. N. *Solar Energy* **2004**, *77*, 749–756.
- (50) Katagiri, H.; Sasaguchi, N.; Hando, S.; Hoshino, S.; Ohashi, J.; Yokota, T. *Solar Energy Materials and Solar Cells* **1997**, *49*, 407–414.
- (51) Suresh Babu, G.; Kishore Kumar, Y. B.; Uday Bhaskar, P.; Raja Vanjari, S. *Solar Energy Materials and Solar Cells* **2010**, *94*, 221–226.
- (52) Salomé, P. M. P.; Fernandes, P. a.; Da Cunha, a. F. *Thin Solid Films* **2009**, *517*, 2531–2534.
- (53) Fischereeder, A.; Rath, T.; Haas, W.; Amenitsch, H.; Albering, J.; Meischler, D.; Larissegger, S.; Edler, M.; Saf, R.; Hofer, F.; Trimmel, G. *Chemistry of Materials* **2010**, *22*, 3399–3406.
- (54) Shavel, A.; Arbiol, J.; Cabot, A. *Journal of the American Chemical Society* **2010**, 4514–4515.
- (55) Wei, H.; Guo, W.; Sun, Y.; Yang, Z.; Zhang, Y. *Materials Letters* **2010**, *64*, 1424–1426.
- (56) Steinhagen, C.; Panthani, M. G.; Akhavan, V.; Goodfellow, B.; Koo, B.; Korgel, B. a *Journal of the American Chemical Society* **2009**, *131*, 12554–5.
- (57) Riha, S. C.; Parkinson, B. a; Prieto, A. L. *Journal of the American Chemical Society* **2009**, *131*, 12054–5.
- (58) Guo, Q.; Hillhouse, H. W.; Agrawal, R. *Journal of the American Chemical Society* **2009**, 11672–11673.
- (59) Dai, P.; Shen, X.; Lin, Z.; Feng, Z.; Xu, H.; Zhan, J. *Chemical communications (Cambridge, England)* **2010**, *46*, 5749–51.
- (60) Egerton, R. F. *EELS in the Electron Microscope*; 2nd ed.; Plenum: New York, 1996.
- (61) Rom, I.; Hofer, F.; Bucher, E.; Sitte, W.; Gatterer, K.; Fritzer, H. P.; Popitsch, A. *Chemistry of Materials* **2002**, *14*, 135–143.
- (62) Barth, S.; Boland, J. J.; Holmes, J. D. *Nano letters* **2011**, *11*, 1550–5.
- (63) Davidson, F. M.; Lee, D. C.; Fanfair, D. D.; Korgel, B. A. *The journal of physical chemistry. C* **2007**, 2929–2935.
- (64) Volobujeva, O.; Mellikov, E.; Raudoja, J.; Grossberg, M.; Bereznev, S.; Altosaar, M.; Traksmaa, R. *IEEE Xplore* **2008**, 257–260.
- (65) Shaheen, S. E.; Brabec, C. J.; Sariciftci, N. S.; Padinger, F.; Fromherz, T.; Hummelen, J. C. *Applied Physics Letters* **2001**, *78*, 841.

- (66) Yang, X.; Duren, J. K. J. Van; Janssen, R. A. J.; Michels, M. A. J.; Loos, J. *Society* **2004**.
- (67) Reyes-reyes, M.; Kim, K.; Dewald, J.; Avadhanula, A.; Curran, S.; Carroll, D. L. *Organic Letters* **2005**.
- (68) Yang, J.; Tang, A.; Zhou, R.; Xue, J. *Solar Energy Materials and Solar Cells* **2011**, *95*, 476–482.
- (69) Zhou, Y.; Eck, M.; Men, C.; Rauscher, F.; Niyamakom, P.; Yilmaz, S.; Dumsch, I.; Allard, S.; Scherf, U.; Krüger, M. *Solar Energy Materials and Solar Cells* **2011**, *95*, 3227–3232.
- (70) Martínez-Ferrero, E.; Albero, J.; Palomares, E. *The Journal of Physical Chemistry Letters* **2010**, *1*, 3039–3045.
- (71) Rath, T. Synthesis and Characterization of Nanocrystalline Semiconducting Materials for Nanocomposite Solar Cells, PhD thesis, TU Graz, 2008.
- (72) Omer, B. M.; Khogali, A.; Pivrikas, A. *2011 37th IEEE Photovoltaic Specialists Conference* **2011**, 000734–000743.
- (73) Lee, C.-K.; Pao, C.-W.; Chu, C.-W. *Energy & Environmental Science* **2011**, *4*, 4124.
- (74) Gruber, M.; Stickler, B. a.; Trimmel, G.; Schürerer, F.; Zojer, K. *Organic Electronics* **2010**, *11*, 1999–2011.
- (75) Gruber, M. Investigation of morphology effects on the performance of organic solar cells and hybrid cells by two-dimensional drift-diffusion simulations, Master's thesis, TU Graz, 2009.
- (76) Yang, X.; Loos, J. *Macromolecules* **2007**, *40*, 1353–1362.
- (77) Van Bavel, S.; Sourty, E.; De With, G.; Veenstra, S.; Loos, J. *Journal of Materials Chemistry* **2009**, *19*, 5388.
- (78) Oosterhout, S. D.; Wienk, M. M.; Bavel, S. S. Van; Thiedmann, R.; Koster, L. J. A.; Gilot, J.; Loos, J.; Schmidt, V.; Janssen, R. A. J. *Nature Materials* **2009**, *8*, 818–824.
- (79) Dowland, S.; Lutz, T.; Ward, A.; King, S. P.; Sudlow, A.; Hill, M. S.; Molloy, K. C.; Haque, S. a *Advanced Materials* **2011**, *23*, 2739–44.
- (80) Duren, B. J. K. J. Van; Yang, X.; Loos, J.; Bulle-lieuwma, C. W. T.; Sieval, A. B.; Hummelen, J. C.; Janssen, R. A. J. *Advanced Functional Materials* **2004**, 425–434.
- (81) Sezen, M.; Plank, H.; Nellen, P. M.; Meier, S.; Chernev, B.; Grogger, W.; Fisslthaler, E.; List, E. J. W.; Scherf, U.; Poelt, P. *Physical chemistry chemical physics : PCCP* **2009**, *11*, 5130–3.
- (82) McCaffrey, J. P.; Phaneuf, M. W.; Madsen, L. D. *Ultramicroscopy* **2001**, *87*, 97–104.
- (83) Pacher, B. P.; Lex, A.; Proschek, V.; Etschmaier, H.; Tchernychova, E.; Sezen, M.; Scherf, U.; Grogger, W.; Trimmel, G.; Slugovc, C.; Zojer, E. *Advanced Materials* **2008**, 3143–3148.
- (84) Loos, J.; Duren, J. K. J. Van; Morrissey, F. *Polymer* **2002**, *43*, 7493–7496.
- (85) Pein, A.; Baghbanzadeh, M.; Rath, T.; Haas, W.; Maier, E.; Amenitsch, H.; Hofer, F.; Kappe, C. O.; Trimmel, G. *Inorganic Chemistry* **2011**, 193–200.
- (86) Fischereder, A.; Rath, T.; Haas, W.; Amenitsch, H.; Schenk, D.; Zankel, A.; Saf, R.; Hofer, F.; Trimmel, G. *Applied Materials and Interfaces* **2012**, 382–390.
- (87) Schaber, P. M.; Colson, J.; Higgins, S.; Thielen, D.; Anspach, B.; Brauer, J. *Thermochimica Acta* **2004**, *424*, 131–142.
- (88) Werzer, O.; Matoy, K.; Strohriegl, P.; Resel, R. *Thin Solid Films* **2007**, *515*, 5601–5605.
- (89) Lewerenz, H. J. *Solar Energy Materials and Solar Cells* **2004**, *83*, 395–407.
- (90) De Jong, M. P.; Van Ijzendoorn, L. J.; De Voigt, M. J. a. *Applied Physics Letters* **2000**, *77*, 2255.
- (91) Krebs, F. C. *Solar Energy Materials and Solar Cells* **2009**, *93*, 394–412.
- (92) Fladischer, S.; Neuhold, A.; Kraker, E.; Haber, T.; Lamprecht, B.; Salzmann, I.; Resel, R.; Grogger, W. *ACS applied materials & interfaces* **2012**.